THE EFFECT OF ION IMPLANTATION ON THE STRUCTURAL AND ELECTRONIC
PROPERTIES OF MOLYBDENUM DISULFIDE

By

RYAN MURRAY

A DISSERTATION PRESENTED TO THE GRADUATE SCHOOL
OF THE UNIVERSITY OF FLORIDA IN PARTIAL FULFILLMENT
OF THE REQUIREMENTS FOR THE DEGREE OF
DOCTOR OF PHILOSOPHY

UNIVERSITY OF FLORIDA

2017

To anyone and everyone who never stopped dreaming

ACKNOWLEDGMENTS

First and foremost, I thank my parents and family for the unending support they provided during this adventure. Next I thank my advisor for providing the motivation, the guidance, and the support to navigate the challenges of such a unique project. I thank the SWAMP group, members past and present, for their assistance when it was asked and for their comradery when it was needed. I thank Intel and the Semiconductor Research Corporation (SRC) for supporting the efforts that precipitated this dissertation. I would like to give a special thanks to the engineers at the Nanoscale Research Facility, without whom I would still be trying to navigate through the darkness of the clean room. I thank Dr. Perry and Xueying Zhao for contributing so much to the work presented here. And I thank everyone at IMEC, for offering me the opportunity to see what it looks like when the world's best and brightest team up and harmonize on mutual goals.

TABLE OF CONTENTS

LIST OF FIGURES

LIST OF ABBREVIATIONS

2DM	Two-dimensional material
ALD	Atomic layer deposition
BE	Binding energy
CAFM	Conductive atomic force microscopy
CBM	Conduction band minimum
DIBL	Drain induced barrier lowering
DOS	Density of states
FWHM	Full width half maximum
I_{OFF}	Off current
I_{ON}	On current
ITRS	International Technology Roadmap for Semiconductors
LOR	Liftoff resist
MLP	Maskless photolithography
MP	Masked photolithography
MOSFET	Metal oxide semiconductor field-effect transistor
PE	Photoelectron
PIII	Plasma immersion Ion Implantation
PL	Photoluminescence
PR	Photoresist
R_C	Contact resistance
R_S	Sheet resistance
RS	Raman Spectroscopy

SCE	Short-channel effect
SIMS	Secondary ion mass spectrometry
SRIM	Stopping range of ions in matter
SS	Subthreshold Swing
STM	Scanning tunneling microscopy
STS	Scanning tunneling spectroscopy
TLM	Transfer length method
TMDC	Transition metal dichalcogenide
TOA	Take off angle
VBM	Valence band minimum
V_{Mo}	Molybdenum vacancy
V_S	Sulfur Vacancy

Abstract of Dissertation Presented to the Graduate School
of the University of Florida in Partial Fulfillment of the
Requirements for the Degree of Doctor of Philosophy

THE EFFECT OF ION IMPLANTATION ON THE STRUCTURAL AND ELECTRONIC
PROPERTIES OF MOLYBDENUM DISULFIDE

By

Ryan Murray

August 2017

Chair: Kevin Jones
Major: Materials Science and Engineering

Molybdenum disulfide (MoS_2) and other 2D materials have the potential to both

continue Moore's Law and introduce novel electronic device technologies. However,

numerous obstacles exist for bringing these unique materials from the lab to the market.

For example, the Fermi level at the MoS_2/contact interface is pinned near the

conduction band, which presents an appreciable barrier for current that results in

prohibitively large contact resistances. Additionally, MoS_2 is intrinsically n-type, but

CMOS technology requires both n- and p-type material. Thus, a reliable and tunable

method for doping MoS_2 is critical for its successful adoption.

Numerous methods for doping MoS_2 have been reported, however they typically

involve processes that are incompatible with current industrial fabrication flows.

Additionally, the methods often employ surface treatments that do not have the

thermally stability to survive the full industrial microelectronic manufacturing process.

Ion implantation is a common and well-known industrial process and is investigated

here as a doping method for MoS_2. Both grown MoS_2 films and mineralogical samples

are examined. Low implantation energies from 200-500 eV result in projected ranges of

0.9 – 2.1 nanometers, which is within the second and third surface layers. Implanted n-

type dopant species include Cl and F, p-type species include P and As, and inert species include Ar and Kr. Implantation doses ranging from 5 x 10^{12} to 1 x 10^{15} cm^{-2} are used. Surface analysis confirms implantation into the surface layers and reveals a strong correlation between surface damage and implantation dose. Activation anneals ranging from 300˚ – 800˚C in a H_2S atmosphere are employed for both dopant activation and defect repair. Devices fabricated on implanted MoS_2 are found to have a reduced on-state drive current relative to an unimplanted, unannealed control sample. Annealing is shown to repair implantation damage and improve device on-state current, however, the current never returns to that of the control sample. Microscopy with atomic resolution reveals implantation-induced defects that are not repaired by H_2S anneals, and implicates them as the source of the degraded device performance.

CHAPTER 1
INTRODUCTION

A 2D World

The 2004 isolation of graphene with Scotch tape quite literally opened a new chapter in the book of materials science, a chapter with high ceilings for potential to impact technology and the world [1]. It's difficult to imagine that, in the 21st century, a technique as simple as the mechanical exfoliation of graphite was still waiting to be discovered, and still waiting to launch entirely new areas of science and engineering. At the same time, it's inspiring to wonder what other every day, overlooked objects might have a scientific breakthrough hiding within them.

Two-dimensional materials (2DMs) began with graphene but they don't end with graphene. Numerous other 2DMs have been studied since 2004, ranging from single element materials such as black phosphorous, to compound materials such as boron nitride, to entire classes of materials such as the transition metal dichalcogenides (TMDCs) [2], [3], [4]. The excitement over these materials lies not only in their potential to continue the technological trends that silicon started so many decades ago, but also in their potential to open new technological markets that traditional semiconductors could never enter. With that, before getting too deep into how 2DMs might be used and the issues preventing their mass adoption, it's important to understand why they even have potential, which ultimately leads to the question of what they are. Therefore, a review of their properties is first in order. The whole class of 2DMs will at times be generally discussed, but the overall focus will be given to one material that has arisen as a popular representative of 2DMs: molybdenum disulfide.

Molybdenum Disulfide

Despite the relatively recent ground breaking isolation of graphene, 2DMs are not as new as 2004. In fact, the physical characteristics of MoS_2 have been studied and deduced as far back as 1923, and by one of the top scientists of that era, Linus Pauling [5]. Unlike many 2DMs, MoS_2 is produced naturally and can be mined from several locations around the world. This enabled MoS_2 to be among the first and the most studied 2DMs.

Structural Properties

MoS_2 is a member of the TMDC family. TMDCs follow the chemical formula MX_2, with M being a transition metal and X being a chalcogen. TMDCs exclude oxygen and only involve sulfur and the chalcogens below it on the periodic table. Being a 2DM, TMDCs take on a stacked structure of individual sheets. These sheets, and the crystal structure of MoS_2, are shown in Figures 1-1 and 1-2. For MoS_2, a single sheet is ~6.5 Å thick. Each MX_2 sheet is three atoms thick, with the X atom on the top and bottom of the sheet and the M atom sandwiched between. The sheets adopt a sublattice with multiple possible polytypes. For MoS_2, the relevant phase is the semiconducting 2H (trigonal prismatic) phase, though there are applications for the metallic 1T (octahedral) phase [6]. In the 2H phase (also known as molybdenite), the S-Mo-S atoms in each layer adopt an A-B-A stacking pattern, where the top and bottom S atoms sit over each other from a top down view. The 1T phase has an A-B-C stacking pattern for the S-Mo-S atoms, where the top and bottom sulfur atoms are offset such that they are independently visible from a top down view. Unlike the 1T phase, the 2H phase is thermodynamically stable and is therefore the phase found in mineralogical samples.

Hence, unless otherwise stated, future references to MoS_2 are for the semiconducting 2H phase.

Electrical and Optical Properties

MoS_2 and other TMDCs possess a unique relationship between their layer thickness and their electrical and optical properties. At the monolayer limit, MoS_2 has a direct bandgap of ~1.8 eV. As the number of layers increases, the bandgap shifts to the bulk value of ~1.3 eV and shifts from being direct to being indirect. It's this existence of a bandgap that opens the door for MoS_2 and other TMDCs for potential broad use in the semiconducting industry, and it sets them apart from graphene, which is limited in its technological applications due to its lack of a bandgap [7].

The origin of the bandgap's direct-to-indirect transition lies in the electron orbitals of the Mo and S atoms. Considering the MoS_2 energy band diagram and the Brillouin zone, the direct bandgap occurs at the K-point, while the indirect bandgap occurs between the valence band maximum (VBM) at the Γ-point and the conduction band minimum (CBM) located halfway between the K- and Γ-points (Figure 1-3). At the K-point direct bandgap, conduction band states are largely made up of Mo d orbitals, which are strong, localized, and relatively decoupled from other layers due to molybdenum's inner location within the S-Mo-S sandwich. For the indirect bandgap, conduction occurs between hybridization of Mo d and S p_z orbitals. The sulfur orbitals are "exposed," relative to the Mo orbitals, which gives them a strong interlayer coupling. As the number of layers shrinks, so too does the chance for interlayer coupling, and so too does the density of hybridized orbital states. At the monolayer, the states shrink beyond the Mo d states at the K-point and the K-point states become the bandgap [8].

In addition to influencing the magnitude of the bandgap, the shifting band structure will also have an effect on the density of states (DOS) at the bandgap, which could influence the MoS_2 thickness that is targeted for fabrication of electronic devices device [9], [10], [10].

The shifting band structure will also have implications on the MoS_2 optical properties. With all else equal, a direct bandgap has a significantly higher chance for emission or absorption of a photon when compared to an indirect bandgap. When plotting the energy band diagrams in energy-momentum space (E-k axes), a direct bandgap is defined as when the conduction band minimum and valence band maximum occur at the same k point; for an indirect bandgap, the CBM and VBM occur at different k points. In a direct bandgap, for an electron to transition from VBM to CBM all that is required is excitation through the absorption of sufficient energy, for example from an incident photon. However, for the same transition to occur in an indirect bandgap the electron must absorb sufficient energy (from a photon) and have a near-simultaneous, sufficient change in momentum (from an interaction with a phonon). The likelihood of the electron-photon-phonon interaction is significantly less probable than the electron-photon interaction alone, hence monolayer MoS_2, with a direct bandgap, would be expected to be more optically "active" than bulk MoS_2, which has an indirect gap [11].

Technological Potential of MoS_2

Moore's Law

The microelectronics industry has moved at a truly astonishing pace, largely because of advancements in both the understanding of and the processing of silicon. When Moore realized and verbalized the potential for that pace it became a kind of self-fulfilling prophecy, or carrot at the end of a stick, toward which the industry ceaselessly

paced [12]. Moore's observation, that our command of semiconductor technology will advance at a rate such that the number of transistors in a dense integrated circuit will double approximately every two years, is no easy task. Many people over the years have predicted the end of this growth, but the industry has banded together, even potential rivals, to develop goals and landmarks to achieve that pace for the benefit of the entire industry [13]. This gives the industry an idea of which problems need to be addressed and by when they need to be address. It gives the industry a roadmap of it will face. One such roadmap is the International Technology Roadmap for Semiconductors (ITRS) [14], which provides a useful metric against which not only the industry, but researchers in academia, can judge their results. Put simply, the summarized message of these roadmaps is "smaller," make everything smaller or thinner.

Silicon has rightfully dominated these roadmaps since they first started. The grueling pace has been maintained through a combination of many things: evolutions in transistor designs, such as ultra-thin body (UTB) devices or multi-gate FETs; advancements in important transistor materials other than Si, such as high-k dielectrics; and with the manipulation of Si, such as with strain. It is possible this pace will continue for some time with Si at the forefront, perhaps through the introduction of even more advanced transistor designs, such nanowire channel devices. However, it's also possible that Si technology will simply be unable to keep up due to its inherent material properties. This has caused a flurry of research into potential material replacements for Si. Compound semiconductors have long been predicted to be that replacement, most notably the III-V materials such as InGaAs. More recently, 2DMs have emerged as

potential replacements for Si. While 2DMs do have several major challenges, such as effective growth methods, they also have inherent material properties that could allow them to take the wheel and drive the industry to places on the roadmap that Si could never reach.

Short-channel Effects

To understand the potential benefits of 2DMs, specifically MoS_2, it's important to first understand the challenges that arise when devices are aggressively scaled. These challenges are broadly termed the short-channel effects (SCE).

One important SCE is leakage current: as the channel is made shorter the drain and source regions sit nearer each other; eventually they sit so close that carriers can tunnel through the energy barrier that exists between them even when the gate has turned the device off. This unwanted flow of current contributes to what is called the off-current, I_{OFF}. The tunneling effect has been shown to have an inverse relationship with the carrier's effective mass in the direction of current flow [15]

In contrast to I_{OFF}, there exists a metric called on-current, I_{ON}, which is the current flowing through the device when the gate bias exceeds the threshold voltage of the channel. Preferably, a device would have both a low I_{OFF}, which minimizes unnecessary heat generation and reduces unnecessary power consumption, and a high I_{ON}, which reduces the number of transistors needed to drive a given current. Both metrics can affect scaling: the reduced generation of heat could allow more transistors to be packed into a tighter area without exceeding thermal limitations, and if fewer devices are needed to drive a desired current, then the same number of transistors can perform more operations. In fact, when intel moved to the 14-nm node, the increase in I_{ON} per individual transistor was large enough that two transistors could match the output

22

current of three transistors from the previous node. Thus, both I_{ON} and I_{OFF} are important metrics, and they are often combined into a single metric, the I_{ON} /I_{OFF} ratio.

In addition to the magnitudes of I_{ON} and I_{OFF}, it's also important how quickly a device can switch from one state to the other. This is typically measured with a term called the subthreshold swing (SS), measured in mV/decade, and it's the reciprocal of the slope of the I_{DS} curve with respect to applied gate voltage, in the subthreshold regime ($V_G < V_T$). A lower SS is better as it means a sharper turn on; the theoretical lower limit at room temperature is 60 mV/dec for a typical MOSFET design, based on the exponential decay of carrier density (in the energy band) with increasing energy [16].

Another important factor for reducing leakage current in devices is the channel thickness. For thick channels, leakage current can flow in the depths below which the gate can reach. This motivated a drive toward thinner channels, or ultra-think body (UTB) devices. There is a limit, however, on the effectiveness of continually thinning a typical, bulk semiconductor: quantum confinement will arise that increases the band gap; dangling surface bonds can induce carrier scattering, which lowers their mobility; and thickness non-uniformity can influence both factors.

Leakage currents will also be influenced by the bandgap of the channel material. A semiconductor with a larger bandgap will inherently have a larger barrier for unwanted carrier tunneling or excitation [17]. If the bandgap is too small, it can be overcome by the drain voltage and allow for undesirable leakage current.

An additional important factor for short-channel devices is drain-induced barrier lowering (DIBL), which occurs when the depletion region from the drain sufficiently interferes with the inversion layer under the gate. At short channels, this will effectively

reduce the channel length, which will reduce the channel resistance and in turn increase the channel current. By competing with the gate for electrostatic control over the channel, DIBL can make the gate need to work harder to achieve the same carrier accumulation, observed as a degradation in SS. In extreme cases, the gate will be unable to turn off the channel. DIBL can be related to a term call the characteristic length, or lambda. Lambda is essentially a measure of how affected a device is by a change in the channel length. The saturation drain-source current, I_{DS}, in a MOSFET is independent of the drain source voltage, V_{DS}, and can be can described as in Equation 1-1, where μ is the carrier mobility, C_{ox} is the capacitance of the oxide, W is the device width, L is the device channel length, V_G is the applied gate bias, and V_T is the threshold voltage of the device:

$$I_{DS} = \frac{1}{2}\mu C_{ox}\frac{W}{L}(V_G - V_T)^2 \qquad (1\text{-}1)$$

DIBL has the effect of reducing the device's channel length, which substitutes a L+ΔL term for the L term in Equation 1-1, which, when simplified, yields Equation 1-2:

$$I_{DS} = \frac{1}{2}\mu C_{ox}\frac{W}{L}(V_G - V_T)^2\left(1 + \frac{\Delta L}{L}\right) \qquad (1\text{-}2)$$

Substituting the additional length term with a term that includes the drain source voltage, yields Equation 1-3:

$$I_{DS} = \frac{1}{2}\mu C_{ox}\frac{W}{L}(V_G - V_T)^2(1 + \lambda V_{DS}) \qquad (1\text{-}3)$$

The substitution from Equation 1-2 to Equation 1-3 allows for relating I_{DS} and DIBL to the source of the DIBL, the drain-source voltage. Lambda is then the coefficient connecting those relationships between I_{DS}, DIBL, and V_{DS}. Lambda is a measure of how a device responds to a change in the channel length; low lambda means the device

is less affected by changes in channel length, and less susceptible to DIBL. A large

lambda means devices are more sensitive to changes in the channel length and to DIBL

[18]

From a materials aspect, a metric has been defined to describes a material's

ability to withstand short-channel effects, also called lambda. It is also directly related to

the dielectric constant of the channel material, as shown in Equation 1-4, where ε_s is the

dielectric constant of the semiconductor, ε_{ox} is the dielectric constant of the gate

dielectric, t_s is the thickness of the semiconductor, and t_{ox} is the thickness of the gate

oxide. It behaves like the previously mentioned lambda, where a low lambda (low

dielectric constant) means the material is less susceptible to SCEs like DIBL.

$$\lambda = \sqrt{\frac{\varepsilon_s}{\varepsilon_{ox}} t_s t_{ox}}$$

(1-4)

Short-channel Advantages of MoS$_2$

Reports in literature have considered the concerns mentioned above and have

identified the properties that a material must possess in order to have superior immunity

to SCEs: a high effective mass, a large bandgap, a low in-plane dielectric constants,

and uniform atomic thickness [19]. MoS$_2$ has all those properties, though some of the

them, such as the bandgap, will change with MoS$_2$ thickness.

Monolayer MoS$_2$ has a bandgap of ~1.8 eV, which is larger than both bulk and

thin body silicon's (~1.1-1.4 eV) and will help reduce tunneling leakage currents [17].

MoS$_2$ is atomically thin and flat in its discrete sheets, so it should not be subject to many

of the surface scattering effects that occur with other traditional semiconductors at those

thicknesses. MoS$_2$ also has a low in-plane dielectric constant (~3.3 - 4), much lower

than many of the common semiconductors such as Si (~11.7), Ge (~16.2), and GaAs (~12.9), which will make MoS_2 less susceptible to DIBL and enhance the gate's electrostatic control over the channel. MoS_2 also has a larger effective mass (~0.55 m_0) than Si (~0.19 m_0), providing another advantage for reducing tunneling current [20], [21].

Indeed, MoS_2 has been predicted to be superior to Si at channel lengths below 5 nm, in the form of improved SS, improved I_{ON}, and likewise improved I_{ON}/I_{OFF} [22]. When compared to another candidate for replacing Si, the III-V semiconductor $In_{0.7}Ga_{0.3}As$, MoS_2 also fared well, with a much better I_{ON}/I_{OFF} (1.4 x 10^7 vs x 312), but with a lower mobility and drive current [23]. For those reasons, it was suggested that MoS_2 be considered for low-operating-power (LOP) applications, where leakage current is the priority.

Devices fabricated on monolayer MoS_2 devices have been shown to have excellent properties [24]. The device's gate length was relatively long, at 1.5 μm, but the results yielded a remarkable I_{ON}/I_{OFF} of 10^8 and an ultralow off-current of less than 100 fA. The device employed a back-gate design, as is typical for MoS_2 devices, which yielded a low field-effect mobility of 0.5-3 cm^2/Vs. However, after the deposition of a top-gate dielectric and contact, the mobility increased to over 200 cm^2/Vs.

Additionally, there are reports of short channel MoS_2 devices that employ unique designs and fabrication processes. One such technique involved placing a nanowire over an exfoliated MoS_2 flake, followed by placing a sheet of graphene over the entire device, then depositing the contact metal, and finally physically lifting off the nanowire to expose the channel and separate the source and drain contacts [25]. The resulting

channel length was 80 nm. The graphene interlayer allowed for a separation between the MoS_2 and contact metal that prevented Fermi level pinning, which resulted in a contact resistance of 0.54 kΩ-μm, a nearly 10x reduction compared to devices without the graphene layer. The low contact resistance and short channel produced a record-high MoS_2 room temperature on-current of 0.83 mA/μm. The results compare favorably to 2017 ITRS requirements for silicon.

Novel Devices

MoS_2 has the potential to impact technology regardless of any short channel benefits it may possess. The unique physical properties allow for applications where Si fails. These unique properties are generally shared among all 2DMs. For example, MoS_2 is flexible, and reports have shown no degradation of the device properties even after bending to a radius of 0.75 mm [26]. Additionally, monolayer TMDCs have a direct bandgap whose magnitude varies depending on the material. Different monolayer TMDCs can be stacked to create an atomically sharp, optically active p-n junction for optoelectronic purposes [27]. The properties of such a device are highly tunable, given the broad range of properties available across the spectrum of 2DMs. The tunable p-n junction provides an additional technological opportunity with tunnel FETs (TFETS). Conduction in TFETs occurs via band-to-band tunneling, from the valance band of the source into the conduction band of the channel. This transport is fundamentally differently than in traditional MOSFETs, where conduction occurs within the same band. The physics underlying this difference gives TFETs beneficial properties, such as SS values below the theoretical limit and lower off-currents than are capable with traditional MOSFETS. Thus, TFETs have a potential important place in future microelectronics, and TMDCs have favorable energy band alignments for that potential [28].

Issues Facing MoS$_2$

Contact Resistance

Chief among the issues facing most 2DMs is the large contact resistance observed for devices. A large R_C is especially detrimental for short-channel devices; as channel lengths continue to decrease, the channel resistance contributes less and less to overall resistance, and contact resistance dominates the overall device resistance. For MoS$_2$, the point at which channel resistance is negligible and R_C dominates was found to be at channel lengths of less than 200 nm [29]. Thus, for continued scaling of devices, R_C reduction is an important goal.

.Depending on the contact metal used, R_C for MoS$_2$ can vary from 4.7 kΩ-μm for Ni and Au, to [29], to 0.8 kΩ-μm for Ti [30], [9]. However, those values are recorded with an applied backgate bias, which will lower the R_C through electrostatic doping of the contact region, although it may help account for the lack of chemical doping at the contact region. Current ITRS requirements for total resistance from source to the drain, R_{SD}, are 134-245 Ω-μm, depending on the device geometry and purpose [31]. By 2026, R_{SD} must drop to 100 Ω-μm.

The large R_C in MoS$_2$ is attributed to a Schottky barrier that forms due to Fermi level pinning (FLP) at the metal/MoS$_2$ interface [29], [32]. FLP is a phenomenon that decouples the Schottky barrier height (SBH) from the parameters that would be expected to contribute to its magnitude; mainly, it makes the barrier independent of the work function of the contact metal. At the simplest level, the SBH (Φ_B) is expect to be equal to the difference between the work unction (WF) of the contact metal and the electron affinity of the semiconductor (the difference between the vacuum level and the conduction band minimum), as shown in Equation 1-5:

$$\Phi_B = WF - \chi \tag{1-5}$$

The SBH is then expected to have a linear relationship with the WF of the metal contact, and plotting the SBH as a function of contact metal WF should yield a line with a slope of 1. The SBH that results from Equation 1-5 is a useful predicative tool; it implies that choosing a low-WF metal for a contact will result in a low barrier for electrons to flow, while a high-WF metal contact should provide a low SBH for holes to flow. However, with FLP, the barrier height is "pinned" to a location in the semiconductor's energy spectrum. The SBH will then not equate to that predicted by Equation 1-5, but will be centered around some value and the plot of SBH vs. WF will yield a line with a slope of less than 1. The strength of the pinning effect will vary from material to material: from moderate, to severe, where the plot of SBH vs. WF yields a nearly flat line of slope approaching zero. The location can be near an energy band, as is the case with InAs, or near mid-gap, which can result in a large R_C.

The origin of FLP is debated and it can emerge from a variety of different effects. Different materials will be subject to varying levels of influence from the different effects, the pinning can be caused by two different things in two different materials. FLP is ultimately due to the creating of interfacial states. One cause of FLP could be metal-induced gap states (MIGS), which emerge due to the electron wavefunction of the metal extending and decaying into the interfacial depths of the semiconductor. Another source of energy states could be due to defects or disorder, called defect-induced gap states (DIGS). MoS_2 does have a concentration of defects, however MIGS and DIGS are not expected to be the dominant cause of FLP in MoS_2, since the models that try to predict FLP assume pristine MoS_2, and yet they still yield FLP.

For MoS$_2$, FLP is thought to be due to two reasons. First, the metal/MoS$_2$ interface results in charge redistribution that induces an interfacial dipole moment; this effectively reduces the WF of the metal. Second, the electron distribution of the interfacial S atoms is disrupted by presence of the metal; this disruption then affects the S-Mo bond and the Mo d orbitals. The Mo 4d orbitals are the main contributors to the DOS in the conduction band; their disruption then introduces gap states into the upper half of the band gap, as is observed experimentally.

Models have predicted FLP with MoS$_2$, with the SBH vs. contact WF plot yielding a slope of 0.71, which does not indicate strong pinning. However, experimental results yielded a slope of 0.1, which does indicate strong pinning [33]. Thus, the assumptions for the models FLP origins in MoS$_2$ are not complete.

One common method for eliminating FLP is to introduce a thin oxide layer between the metal and semiconductor. The oxide must be thin enough to allow easy carrier tunneling, but thick enough to prevent the prevent whichever FLP-inducing reaction that occurs at the metal-semiconductor interface. Reports did observe a reduction in the barrier height by adding a thin (1-2 nm) oxide layer, with a reduction from 0.18 eV to 0.09 eV for TiO$_2$ interlayer and 0.13 for Al$_2$O$_3$ interlayer [34]. The reduction in SBH resulted in a substantial decrease in the series resistance of a device, from 125 kΩ to 3.5 kΩ, for a Ti contact. However, other studies that employed a thin TiO$_2$ interlayer with different contact metals found what appeared to be even stronger pinning with the interlayer, as opposed to the expected reduction in pinning strength [35]. The stronger pinning also came with a reduced R$_C$; thus, it was concluded, and corroborated with modeling, that charge transfer from the TiO$_2$ interlayer effectively

dopes the MoS_2. The observed effect of the TiO_2 interlayer can then be thought of in terms of doping, and not FLP.

MoS₂ does have a metallic phase, the 1T phase. MoS₂ flakes and films have been phase engineered at device contact regions to create the 1T phase at the under the metal contacts, while leaving the channel in the semiconducting 2H phase. This was accomplished by soaking the MoS_2 in n-butyllithium, to allow for the lithium atoms to contribute an electron to the MoS_2 and induce the phase change to 1T. The 1T produced a very low contact resistance, however the 1T phase is only metastable with a relaxation energy of ~1 eV. The 1T phase will relax back into the 2H phase at 95°C, far below typical semiconductor process temperatures, making 1T- MoS₂ unsuitable as a real-world solution for MoS_2's contact resistance issues [36], [37].

Doping

A heavily doped contact region will produce a thin and potentially negligible barrier through which carriers can tunnel. As a means of reducing contact resistance, many doping methods for MoS₂ have been reported in literature, though these methods are typically unconventional due to the unique situation of dealing with a 2D film.

A common doping method for bulk semiconductors is to dope during growth, so that the dopants are inherently incorporated within the lattice. This method has been effectively utilized with MoS₂, even successfully yielding p-type MoS₂ by substituting 0.5% of the Mo atoms with niobium [38]. However, even if doping during growth is successful, it's still useful to be able to selectively dope specific regions, to allow for highly doped contact regions, or p-n junctions, or even for isolation. Thus, additional methods must be explored.

Numerous doping methods have been reported. Doping can be achieved by coating the surface in poly-vinyl alcohol, resulting in surface charge transfer and n-doping [39]. A similar method involves the use of polyethyleneimine rather than poly-vinyl alcohol [40]. Other large molecules, such benzyl viologen, can also be used to facilitate charge transfer [41].

Another reported method uses solution-based chlorine. MoS_2 is soaked in a solution of dichloroethane for extended periods of time [42]. The exact doping mechanism is not determined, but it's believed that Cl substitutes into preexisting sulfur vacancies, rather than the Cl sitting as an interstitial or adsorbate. Nevertheless, the report is an example of effective doping with the use of a single-atom species, as opposed to the previously mentioned molecular methods.

The mentioned methods have been shown to effectively dope MoS_2. However, the processes involved typically steps, such as an extended soak in a solution, that are not viable for current industrial flows. Additionally, it's unclear whether the materials involved can survive the thermal treatments required by industry.

Opportunities

There remains the need for a robust and flexible doping method for MoS_2, and for 2DMs in general. Ion implantation is a common and well-understood industrial technique. Tailoring ion implantation to the needs of MoS_2 would allow for a more seamless adoption into current manufacturing environments, relative to common reported doping methods. However, ion implantation has not been thoroughly examined as a doping method for MoS_2 and the important parameters are unknown. These parameters include the implant species, implant dose, implant energy, and post-implantation anneals. Therein lies an opportunity to research the topic and gain an

understanding of how each implantation parameter influences the structural and

electronic properties of the MoS_2.
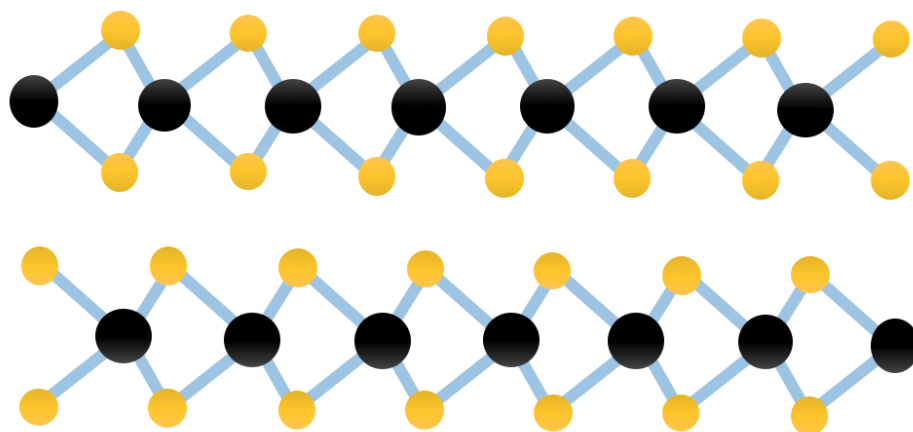
Figure 1-1. 2H-MoS$_2$ structure: side view. Two sheets are shown with the Van der Waals gap between them. The black circles are Mo atoms, while the yellow balls are S atoms.
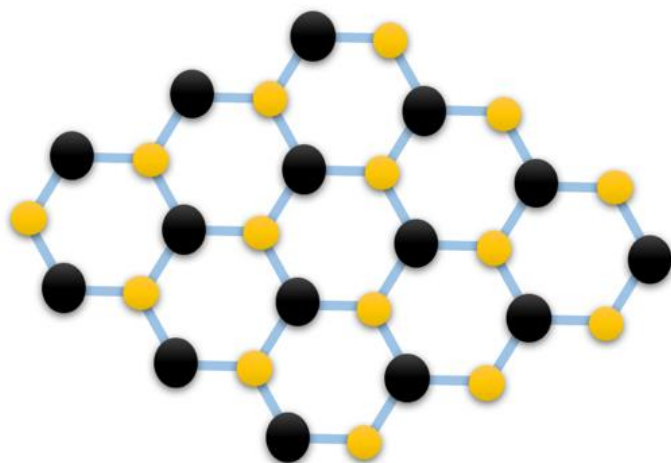
Figure 1-2. 2H-MoS$_2$ structure: Top-down view. The black circles are Mo atoms, while the yellow balls are S atoms. Two S atoms are on the same axis from this view, but only one is visible.
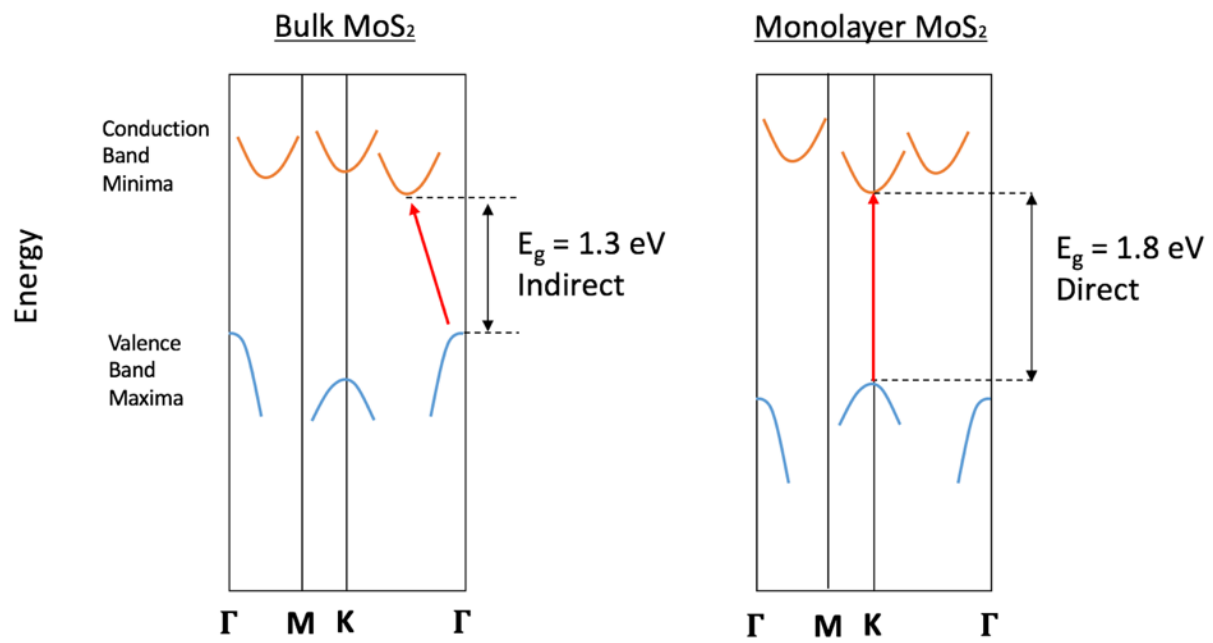
Figure 1-3. E-k diagram of the bandgap of MoS$_2$, and how it is influenced by layer thickness.

CHAPTER 2
STRUCTURAL AND CHEMICAL CHARACTERIZATION METHODS

A review of the characterized methods used to understand the experimental effects on the structural and chemical properties of the MoS_2 samples. First, the technique is introduced with a review of the theories and science underlying their operation. Next, examples are given for how the technique applies to MoS_2.

X-Ray Photoelectron Spectroscopy

Overview

X-Ray Photoelectron Spectroscopy (XPS) is a robust technique for probing the chemical environment of atoms on the surface of a sample. XPS is capable of detecting the surface chemical composition, excluding hydrogen and helium, with a detection limit typically in the range of 0.1-1%[43]. The basic, general theory of XPS can be summarized in Equation 2-1:

$$BE = hv - \left(KE - \Delta_p \right) \tag{2-1}$$

As illustrated in Figure 2-1, the sample is illuminated with x-rays of energy hv, with h being Planck's constant and v (the Greek letter nu) being the photon's frequency. Core electrons within the sample are excited by the x-rays and are emitted from the sample. Electrons emitted in this fashion are called photoelectrons (PE). A spectrometer then collects the PEs and measures their kinetic energy (KE). With the photon energy being known, subtracting out the KE of the PE gives the energy required to free the electron from its bound state; this energy is known as the binding energy (BE). The result is a collected PE intensity that peaks around the BE of the orbital from which that PE originated. Electrons originating from different orbitals, such as an s or p orbital, will yield different BEs. Likewise, orbitals that experience spin-orbit coupling (p, d, and f

orbitals) do not yield a single BE; rather, the BE is split into a closely spaced doublet. Binding energies for orbitals and their associated atoms have been exhaustively tabulated which allows for confident identification of the atomic species present in the probed sample [44]. However, chemical identification is not always straightforward: if orbitals from different atoms have a similar BE, or if a spin-coupled doublet is too closely space, then the peaks can overlap and obscure the individual peas. It is possible and common to deconvolve the final peak into its constituents, but for complex chemical environments the result may be left open for interpretation. The final term in Equation 2-1, Δ_p, accounts for the work function (WF) of the sample. Thus, as the sample's WF changes, the BE will shift and it becomes possible to detect such changes in doping. N-doping results in a decrease in sample WF and an increase, blue-shift, in the BE, while p-doping results in a red-shift of the BE.

When considering the depth that XPS probes, several important factors arise: namely, the escape depth of a PE, and the takeoff angle (TOA) of the PE (Figure 2-2). A PE can interact with anything it encounters on its way from its source to the detector, including the sample itself. This results in a probability for emission that diminishes exponentially with depth into the sample. This loss attenuates the detectable intensity and limits the depth probed by XPS to the top few nanometers of the sample's surface, regardless of how much larger the interaction volume of the x-rays with the sample is [45]. Additionally, a change in the TOA of the PEs, and incoming angle of the x-rays (both measured from the sample normal), will influence the average depth within which electrons will be minimally attenuated. As the TOA deviates from normal it will be attenuated by a factor of cosine of the TOA, which allows for varying the TOA and

probing different depths within the sample. Depth profiling in this manner is called angular-resolved XPS (ARXPS); a lower TOA, measured from normal, probes deeper into the sample compared to a higher TOA.

With XPS it is important to have a sufficiently conductive surface to provide a channel that allows for efficient transport and grounding of the generated photoelectrons. Otherwise, the PEs can build up on the sample surface and lead to so called charging effects that shift the entire measured spectrum; that is, the measured BEs will not correspond to that deduced from Equation 2-1. Additionally, the BEs can vary from sample to sample, which is important when trying to compare any BE shifts resulting from, for example, differences in doping among different samples. The solution to this problem is to align all the peaks to a reference value for an element that is both common to all the samples and that is unaffected by the experiment. The most common reference peak for this is the C1s peak of "adventitious carbon", or carbon remaining on the sample surface from air exposure. However, the C1s peak can be a dubious reference as it presents its own set of issues: the C1s peak is a convolved peak of all the carbon bonds from all carbon species present on the surface, including C-C, C-H, O-C=O, and C-O. While values such as 284.7 are commonly used as the reference, the variety of carbon species can vary from sample to sample and can depend on the film thickness (air exposure time), resulting in a C1s peak shift from 284.08 to 285.52 eV, measured on conductive surfaces that should have minimal charging [46]. The variation of 1.44 eV can be as much as an order of magnitude larger than the resolvable BE different chemical states of the same element. Deconvolving a peak into its separate constituents is possible but not always accurate. Additionally, there's evidence of

vacuum level alignment, rather than Fermi level alignment, for the C 1s peak, resulting in the C 1s BE being dependent on the work function of the sample, which can obscure a change in the sample's work function from the experiment.

For MoS_2, the relevance of shifting BEs and reference peaks is dependent on the thickness and width of the MoS_2 sample being studied. For exfoliated flakes, thickness can vary from monolayer (~0.65 nm) to many-layered (tens of nm), and the flakes lay on top of an oxide substrate, typically SiO_2. Thus, the probed depth can penetrate through the flakes and into the oxide. Additionally, exfoliated flakes vary in shape, length, and width, and can be anywhere form <1 µm2 to >100µm2 in area. Flakes smaller than the spot size of the x-ray beam (from 10-200 µm in diameter), can include potentially significant signal from the underlying oxide. As a result, for XPS on exfoliated flakes the Si 2s peak is sometimes used as the reference peak; O peaks being overlooked for the same multi-species and deconvolution issues as with the C1s peak[47]. However, for XPS on bulk MoS_2 that is much thicker than the probe depth and much wider than the x-ray spot size, aligning to C1s remains the best, or only, option.

Detailed Applications for MoS_2

The relevant BE peaks for MoS_2 occur for electrons in the following orbitals and at the following approximate BEs: Mo $3d_{3/2}$ (BE = 232.3 eV), Mo $3d_{5/2}$ (BE = 229.1 eV), S $2p_{1/2}$ (BE = 163.2 eV), and S $2p_{3/2}$ (162.0 eV) [48]. Representative examples of XPS performed on mineralogical are in Figure 2-3, Mo 3d peaks, and Figure 2-4, S 2p states. When MoS_2 is grown, for example by chemical vapor deposition, XPS is one technique used to confirm the synthesis of MoS_2 [49]. In addition to, and sometimes in lieu of, electrical results, XPS can be used to confirm n- or p-type doping effects through a respective blue or red shift in the molybdenum and sulfur BEs [50]. Another application

of XPS with MoS_2 is in using the relative intensity of the Mo and S peaks to observe S loss during high-dose argon irradiation [47].

Raman Spectroscopy

Overview

Raman spectroscopy (RS) characterizes molecular vibrational modes. At equilibrium, molecules within a sample will occupy a vibrational mode that is determined by their thermal energy. Additional vibrational modes may exist for the molecules, but energy barriers also exist between the different modes, which can prevent their occupancy. Excitation over the energy barriers is experimentally achieved by subjecting the sample to laser illumination, commonly performed using a 532 nm laser. Incident photons of sufficient energy can excite molecules into higher-energy vibrational modes. An excited molecule will subsequently relax to a lower-energy state by releasing energy, which can be in the form of an emitted photon. Detectors situated within the RS instrument then collect and analyze those emitted photons.

A molecule that has been excited to a higher-energy vibrational mode can relax in one of three manners: to a mode that is lower in energy than the initial mode (Stokes scattering), to mode that is higher in energy than the initial mode (anti-Stokes scattering), or to a mode with equivalent energy to that of the initial mode (elastic scattering). Raman spectroscopy relies on inelastic scattering of the incident photons. Thus, Stokes and anti-Stokes scattering are the relevant relaxation mechanisms for RS. A molecule that has experienced stokes scattering will eventually relax to the equilibrium mode by releasing energy. Typically, the occupied mode has energy close to that of the equilibrium mode, and energy is released in the form of heat. Anti-Stokes scattering occurs when a molecule already occupies a vibrational mode that has higher-

energy than the equilibrium mode, such as from thermal excitation. Upon excitation from an incident photon, the molecule can relax to a mode at a lower-energy than the initial mode, and emit a photon of higher energy than the incident photon.

At room temperature, most molecules are in their equilibrium vibrational state, which makes Stokes scattering much more likely than anti-Stokes scattering. However, both types of scattering are much less common the elastic scattering, where the incident and scattered photon energies are equal. In fact, only one in every 10^6-10^8 photons induce inelastic scattering in this manner, however modern laser produce high enough intensities to yield measurable results. The reliance of RS on inelastic scattering might imply that the data is presented relative to the incident photon, for example, as a simple shift in photon energy. However, this is typically not the case; data is expressed as the wavenumber of the detected photon, typically in units of cm^{-1}, which is directly related to the photon energy [51]. The photon/matter interaction induces a polarization of the electron cloud surrounding the nuclei, but beyond that it's necessary to induce motion in the nuclei in order to produce meaningful data.

Detailed Applications for MoS$_2$

The relevant vibrational modes for MoS_2 are the E^1_{2g} and A_{1g} modes (Figure 2-5). Due to RS's involvement with molecular vibrations, it becomes important to discuss the type of vibration that these modes represent. The E^1_{2g} mode is an in-plane vibration that arises from two S atoms vibrating in opposite directions relative to a Mo atom. The A_{1g} mode is an out-of-plane vibration again arising from S atoms vibrating in opposite directions. The distinction is important because it can make the modes sensitive to different phenomena. For example, peak of the modes are influenced by the layered nature of MoS_2 and the number of layers within the sample. Adjacent layers can

influence each other through long-range coulombic interactions, and they can also physically suppress the ability for atoms in a layer to vibrate. The result is a shift in the E^1_{2g} and A_{1g} peaks with changing number of MoS_2 layers. As the number of layers increases from the monolayer, the A_{1g} mode blue shifts while the E^1_{2g} mode red shifts. This provides a way for identifying the number of layers contained in exfoliated flakes [52]. Additional uses for RS with MoS_2 come in determining the crystal quality through the full width half maximum (FWHM) of a vibrational mode's peak. Defects present in a crystal can disturb the lattice and introduce local variations in atomic bond lengths, which alter their vibrational modes relative to a pristine lattice and increase the FWHM of a RS peak. Thus, defects such as grain boundaries, interstitials, or vacancies can all increase the FWHM of an RS peak. In this way, the RS peak FWHM can aide in improving MoS_2 growth techniques, as well as observing experimentally-induced crystal damage and repair [53], [54].

Photoluminescence

Overview

Like Raman spectroscopy, photoluminescence (PL) involves directing photons at a sample and measuring the photons that are emitted from the interaction between the incident photons and the matter in the sample. As a result, PL and RS are often performed in the same tool, though the mechanism underlying them are quite different and thus they provide complementary information. While RS relies on the excitation and relaxation of molecular vibrational modes, PL pertains to electrons. [55] An incident photon of sufficient energy, when absorbed by an electron, will excite an electron to a higher energy state. The electron subsequently relaxes and emits a photon of energy equal to the difference between the excited and relaxed state. For semiconductors,

typically the excited state is the conduction bad and the relaxed state is the valence band, though sometimes states near the bands, such as those from excitons, can contribute to PL at energies different from the bandgap (Figure 2-6). This emission process is also known as radiative recombination, but it's also possible for an electron to relax without emitting a photon in a process known as nonradiative recombination. Nonradiative recombination can occur when an additional state is created near the middle of the bandgap, typically from a defect, which provides a pathway for an electron to ease its way from the conduction band to the valence band without emitting a photon in the energy range being observed. A classic example of nonradiative recombination is gold dopants in silicon [56].

Detailed Applications for MoS$_2$

Two dimensional materials such as MoS$_2$ present an interesting case in regards to PL due to the influence of the sample's thickness on the sample's optical and electrical properties. For example, monolayer MoS$_2$ has a direct bandgap of about 1.9 eV, while bulk MoS$_2$ has an indirect bandgap of approximately 1.3 eV [57]. Thus, a significant decrease in PL intensity is expected with increasing MoS$_2$ layer thickness, and in fact it is observed even when the MoS$_2$ layer thickness increases from only one to two layers.[58] PL spectra for MoS$_2$ is comprised of two peaks: the A1 peak at ~627 nm (1.98 eV), and the B1 peak at ~670 nm (1.85 eV). These peaks result from a degeneracy in the valence band and a consequential spin-orbital splitting, which creates the lower energy resonance of excitonic optical transitions.[57]

Scanning Tunneling Microscopy and Spectroscopy

Overview

Scanning tunneling microscopy (STM) is a powerful technique that can provide analyses unlike any other technique. STM involves bringing an atomically sharp metallic tip to within a few nm of the sample's surface. Piezoelectric mechanisms allow for precise control of the tip's x, y, and z location. A bias is then applied between the sample and tip, and for an adequately conductive samples a current will tunnel between the tip and sample despite their lack of actual physical contact. The tunneling current will be exponentially dependent on the distance between sample and tip (Equation 2-2), where m is the mass of the electron, U is the energy barrier height, E is the energy of the electron, h-bar is the reduced Planck's constant, and w is the tunneling distance (tip-sample distance).

$$I \propto e^{-2\frac{w\sqrt{2m(U-E)}}{\hbar^2}}$$
(2-2)

After a tunneling current has been confirmed the tip is rastered across the sample in one of two modes: constant-current or constant-height mode. For constant-current modes, the tip's z height is allowed to change to ensure the tunneling current is held constant, and it is the tip's height that is measured. For constant-height mode, the tip's z height is held constant and the tunneling current is measured. The resulting image is a combination of the topology as well as the DOS of the material, and is also influenced by the shape and sharpness of the tip. For example, the tip is ideally atomically sharp but if two or more atoms are present at the tip then tunneling can occur at multiple places and lead to erroneous and blurred images. A positive bias applied on the tip will allow electrons from the tip to flow into empty states of the sample. Likewise,

a negative bias on the tip will allow electrons from occupied states within the sample to flow into the tip (Figure 2-7). Thus, it's possible to probe the occupied and unoccupied states of the sample by altering the tip bias. With scanning tunneling spectroscopy (STS), the tip is not rastered over the surface, rather it is situated at a specific location, the bias is adjusted from negative to positive, and the tunneling current is measured. In addition, the derivative of the tunneling current with respect to the applied voltage is directly proportional to the DOS of the sample, as shown in Equation 2-3. Thus, by plotting dI/dV vs. V it's possible to image the DOS at a specific location, such as on a defect or dopant site.

$$\frac{dI}{dV} \propto \rho_s(E_F - eV) \qquad (2\text{-}3)$$

Detailed Applications for MoS$_2$

STM and STS have been used on MoS$_2$ to identify single defects. Both naturally occurring defects and defects induced by irradiation damage. The results typically indicate an enhanced tunneling current in the negative biases, which represent an increase in the number of filled states. Additionally, the defect density can be estimated by counting the number of defects within the image frame. A STM image of the MoS$_2$ surface is shown in Figure 2-8, in which the surface lattice is atomically resolved.
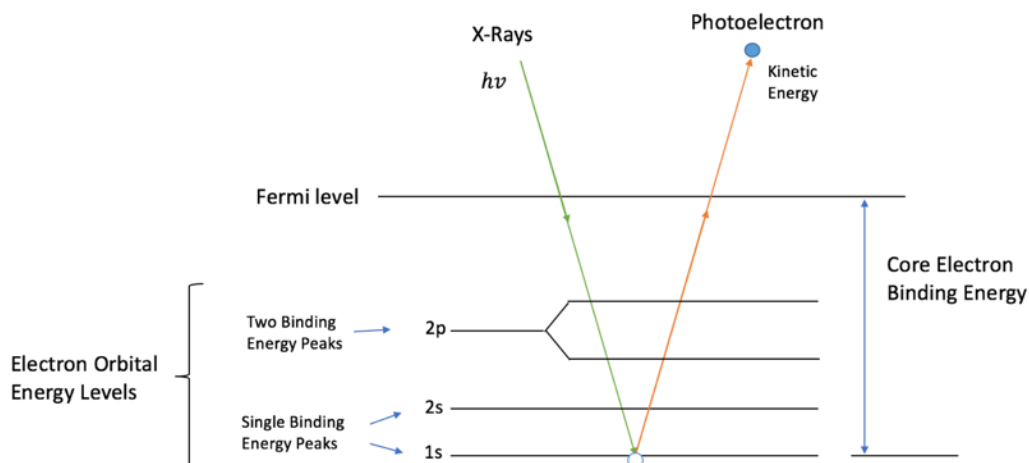
Figure 2-1. Illustration of the fundamental basis of XPS. Incoming X-Rays excite electrons. The electrons are emitted and their kinetic energy is measured. This allows for the determination of the electron's binding energy and the orbital from which it originated.
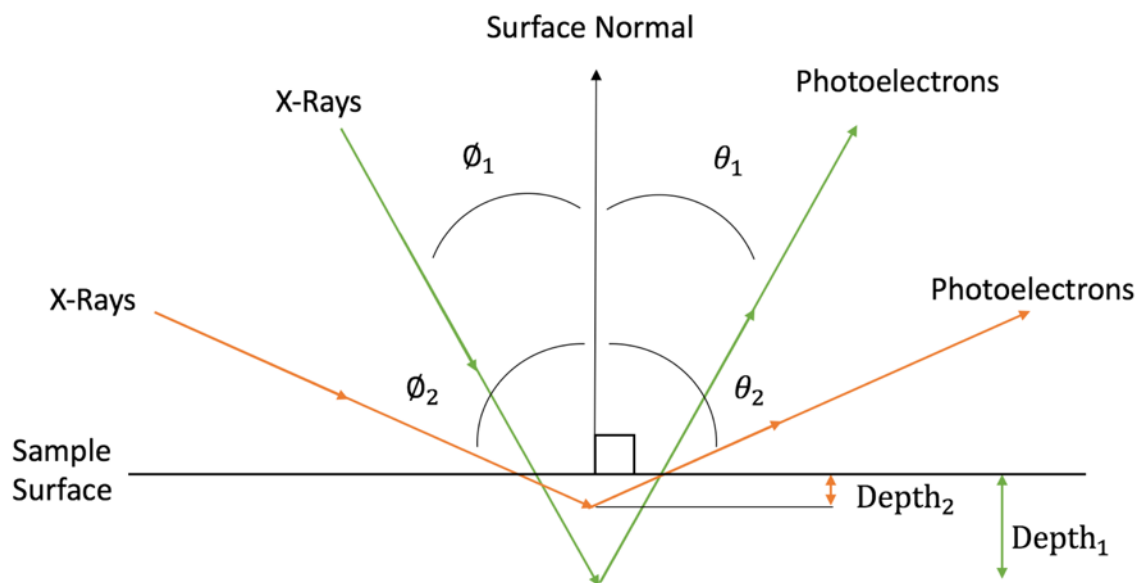
Figure 2-2. XPS relationship between the angle of incoming X-ray, the take-off-angle of the photoelectron, and the probed depth within the sample.
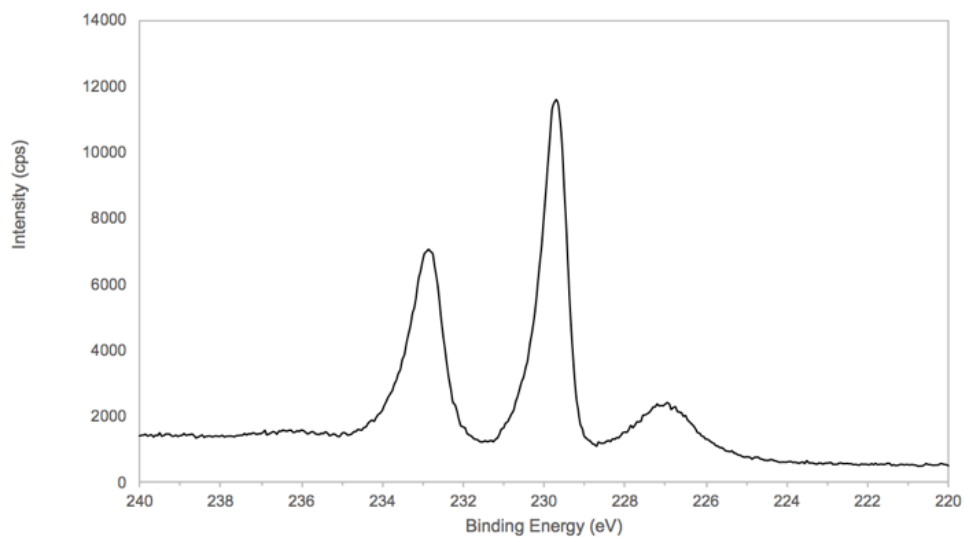
Figure 2-3. Example XPS spectra of MoS_2. Binding energies for Mo 3d doublet.
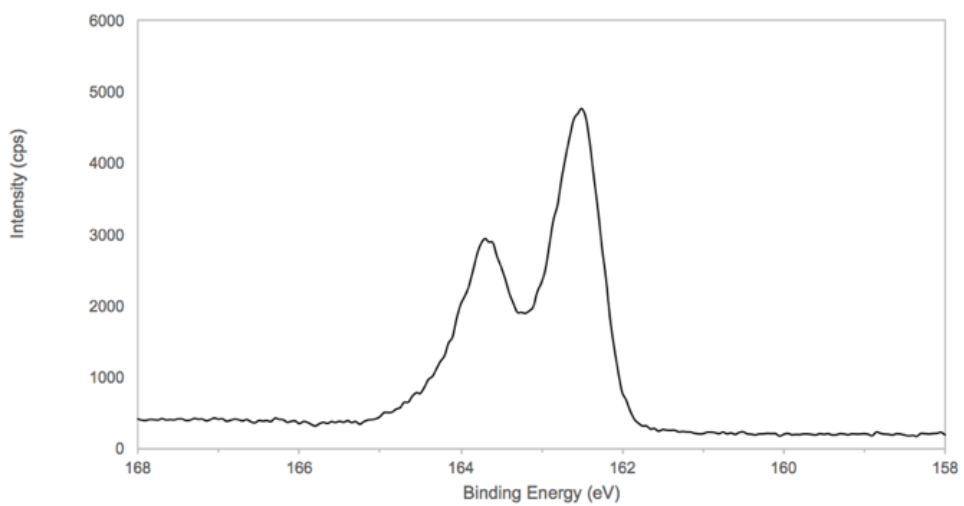
Figure 2-4. Example XPS spectra of MoS_2. Binding energies for the S 2p doublet.
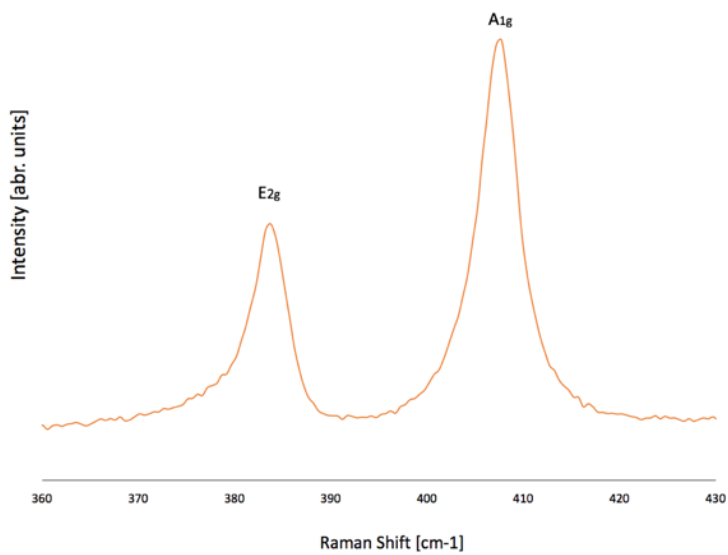
Figure 2-5. Example of Raman spectra in MoS_2 showing the E_{2g} and A_{1g} vibrational mode peaks.
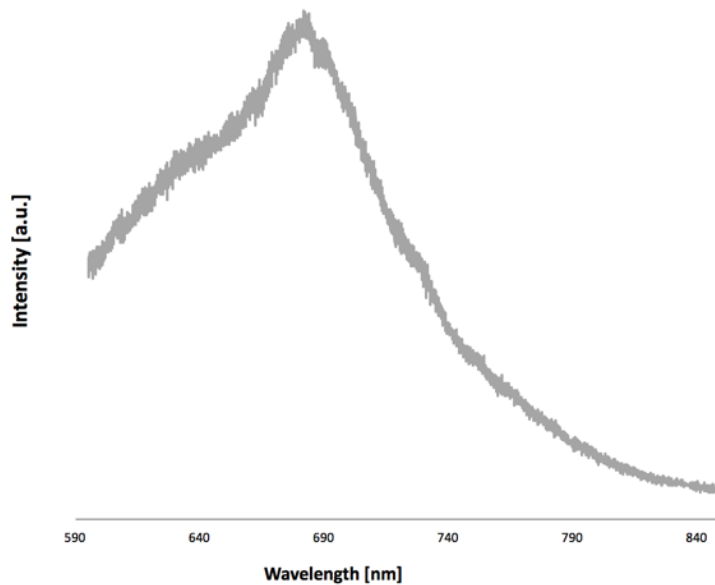
Figure 2-6. Example of photoluminescence spectra from MoS_2 showing the exciton peaks.
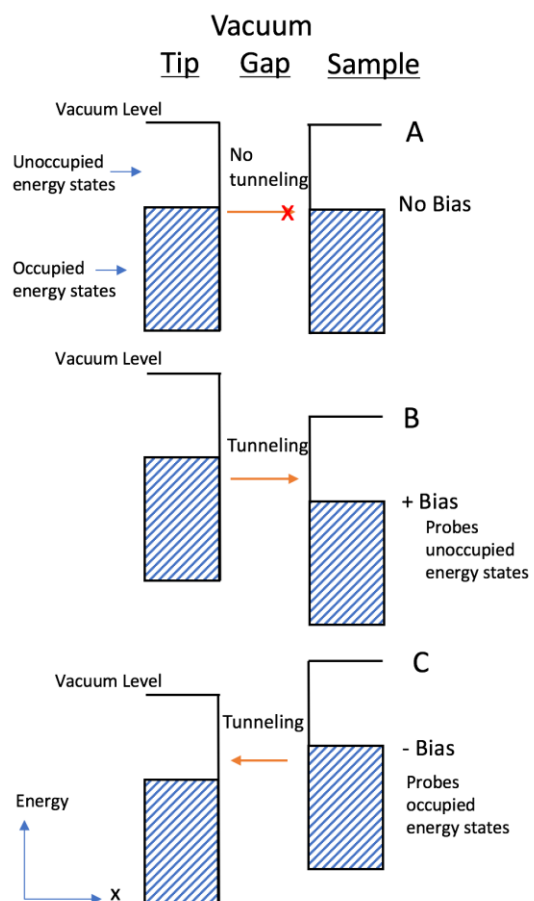
Figure 2-7. Depiction of the electron tunneling between a STM tip and a sample.

Figure 2-8. Example STM image of mineralogical MoS_2 surface. Atomic resolution is acheivable and the lattice is visible. Image courtesy of Xueying Zhao.

DEVICE CHARACTERIZATION METHODS

MoS$_2$ Devices

The typical structure of a MoS$_2$ device is shown in Figure 3-1. The substrate is degenerately doped Si capped with a layer of SiO$_2$. This combination offers many advantages. The oxide provides a gate dielectric and allows for optical contrast to develop between the substrate and MoS$_2$ flakes of different thicknesses. This makes it possible to identify thin MoS$_2$ flakes based on their thickness. The degenerately doped Si behaves like a metal and can conveniently be used as a gate electrode. Gating in this manner, where the gate influences both the channel and contact regions, is referred to as back-gating and is commonly used for measuring devices fabricated on 2DMs.

MOSFETs are often used to produce a transfer curve (Figure 3-2). A transfer curve is obtained by applying a constant voltage between the drain and source, V_{DS}, then sweeping the gate voltage over a desired range, and measuring the resulting I_{DS}. The transfer curve provides useful information, such as I_{ON}/I_{OFF}, the ratio between the on- and off-current. Additionally, the transfer curve can be used to determine the field effect mobility, μ, shown in Equation 3-1, by finding the slope in the linear regime. That is, the slope when I_{DS} increases linearly with V_G, rather than exponentially.

$$\mu = \frac{\partial I_{DS}}{\partial V_G}\frac{L}{W C_i V_{DS}} \tag{3-1}$$

For n-type devices like those made on MoS$_2$, the linear region occurs when V_G exceeds V_T. The slope of I_{DS} vs V_G in the linear region is the differential factor in Equation 3-1, and the x-axis intercept for the line-fit of that linear region provides an estimate of V_T. Calculating μ in this way will yield a lower estimate, since the contact resistance has not been accounted for. Knowing μ will then enable calculation of the 2D

carrier density, n_{2D}, shown in Equation 3-2. In these equations, L is the device channel length, W is the device channel width, C_i is the capacitance of the gate oxide, V_{DS} is the applied bias between the drain and source, and q is the elementary charge of an electron.

$$n_{2D} = \frac{I_{DS}L}{qWV_{DS}\mu} \tag{3-2}$$

Transfer Length Method

The transfer length method (TLM) is a relatively simple but powerful technique that can reveal important parameters such as contact resistance, R_C, and sheet resistance, R_S. TLM determines these parameters by effectively simulating the unrealistic resistance measurement within a single contact, where current flows through the contact, into the semiconductor, then back into itself to be measured, only encountering resistance terms by passing twice through its own metal-semiconductor junction.

TLM is performed by first patterning a series of electrical contacts on a semiconductor (Figure 3-4). The distance between consecutive contacts is the channel length, $L_{Channel}$, of the device that is defined by those two contacts. TLM requires the measurement of devices that have a different $L_{Channel}$, so the TLM row pattern requires that each consecutive pair of contacts be separated by a larger distance than that of the previous pair of contacts. Thus, $L_{Channel\ 1}$ is the shortest, $L_{Channel\ 2}$ will be longer, $L_{Channel\ 3}$ will be even longer, etc.

After device patterning, the resistance between each consecutive contact is measured and plotted as a function of $L_{Channel}$ (Figure 3-5), and a line is fit to the data points. The y-axis intersection of the line-fit then approximates a resistance

51

measurement between two contacts separated by zero distance. Thus, the y-axis intersection is equal to twice the contact resistance.

Resistance measured between two contacts on a semiconductor can be approximated by a contribution from each contact, R_C, and a contribution from the resistance of the channel, $R_{Channel}$, as shown in Figure 3-1 and Equation 3-3. The channel resistance in Equation 3-3 can be broken down into its components (Equation 3-4), where W is the channel width (Figure 3-4). The terms can be further broken down into Equation 3-5, where ρ_c is the specific contact resistivity (units of Ω/cm^2) and L_T is the transfer length.

$$R_{Measured} = 2R_C + R_{Channel} \tag{3-3}$$

$$R_{Measured} = 2R_C + R_S \frac{L_{channel}}{W} \tag{3-4}$$

$$R_{Measured} = 2\frac{\rho_C}{WL_T} + R_S \frac{L_{channel}}{W} \tag{3-5}$$

Current flowing through the metal- semiconductor junction will crowd at the edge. Thus, more of the current is located closer to the edge, such that at a distance of L_T from the edge of the contact the current will have reduced by a factor of 1/e, or 63%, rather than dropping in a linear manner (Figure 3-6). If the contact is much longer than L_T, then effective area of the contact-semiconductor junction can be approximated as W multiplied by L_T, rather than W multiplied by the length of the contact, since the length portion beyond L_T will contribute less than the L_T portion [59].

Error Analysis

TLM involves fitting a line to data points, for $R_{Measured}$ (y-axis) plotted against $L_{Channel}$ (x-axis). Variation in the data points can result in a poor line-fit, which will add

error and uncertainty to all parameters derived from that line, such as R_C or R_S. This issue can be addressed by performing regression analysis on the data points and line-fit. The actual data points will occur at values different than what the line-fit estimates. For the entire data set, the average magnitude of that difference is called the standard error of the estimate (SE_E) [60]. Equation 3-6 shows the calculation of SE_E for a line-fit, where Y is an actual data point, Z is the data point predicted by the line-fit, and N is the number of data points used for the line-fit.

$$SE_E = \sqrt{\frac{\sum(Y-Z)^2}{N}}$$

(3-6)

SE_E is similar to standard deviation in that they both reference an average distance of data points from a metric, however the standard deviation relates to the mean of those data points, while SE_E relates to their estimated values. SE_E can be used to determine the standard error in the slope and in y-intercept of the line-fit, which will determine the error in the values estimated from the line-fit.

The standard error of the estimate is not to be confused with the standard error of the mean, SE_M, which is useful when dealing with the mean of a data set [61]. An entire population of data points will have an overall mean. However, a subset of data points, taken from the overall population, will have a mean that differs from that of the overall population. SE_M relates to the mean of data subsets, and the average variation of those means compared to the mean of the overall population. SE_M is calculated in Equation 3-7, where Y is a data point in the data set and M is the mean of the data set.

$$SE_M = \sqrt{\frac{\sum(Y - M)^2}{N(N - 1)}} \qquad \text{(3-7)}$$

For both SE_E and SE_M, a lower value relates to a greater certainty in the result related to that error. Both errors are inversely proportional to the size of the sample population, thus, large sample populations are preferred to ensure certainty in the results. SE_E will be used to analyze the error in TLM experiments, as it relates to error in line-fits, and the resulting estimated values for R_C and R_S. SE_M will be used to analyze error when taking the mean of a data set, such as when determining the average mobility or 2D carrier density of a set of devices that have undergone a similar treatment. In such cases, the mobility value will be taken from multiple nearby points around a single point on the I_{DS}-V_G transfer curve, to account for error in determining the slope of the linear region.
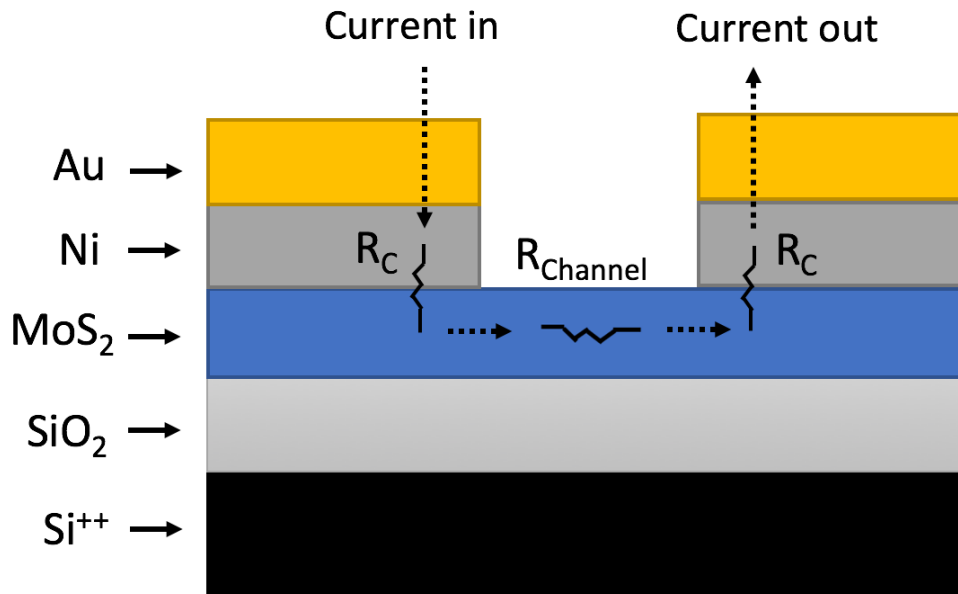
Figure 3-1. Typical structure of a MoS$_2$ device, not drawn to scale. The substrate is Si++/ SiO$_2$, and the contacts are Ni/Au.
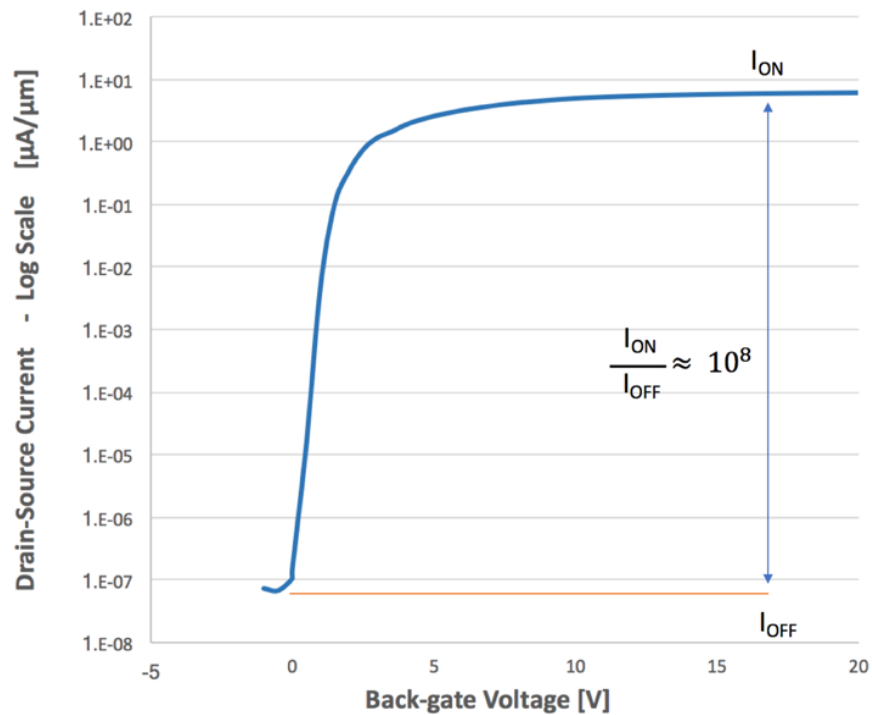
Figure 3-2. Typical transfer curve for a MoS$_2$ field-effect transistor, with the y-axis on a log scale. V$_{DS}$ is held constant..
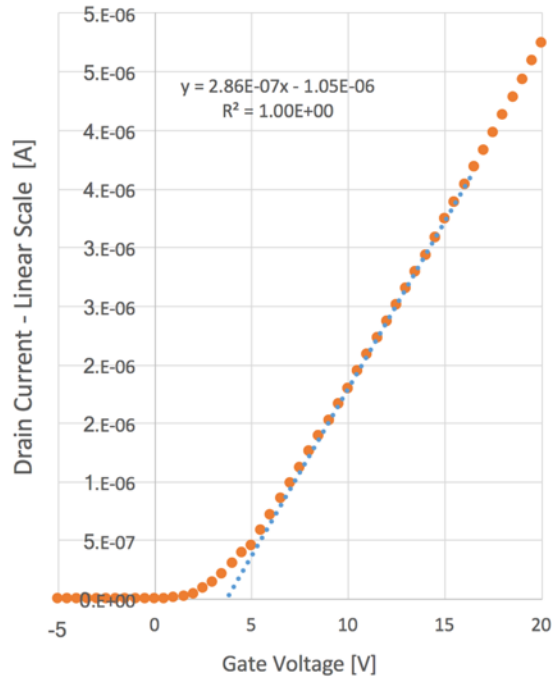
Figure 3-3. Typical transfer curve for a MoS$_2$ field-effect transistor, with the y-axis on a linear scale. A line-fit to the linear portion can determine the slope, which can then be used to calculate the field-effect mobility, μ.
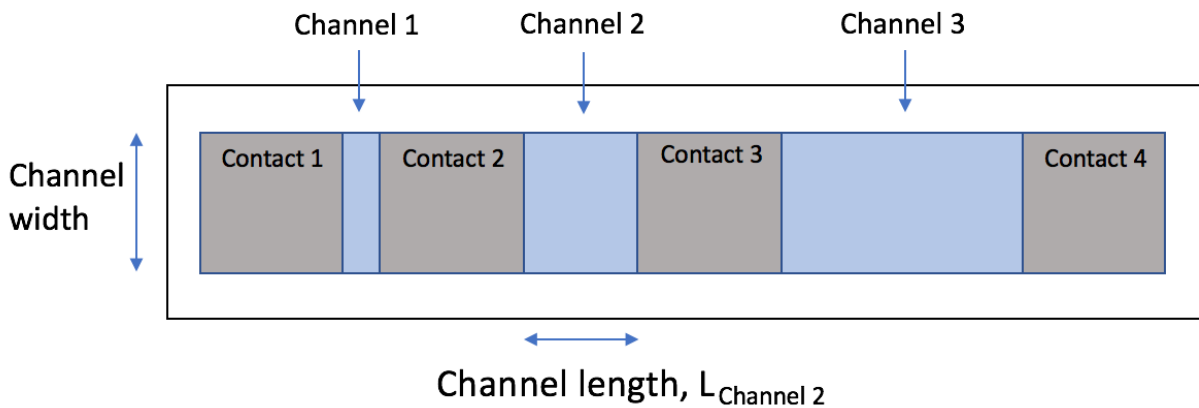
Figure 3-4. Basic TLM design. A row of boxes, with an increasing gap (channel length) between consecutive boxes.
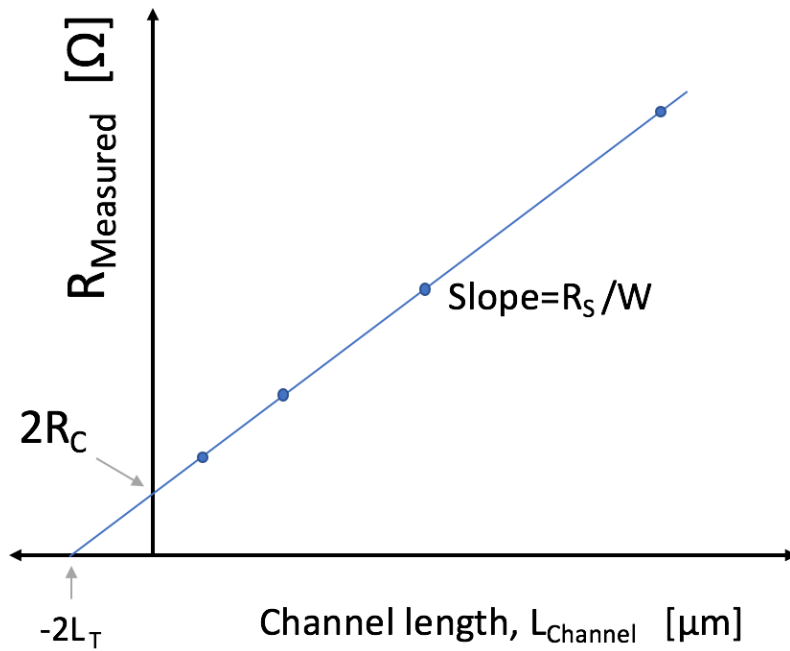
Figure 3-5. Representation of TLM data and analysis showing the relationship between a linear fit of the data points and various device resistances.
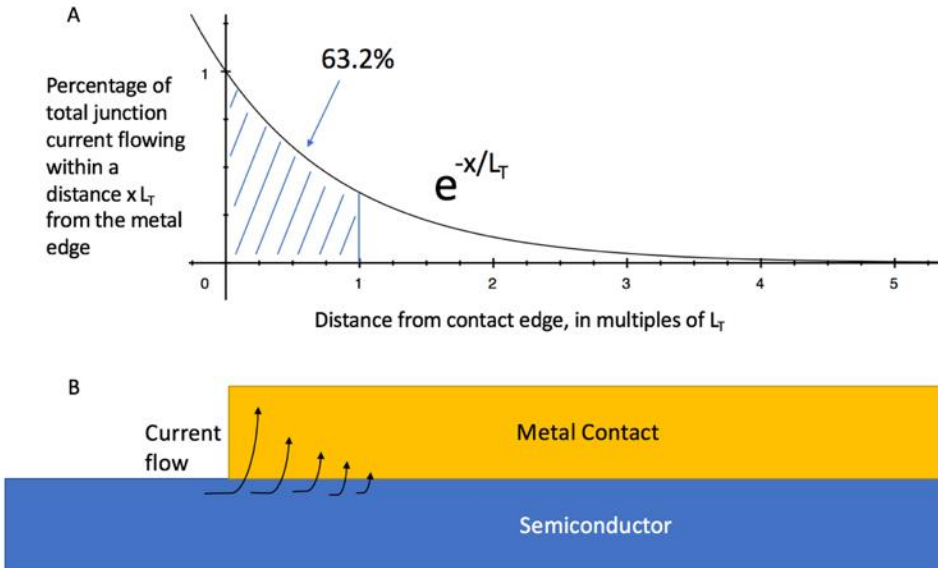
Figure 3-6. Depiction of L_T, the transfer length. Current flowing through a metal-semiconductor junction will crowd at the metal edge. The percentage of total current flowing through the junction at a distance xLT will be $\exp(-x/L_T)$.

CHAPTER 4
SAMPLE PREPARATION AND PROCESSING TECHNIQUES

MoS_2 Material

Working with MoS_2 for microelectronic purposes requires isolating it into sheets of few-layer thickness. This is typically accomplished through one of two ways: mechanical exfoliation from a bulk mineralogical crystal, or through the growth of a thin MoS_2 film. The mineralogical origin of mechanically exfoliated samples generally yields superior electronic and optical properties when compared to grown films, due to defects in the films that result from the growth process [4]. However, running experiments on grown films can be quicker than with exfoliated flakes, due to the random shapes, thicknesses, and arrangement of flakes that exfoliation produces. Therefore, both methods have their advantages and disadvantages, but ultimately if 2DMs are ever to achieve widespread adoption then effective growth methods must be developed. Until then, exfoliated mineralogical flakes fill a useful role in laboratory settings.

Mechanical Exfoliation

Mechanical exfoliation is a simple process that nonetheless was significant enough to yield a Nobel Prize in 2010 [62]. The process involves using a sticky material, such as tape, to peel off sheets of 2DM from a bulk crystal [63]. A piece of tape is pressed on and peeled off from a bulk crystal of the 2DM. This results in a competition between the attractive forces at the different interfaces: the tape-sheet interface (for the outermost sheet that is touching the tape) and the sheet-sheet interfaces (for the sheets that are touching each other). When peeling off the tape, at some distance into the depth of the 2DM the competition of forces reaches a turning point. The 2DM sheets below that point will remain on the substrate, while the sheets above it will exfoliate with

the tape. The separation is highly random and can depend on the peeling motion as well as any defects present in the material that could provide a weak point for fracture to occur.

After the initial exfoliation, the material remaining on the tape can be quite thick so it's necessary to thin the material by pressing on and peeling off tape in repeated exfoliation steps. The tape with the thinned material is then placed onto a substrate and peeled off. The adhesive force between the tape–MoS_2 and substrate–MoS_2 is sufficient enough that, upon peeling the tape off from the substrate, sheets of the 2DM remain on both the substrate and tape. In this way, the 2DM surface that is exposed on the substrate after exfoliation is pristine; it has never touched the tape, it has only touched an adjacent sheet of 2DM.

Exfoliation yields a stochastic distribution of 2DM 'flakes', which is a general term used to describe a randomly shaped and randomly thick piece of 2DM. Exfoliated flakes are randomly arranged over the surface of the target substrate. Flakes can vary in area from less than a micron squared to tens of microns squared, and vary in thickness from monolayer to tens of layers. A macroscopic image of exfoliated flakes on a Si/ SiO_2 substrate is shown in Figure 4-1.

Optical Contrast and Flake Thickness

The ability to quickly and accurately determine the thickness of a 2DM flake is important due to the thickness having significant effect on the material's electronic and optical properties [64], [65], [66], [10]. Rigorous techniques involving atomic force microscopes or electron microscopes can accurately determine flake thickness, however they are generally too time consuming for practical use when absolute

precision of thickness is not necessary, such as when making devices on few-layer flakes.

A much quicker method exists using the color, or optical contrast, of the flake [67]. The typical substrate for exfoliated flakes is Si/ SiO_2, which upon exfoliation results in a Si/ SiO_2/ MoS_2 stack where each layer has a unique index of refraction. Light passing through each layer will experience a phase shift that is dependent on the thickness of the layer and the layer's index of refraction. There is also a chance for the light to reflect at the interface between each layer, dependent on the index of refraction of each layer at the interface. The combination of phase shift and reflection induces interference between light that is reflected from different interfaces, which produces contrast. Contrast in this sense is refers to the relative intensity of reflected light, comparing where the 2DM is and isn't present on a substrate. The contrast is thus dependent on the thickness of the SiO_2 layer and the thickness of the MoS_2 layer (as well as the wavelength of illuminated light, and the index of refraction of each layer in the stack).

Considering SiO_2 thicknesses below 300 nm and keeping everything constant aside from the SiO_2 thickness, this sets up three situations that are dependent on SiO_2 thickness: high MoS_2 contrast (SiO_2 of thicknesses 50-100 nm and 200-300 nm), low MoS_2 contrast (SiO_2 thicknesses of 130-160 nm), and no MoS_2 contrast (SiO_2 thicknesses of 0-50, 100-130, and 160-200 nm). Additionally, since the phase shift is dependent on the wavelength of the incident and reflected light, different wavelengths will be shifted and interfered with at different amounts. The overall result of this wavelength-dependent phase shift is that a color emerges to our eyes, a color that, with

all else constant, depends only on the thickness of the 2DM flake. This color can be

quantified by imaging the flakes in an optical microscope and using an image

processing program to separate the light into its red, blue, and green components, and

comparing the intensity of each component from different flakes to the intensity of the

bare Si/ SiO_2 substrate [68]. Once a flake color is corresponded to a flake thickness

using a precise measuring tool such as an electron microscope, that color can reliably

be used to identify other flakes of the same thickness.

Grown MoS$_2$ Films

Experiments performed in Chapters 6 and 7 used large-area MoS_2 films grown

by a group at the Interuniversity MicroElectronics Center (IMEC) in Leuven, Belgium

using a published method of Mo sulfurization [69]. To start, thin Mo films were deposited

on a sapphire substrate and annealed in 10 mbar of H_2S at 800˚C for 30 minutes,

followed by an additional 20 minute anneal at 1000˚C under a H_2S/N_2 flow. Sulfur in the

H_2S reacted with the Mo film and resulted in 3-5 layer thick 2H phase MoS_2 films that

were oriented parallel to the substrate. The films were then transferred onto highly

doped Si substrates that had been capped with 90 nm of SiO_2, which are the typical

substrates for device fabrication. Transfer was found to be necessary because films

grown directly on SiO_2 were inferior to those grown on sapphire. The transfer process

involved deposition of a polymer on the MoS_2 film, to provide mechanical support. A

corner of the film was scratched and it was submerged in water. The water penetrated

the MoS_2 /substrate interface and allowed for the MoS_2 film to be lifted off and

transferred to the desired substrate. Finally, the polymer was dissolved in toluene [70].

Cross-sectional transmission electron microscopy images confirmed the 3-5 layer

thickness of the film. Electron diffraction patterns (measured from the film yield well-

defined spots, which is indicative of a crystallographic film. However, atomic force microscopy characterizations of the surface show textured grains and terraces that vary in width from 10-100 nm. Electron spin resonance (experiments determined that these grains contain antisite defects where S or S_2 substitute for a Mo atom, with an estimated frequency of 1.5-3.5 antisite defects per 10 nm of grain boundary length [71]. It's these grain boundaries that are implicated as the source for degraded mobility (~3 cm^2/Vs) of devices made on these films, which is much lower than the theoretical maximum room temperature value of over 400 cm^2/Vs, or the more common value of 10-100 cm^2/Vs attained for exfoliated mineralogical flakes [72], [73], [74]. Notably, the reported mobility of 3 cm^2/Vs was only achieved after capping with Al_2O_3, which has commonly been shown to improve device performance through the suppression of charge impurity and phonon scattering effects, as well as any influence that environmental adsorbates may have (typically p-type doping) [75], [76], [33], [77], [78]. Despite the low mobility of the films, they can still yield devices with respectable I_{ON}/I_{OFF} ratios of 10^6.

The mentioned grain boundaries inherent in these grown films have a particular relevance for implantation and annealing studies. Their precise impact is unclear, but their potential impact relates to the diffusion of the dopant atoms. Activation anneals are intended to provide the thermal energy to allow for dopant substitution. It's conceivable that the grain boundaries could getter the dopants or even provide a pathway for speedy out-diffusion from the sample [79], [80], [81]. Either case could inhibit effective dopant activation.

Device Fabrication

Lithography

Lithography is common process for patterning designs on a semiconductor surface. Two types of lithography will be described here: masked photolithography (MP), maskless photolithography (MLP). The basic overall process is the same for each method, though important differences exist in the details. The general process involves depositing a polymer resist and exposing selected regions to UV light or an electron beam, and immersing the sample in a developer to remove unwanted resist regions (either exposed or unexposed areas, depending on the type of resist). This process leaves a pattern in the resist and prepares the sample for subsequent processes, such as metal deposition or etching. After a subsequent process, such as etching, the PR is simply dissolved, or "stripped", away. Following a process such as metal deposition, the PR is also dissolved away but the solvent is potentially different than that used for simple PR stripping, and the process is generally referred to as "liftoff"; the metal on the developed region remains, while the metal on the undeveloped PR is "lifted off."

The first step in lithography is the deposition of a resist, often and generally referred to as photoresist (PR) even if the process isn't optically based (such as with and electron beam lithography). PR is a polymer suspended in a solution. Deposition is performed by standard spin coating methods [82], where the substrate is held on a chuck via a vacuum, the PR solution is dropped on to the substrate, and the substrate is spun at a specified speed for a specified time. Importantly, prior to PR deposition it is common in lithography to apply a primer, such as hexamethyldisilazane, to improve adhesion between the PR and substrate. This step was avoided for the experiments

presented in this dissertation to prevent the primer from influencing the results, due to the 2DM's ultra-thin channel and sensitivity to the environment.

For optical lithography, two types of resists exist: positive and negative PR. With positive PR, exposure to UV light or an e-beam induces a breakdown in the PR polymer chains which makes the exposed region more soluble in the developer. Thus, with positive PR, the exposed region is removed by the developer. With negative PR, exposure induces crosslinking of the PR polymer chains, making that area less soluble in the developer. Thus, with negative PR, the exposed region remains and the unexposed region is dissolved upon immersion in the developer. This distinction is simple but important: certain processes are aided using a negative PR, but the laboratories where these experiments were conducted only had access to positive PR.

Specifically, when the light interacts with the PR during exposure there is a decaying magnitude of exposure through the depth of the PR due to the absorption of light, necessitating a large enough intensity of incident light to ensure proper exposure through the depth of the PR. At the edge of the exposed region the intensity of light is not enough to expose through the entire depth of PR, which leads to a profile that slopes away from the incident beam. When exposing a pattern in positive PR the profile at the exposed edge results in a continuous surface along a path that crosses from exposed region to unexposed region. Exposure of negative PR results in a non-continuous surface when traveling form the exposed to unexposed regions. This discontinuity is referred to as an undercut. For subsequent processes, such as etching an undercut might not be necessary, but for common lithographic processes such as metal deposition and liftoff, an undercut is critical. After metal deposition and during

liftoff, the continuous surface created by positive PR will result in a continuous metal surface and will introduce potential problems: the entire metal surface could remain after liftoff, or the entire metal film can be lifted off; both issues can ruin the patterns.

Negative PR mitigates these issues with the undercut: the discontinuous surface ensures that the metal deposited into the developed PR region is unaffected by the liftoff od the metal that is on top of the undeveloped PR. Thus, negative PR is critical for liftoff. However, as mentioned, the laboratories used in the experiments presented here only have access to positive PR. The solution to this issue involves the use of a liftoff resist (LOR). The LOR is deposited on the sample surface prior to deposition of the PR, and it is largely unaffected during exposure. The LOR is dissolved in the developer so a slightly longer development time is required when using an LOR. Dissolution of the LOR occurs in a manner that creates an undercut and allows for the use of positive PR with liftoff processes.

Masked and Maskless Photolithography

While the overall process is similar, MP and MLP differ in their exposure steps. Both methods have their advantages and disadvantages. MP is a parallel process where the entire pattern is exposed at once, so it is fast but it requires a pre-made mask, which limits the flexibility of designs you can make. MLP is a serial process that "draws" the pattern as it exposes. The serial nature of MLP makes it slower than MP, but it allows for designing unique patterns, and relatively easily, so it is a more flexible process than MP. The flexibility of MLP makes it very useful when patterning devices on exfoliated MoS_2 flakes, due to the random shape and size of flakes that result from exfoliation. On the other hand, grown MoS_2 films don't require uniquely shaped devices,

so MP is sufficient for making devices on grown films. An example of devices made on exfoliated MoS$_2$ flakes using MLP is shown in Figure 4-2.

Ion Implantation

General

Ion implantation is a process by which atomic species are incorporated into a substrate. It's a widespread and mature technology that offers precision and flexibility. Common uses include selected-area doping or electrical isolation of a region by inducing a significant increase in local resistivity. More exotic use cases do exist, such as the Smart Cut process, which allows for the production of uniform thin films that are readily transferable to other substrates in a manner that would be difficult or impossible to replicate through other methods [83].

Ion implantation employs an electric field to accelerate and guide an ionic species into the target substrate. The energy in the electric field imparts a kinetic energy (KE) to the ions based on the ion's charge. The ions then transfer that KE to the atoms in the target substrate. The transfer of KE and slowing of the incoming ion occurs through two methods: nuclear and electron stopping. Nuclear stopping dominates at lower ion KE and it results from the binary collision between the ion and the target atom's nucleus. Electron stopping dominates at higher implant energies and can potentially involve numerous processes, such as the promotion of a valence band electron into the conduction band or even ionization of the target atom, thus the electronic structure of the target atom will influence which mechanisms occur. With the low implant energies used for the experiments performed in this dissertation, nuclear stopping is expected to dominate. For clarity, unless otherwise stated, the implanted ion

will be referred to as ion regardless of its charge state throughout the course of its interactions.

The probability for a binary collision between the ion and a substrate atom is related to a term called the cross section, σ, which can be thought of as an interaction area surrounding the substrate atom. As implant energy increases, so will the ion's KE and velocity, resulting in less time for an ion-atom interaction to occur. Consequently, σ, and the chance for an ion-atom interaction, will decrease with increasing ion KE [84].

Sufficiently low ion KE can result in the ion reflecting from or absorbing to the target surface, which will result in minimal if any damage to the target. However, if the energy transferred from the ion to the target atom, T, exceeds the displacement threshold energy of the target atom, E_D, then the target atom will recoil and be displaced from its lattice site. The displaced atom is then referred to as the primary knock-on atom (PKA). If T is less than E_D, then the transferred energy will dissipate as heat that vibrates the target lattice.

Displacement of an atom from its lattice site involves breaking the chemical bonds it shares with its neighbors; thus, it might be expected that E_D is comparable to the sum of those bond energies (for example, 10-12 eV). However, E_D can be more than double the sum of bond energies due to non-idealities that arise in the collision process, including but not limited to scattering of the PKA in directions other than that of least resistance. Optimal scattering directions will depend on the local arrangement of nearest neighbors to the PKA, hence E_D can be influenced by the crystallographic orientation [85].

Energy and momentum are conserved during the ion-PKA collision, leading to a maximum possible transfer of energy, T_{max}, that depends on the relative masses of the participating species. An expression for the non-relativistic T_{max} is given in Equation 4-1, where m is the mass of the ion, M is the mass of the target atom, and KE is the energy of the incoming ion.

$$T_{max} = E \frac{mM}{(m+M)^2}$$ (4-1)

From that, it's possible to determine the minimum initial KE required for the ion to displace the target atom, as shown in Equation 4-2 [86].

$$E_{min} = T_{max} \frac{(m+M)^2}{mM}$$ (4-2)

A complex parade of events can occur following displacement of the PKA. If the collision occurred near the surface, there is a chance for the ion or the PKA to sputter from the substrate. Otherwise, they will continue traversing through the substrate's lattice in a random path where they will inevitably interact with additional substrate atoms. Each interaction with a lattice atom provides a chance for that atom to vacate its lattice site and recoil on its own random path of interactions. In this manner, a cascade of collisions and recoils can unfold, with potential for significant damage to the substrate's crystal lattice.

Each interaction reduces the overall kinetic energy of the system. Eventually the energy will have spread out enough so that lattice atoms are no longer encouraged leave their site, and the cascade will stop. The concentration of implanted ions will come to rest in an approximate Gaussian profile as a function of depth into the target

substrate. The peak of this profile is termed the projected range, R_p, and the standard deviation is the straggle, ΔR.

The implanted ions at this point are sitting interstitially, but for them to contribute to doping they need to substitute, or "activate", onto a lattice site. Such activation requires motion, not only of the implanted ions to a lattice site, but also of the lattice atoms from their lattice site. Thus, post-implantation anneals are required to "activate'" the dopants, with the added benefit of thermally repairing some of the implantation-induced damage. Oftentimes, adequate motion will occur at approximately three-quarters of the target's melting point. Such high temperatures can lead to undesired diffusion of the implanted species deeper into the substrate. This can be avoided, or at least minimized, by employing rapid thermal processes that use a higher temperature for a shorter amount of time to minimize diffusion.

The key process parameters for ion implantation are the species, the energy, and the dose. Species are chosen based on their n- or p-type doping ability, though inert noble gasses can be implanted to observe the damage effect of implantation without chemical doping. Common implant energies range from the tens of keV to MeV, and typical doses range from 1 x 10^{12} cm^{-2} to 1 x 10^{18} cm^{-2}. Finally, key process parameters for the post-implantation anneal are the annealing temperature and time, as well as the annealing atmosphere.

Detailed Applications for 2D Materials

Implantation into bulk silicon is a well-known process. However, the same rules do not always apply for low-dimensional systems. For example, the cross section, and thus the probability, for a binary collision to occur between an ion and target atom was

said decrease with increasing ion energy. For bulk semiconductors, this means the ion will travel deeper into the substrate, but ultimately the ion will stop and its kinetic energy will be dissipated into the substrate. Thus, the substrate will still experience the full extent of damage that results from absorbing the larger kinetic energy, and damage will increase with implantation energy. This is not the case for 2D materials. Initially, the damage (in the form of sputter events) does increase with increasing implant energy. However, the increasing energy will eventually cause the cross section for a collision to decrease, at which point fewer collisions occur. At high energies, the implanted species will come to rest in the substrate underneath the 2D material, and the 2D material will experience less damage (fewer sputter events) as the implantation energy increases. Damage typically peaks for energies between 100-1000 eV, depending on the implantation species [87].

This discrepancy between 2D and bulk material is observed when attempting to model and predict implantation. Bulk implantation is reliably modeled using software such as the Stopping Range of Ions in Matter (SRIM). However, SRIM assumes the target is amorphous and of a homogenous density. There is a Van der Waals gap between each sheet in a 2D material. This, combined with the aforementioned reduction in collision cross section with increasing implantation energy, leads SRIM to overestimate the number of implantation-induced defects by as much as four times. In some cases, such as for a carbon nanotube, tweaking the target density allowed SRIM to predict the correct number of defects, though that did not work for graphene [88]. It should be noted, despite these discrepancies with SRIM and 2D materials, SRIM has accurately predicted the projected range for implantation into carbon nanotubes [89].

Regarding the cross section, for 3D materials it is commonly based on the cross section for Coulomb scattering between an electron and a nucleus that was developed by Mott in 1929 and later refined by McKinley and Feshback [90], [91]. It assumes the target atom is at rest. When fitted for graphene, it yielded a sharp onset of T_D at 108 keV, whereas experimental evidence on suspended graphene suggested a gradual onset beginning at 80 keV. However, the model was accurate after it was adjusted to account for graphene's atomic vibrations. It was concluded that the vibrating atom could receive a higher maximum transferred energy than predicted in Equation 4-2, which resulted in the experimentally observed reduced T_D. This example might be an especially distant outlier, since suspended graphene has been shown to have unique vibrational properties compared to non-suspended graphene, where contact with the substrate might inhibit vibrations [92]. Nevertheless, it does give hope to the notion that only a slight modification is needed to for standard 3D models to accurately describe 2D materials.

Additional differences between 2D and 3D materials that may influence ion implantation regard the high surface-to-volume ratio inherent to 2D materials. For implantations normal to the surface, the implantation energy that produced the most defects was in the 100-1000 eV range. Such low energies will focus the ion stopping, and therefore the most damage, into the near-surface region. This could lead to an enhanced sputtering yield. This could be particularly relevant for the experiments described later in this dissertation, as they employed implantations normal to the surface and implantation energies within that range. Additionally, the high surface-to-volume ratio combined with the enhanced diffusion pathways of the Van der Waals

gaps could have implications on post-implantation anneals, especially when annealing

in an H_2S atmosphere. S diffusion through the gap was modeled to have a low energy

barrier of only 0.08 eV, allowing S to easily reach subsurface implantation-induced

sulfur vacancies [93].
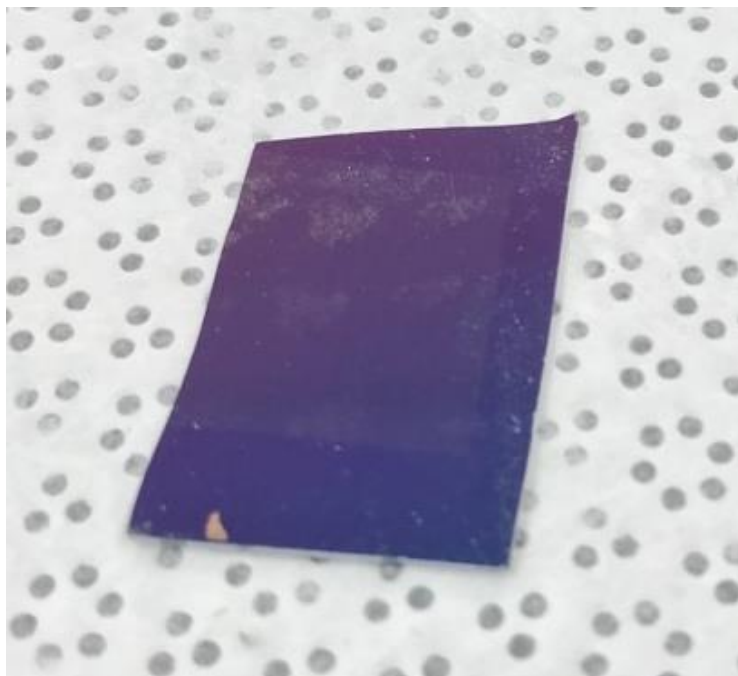
Figure 4-1. Macroscopic picture of a Si/ SiO$_2$ susbtrate on which MoS$_2$ has been mechanically exfoliated. The flakes are only microns in size but large groups of them are visible as the smudges on the substrate. Photo courtesy of author.

Figure 4-2. Optical image of devices patterned on a MoS$_2$ flake. The flake is the blue part and it is approximately 13 μm long. The gold parts are metal contacts.

CHAPTER 5
Cl AND Ar IMPLANTS INTO NATURAL MoS$_2$

A wide range of doping methods exist for MoS$_2$, but few are ready for industry. Ion implantation is a well-known and common doping method that has largely been avoided in MoS$_2$ due to concerns over the fragility and surface sensitivity of thin 2D films. This chapter encompasses the initial efforts into observing the effect of ion implantation on MoS$_2$. Analyses were performed on the chemical and structural effects of implantation on MoS$_2$, followed by electrical characterizations.

Implants were performed in three manners: into the channel of a pre-made device, into the contact-region during device fabrication, and through the metal contacts of a pre-made device while protecting the channel. Prior to the experiments, little was known about the appropriate implantation parameters, with the three most important being the species, energy, and dose. As is common with ion implantation experiments, two different types of implantation species were employed: an inert species, to observe the effect of damage alone; and a species intended to chemically dope the material, in this case n-doping. The implantation doses were varied over three orders of magnitude to identify effective dose regimes. Low implant energies were employed to ensure implantation into the thin MoS$_2$ film and not the underlying substrate. However, for the through-contact implants, a much higher energy was required to penetrate the metal contact. No activation anneals were performed.

Ion Implantation

Species

Outside of substitutional doping during MoS$_2$ film growth, relatively large and oftentimes complex molecules are typically used as dopants via a surface charge

transfer effect, however these molecules are unavailable for use in ion implantation [41], [40]. For non-molecular MoS$_2$ dopant species that are available with ion implantation, chlorine has been reported to be an effective n-type dopant through an extended MoS$_2$ film soak in a chlorine-containing solution, thus it was chosen as the chemical dopant for these implantations [42]. It was unclear in the report whether the Cl was substituting a S site or whether it was intercalated between the MoS$_2$ layers, but the n-type doping effect was clear. It could be speculated that the high electronegativity of Cl would prevent it from being a donor, however, aside from the reported experimental evidence, models predict that the Cl-Mo bond will in fact result in Cl donating an electron to the Mo d orbitals [94].

Noble gases are typically used for observing the damage effect of implantation due to their chemical inertness, specifically the noble gas nearest in mass to the chosen chemical dopant species to avoid any influence that appreciably different atomic masses and sizes may have on the collision interaction between sample and implanted ion. Thus, argon was chosen as the inert species to observe the damage effect.

Implant Energy

The Stopping and Range of Ions in Matter (SRIM) Monte Carlo software simulation package is a powerful tool for understanding and revealing important parameters of ion implantation experiments. However, SRIM simulations are not optimized for a 2D such as MoS$_2$, where the Van Der Waals gap inherent to layered materials introduces an additional and unaccounted for complexity [95]. SRIM has been shown to over-estimate implant damage for implants into 2D materials, though it has also accurately predicted the projected range [88], [89]. Additionally, secondary ion mass spectroscopy (SIMS) was used to determine the implanted dose profile for the PIII

of phosphorous into MoS_2, albeit for high implant energies and for MoS_2 films thicker than typically used for making device. The SIMS results confirmed the SRIM as reasonable estimates for projected ranges into MoS_2 [54].

Aside for the through-contact implantations, SRIM calculations were performed to aim for a projected range of 9 Å, or approximately the middle to upper region of the second MoS_2 layer to ensure near-surface implantation, keeping the few-layer nature of MoS_2 in mind. This resulted in an implantation energy of 200 eV for Cl, with similar results for Ar. Notably, the straggle, or standard deviation of the projected range, for that implant energy and species is 8 Å, nearly equivalent to the projected range. MoS_2 layers are ~7 Å thick, so these SRIM calculations suggest the bulk of the implanted dose will lay within the first two MoS_2 layers. For the through-contact implantations, with Ni contacts 8 nm thick, a higher energy of 18 keV was used to aim for a projected range near the contact/ MoS_2 interface. Implantations are typically performed at angles slightly off axis from the sample's surface normal, such as 7° off axis, to prevent channeling of the implanted ion which may lead to inaccurate projected ranges [96]. However, the low energy implantations were performed at normal incidence due to the low amount of channeling at would be expected at such low energies.

Dose

When choosing an implantation dose, it's important to consider that the 2H phase MoS_2 employed here has a surface atomic density of ~2.32×10^{15} cm^{-2}. A dose similar to that was chosen for the high end of the dose range. Therefore, the implantation dose matrix was chosen to consist of 1×10^{13}, 1×10^{14}, and 1×10^{15} cm^{-2}. The resulting peak concentrations are approximately 2.5×10^{19}, 2.5×10^{20}, and 2.5×10^{21} cm^{-3}. The concentration profile with depth for the 1×10^{13} cm^{-2} dose is shown in Figure 5-1.

Material Characterization: Methods and Results

To explore the effect of ion implantation on the structure and local chemical environment of MoS_2, XPS and STM/STS were performed on bulk mineralogical samples that were implanted with the noted array of Cl doses, using the low implant energy of 200 eV. The size of the bulk samples (multiple mm in length, width, and thickness) provides multiple benefits over exfoliated flakes (typically nm thick and <dozens of μm^2 in area) when performing these characterization techniques. First, it ensures the samples are larger than the XPS spots size, which is typically $200\mu m^2$, to avoid the XPS spot size overlapping the substrate or any fabricated features and generating unwanted signals; for example, the binding energy of the tantalum 4d core peak can overlap the Mo 3d core peak, so avoiding generation of the tantalum signal, say from TaN alignment marks patterned over a substrate, is critical to attaining sensible results [44]. Second, these characterization methods require the sample to be grounded, either to prevent charge buildup in XPS or to ensure a conductive pathway for tunneling current in STM; this is easily accomplished with large bulk samples, where the reasonably large clamps that hold the sample to the sample holder are often used as electrical grounds, as opposed to small exfoliated flakes which would require additional and unnecessarily complex lithography steps to ensure an electrical ground. Lastly, and perhaps most importantly for the individual running the characterization techniques, bulk material affords a large surface at which to aim. Not every XPS or STM tool is equipped with high magnification cameras for precisely directing the probe. Additionally, STM typically has a relatively small scan window, on the order of 4 μm^2 at the maximum. It would be impractical to try and locate an exfoliated flake on a substrate given these constraints.

XPS Results

XPS characterizations were performed by Xueying Zhao in collaboration with Dr. Scott Perry at the University of Florida. Figure 5-2A shows the Mo 3d and S 2p core peaks for implanted samples as well as for pristine MoS_2. All peaks were aligned to the C 1s peak to avoid any issues of charging. Increasing Cl doses induced core peak shifts to lower binding energies (BEs), as shown in Figure 5-2B, which is indicative of p-type doping of MoS_2 rather than the predicted n-type doping from Cl [97]. The shift in BE is consistent with previous reports of preferential sputtering of sulfur atoms from MoS_2 by Ar^+ bombardment [47], [98]. Reports noted the similar effect that would be expected when depositing Mo on the MoS_2 surface, and concluded that Mo-clusters form during irradiation-induced S-loss. Electrons transfer from the MoS_2 to the Mo to balance the Fermi levels, and an overall p-type shift is detected in XPS. The effect can occur even when Mo-Mo is below the detectable limit in XPS [99], [100], [101]. Relative to the pristine sample, the shift in BE for the 1×10^{13} cm^{-2} dose was nearly negligible, while the shift in the 1×10^{14} cm^{-2} dose was a small but measurable ~0.1 eV. The shift for the 1×10^{15} cm^{-2} dose, however, was much large at ~0.7 eV. In addition, the 1×10^{15} cm^{-2} dosed sample exhibits a MoO_x peak, indicating activation of Mo sites where oxidation can occur following implantation. This finding is notable; while the lack of detected oxidation for the lower dosed samples might be a result of the detection limit for XPS, it also indicates that significant oxidation does not occur for the lower dosed samples.

Angle-resolved XPS (ARXPS) was also performed to observe the presence of implanted Cl as a function of depth within the sample. The implanted species was only detected for the highest dosed sample, which can likely be attributed to the detection limit of XPS (typically within 0.1-1%) being unable to detect the Cl in the two lower

dosed samples, rather than a lack of implanted Cl for the lower doses. As such, all ARXPS results will only refer to the highest dosed sample, 1 x 10^{15} cm^{-2}. The take-off-angle (TOA) is referenced from surface normal, so higher angles provide a more glancing angle and are consequently more surface sensitive, while lower angles probe deeper into the samples. Take off angles were taken from a range of 55 degrees, where ~90% of the signal originates from with a depth of ~2.3 nm into the sample, and 85 degrees, where ~95% of the signal originates from a depth of ~0.45 nm. The chlorine signal held nearly steady with a 2-3 atomic percentage within the depths probed, with the higher end of that range being detected in the more surface levels, within ~1.0 nm of the surface (Figure 5-3). In addition to detecting the presence of Cl, significant amounts of oxygen were also detected in levels increasing from ~25 to ~42 elemental percentage as the probed depth focuses increasingly toward the surface. Regarding the potential sputtering and loss of S that may result from the implantation, the S:Mo ratio remains at a near constant ~1.5:1 throughout the depths probed (Figure 5-4). This indicates a loss of sulfur, however not as great as potentially expected given that the typical S:Mo ratio can be less than the 2:1 expected from stoichiometry due to the presence of S vacancies[102]. Reports of Ar irradiation at 500 eV showed considerable loss of S, ascertained through the S:Mo ratio calculated using the area under the S and Mo XPS peaks[47]. Interestingly, a S:Mo ration of 1.5:1 was only observed for doses exceeding 1 x 10^{16} cm^{-2}, an order of magnitude higher than the dose reported in this chapter. However, the reported 1.5:1 S:Mo ratio was for Ar irradiated samples that where not exposed to air after implantation, and the samples reported in this chapter were. Additionally, the S:Mo ratio in the report was set to 2:1 for the pristine sample and the

inherent S vacancies were not accounted for. Accounting for the native S vacancies would shift their S:Mo ratios to align with lower irradiated doses, closer to those employed in these experiments.

STM/STS Results

STM/STS characterizations were performed by Xueying Zhao in collaboration with Dr. Scott Perry at the University of Florida. To start, STM scans were performed on samples as a function of implantation dose (Figure 5-5). Clearly, the surface becomes increasingly disordered with increasing dose due to damage from the implantation. In fact, atomic resolution of the MoS_2 lattice was not achievable for implanted doses beyond 1×10^{13} cm^{-2}, indicating the high severity of damage and lattice disruption for the higher doses. Surface-averaged STS scans were performed by attaining I-V curves at 16 nearby locations and averaging the results, and an increasingly metallic characteristic, in the form of a reduced bandgap, was observed with increasing dose (Figure 5-6). Additional occupied energy states are created near or within the valence band maximum that result in the bandgap reduction. That result is despite both the high damage and oxidation observed for the higher doses (with the oxidation only observed in the core level XPS peaks for the 1×10^{15} cm^{-2} dosed sample).

The high damage with higher doses precludes those samples from consideration when using STM to observe individual defects produced with implantation. Thus, the 1×10^{13} cm^{-2} dosed sample was used for identifying defects. Four features were observed, shown for a negative sample bias in Figure 5-7A, where the figure's contrast is such that darker regions indicate a higher tunneling current with respect to the brighter spots. The four features are: 1, pristine MoS_2; 2, a dark spot; 3, a dark spot surrounded by a bright halo; and 4, a bright spot. The I-V curves shown in Figure 5-7B

80

indicate enhanced tunneling current for Features 2 and 3, and reduced tunneling current for Feature 4, both with respect to Feature 1, the pristine MoS_2. The change in current is less pronounced for positive biases but is noticeable and reproducible for the negative biases. Since positive biases probe unoccupied states and negative biases probe occupied states, this implies the defects only have significant effect on the occupied states, observable with the affected tunneling current. Thus, Features 2 and 3 represent sites with increased number of occupied states, while Feature 4 represents a site of decreased occupied electronic states.

Ion implantation will not only implant an interstitial defect but will also damage the lattice, thus identifying the observed features requires parsing the two effects. Reports have shown that sulfur vacancies and Ar irradiation-induced damage sites can have enhanced tunneling current, so Feature 2 can be attributed to a surface damage site [103]. The reduced current in Feature 4 could also be due to a subsurface defect, and has been attributed to a missing MoS_2 layer [102]. The final feature, Feature 3, contains elements of both Features 2 and 4, and indicates a charged site that pulls charge from the surrounding region, screens that area, and reduces the current. Similar features have been observed in both irradiated and non-irradiated MoS_2, and were attributed to defects that ionize a site, after which the electronegative S pulls that charge in, and screens the surrounding area. However, they typically see an increased current at positive biases, which was not observed here [104], [105]. Interestingly, other reports have attributed it not to S, but to Mo, and a metallic Mo-cluster that results from multiple local S vacancies [102]. XPS results supported that report, where reduced S was detected in areas where those defects occurred in higher concentrations.

Implanted MoS₂ Devices: Fabrication and Results

Device Fabrication

Naturally occurring MoS_2, purchased from SPI, was mechanically exfoliated onto 300 nm SiO_2 on Si substrates. Flakes of appropriate thickness were identified based on their optical contrast, with few-layer thick flakes (~5-15 layers) being targeted due to their reported higher on currents when compared to mono- or many-layered flakes [68], [9]. All devices were fabricated using a conventional maskless photolithography process flow. While Ti contacts have been shown to produce relatively good contacts to MoS_2, the contacts in this experiment were chosen to be Ni/Au (30/90 nm) due to titanium's tendency to getter the implant species, chlorine [42]. To avoid confusion, nickel was the metal in contact with the MoS_2, while the gold was deposited on top of the nickel.

For the channel-implanted devices (Figure 5-8A), the electrical properties were measured after device fabrication, then the samples were implanted (the metal contacts prevented the contact-area from the implantation), and the electrical properties were measured again. This allowed for a direct before- and after-implantation comparison. For the contact-region implanted devices (Figure 5-8B), implantation was performed after lithographic patterning and photoresist development, but before metal contact deposition. This allowed for the 800 nm of deposited photoresist to protect the channel from implantation. However, it did not allow for a direct before- and after-implantation comparison for a single device, so all comparisons are made for devices with similar channel lengths and flake thicknesses. An example of the process flow for fabrication of the contact-region implanted samples is provided in Figure 5-9. For the through-contact implantations, the implantations were performed after both lithographic patterning and metal deposition (8 nm of Ni), but before metal lift-off. This allowed for both the metal

and photoresist to protect the channel, though, like the contact-region implants, this process flow does not allow for a before-and-after implantation comparison. Following through-contact implantation and prior to lift-off, additional metal was deposited on the samples to ensure the contact thickness was equal to that of the other implanted samples (30/90 nm, Ni/Au). Unless otherwise stated, no anneals were performed on any of the devices. Measurements were performed in air, and no device gating or transfer characteristics were investigated.

Electrical Results

Channel implantations

Output current for pre-devices was observed to decrease after implantation of Cl into the channel. An example is shown in Figure 5-10, where the 1×10^{13} cm^{-2} dose implant yielded a nearly 5x decrease in output current (from 1.9 µA to 0.4 µA), which was a typical result for that dose. The higher doses yielded similar results but in greater magnitude, with the reduction in current exceeding 100x. With such a reduction in current observed after channel implantation, argon was not investigated as a species for channel implantation.

Contact-region implantations

Prior to implantation, devices on few-layer MoS$_2$ flakes typically produced a non-linear I_{DS}-V_{DS} response (Figure 5-11), representative of Schottky behavior at the metal/ MoS$_2$ interface. In contrast, linear I_{DS}-V_{DS} output characteristics were observed following contact-region implantation (Figure 5-11). Comparing devices for the 1×10^{13} cm^{-2} dose implants to an unimplanted device of equivalent channel length ($L_{Channel}$ = 1 µm), the output current increased by 4x for the Cl implantation, from 1.08 µA/µm to 4.32 µA/µm at V_{DS} = 1 V. The 1×10^{13} cm^{-2} Ar dosed sample also yielded an increase in current

over the unimplanted sample, though it was an increase of only 1.8x (1.08 µA/µm to 1.95 µA/µm at V_{DS} = 1 V), less than half that of the Cl implant.

Like the 1 x 10^{13} cm^{-2} dose, the 1 x 10^{14} cm^{-2} Cl dose for the contact-region implantations yielded linear I_{DS}-V_{DS} curves. However, this implant resulted in a decrease in current when compared to both the 1 x 10^{13} cm^{-2} Cl dose (6.75x reduction) and the unimplanted sample (1.5x reduction). The 1 x 10^{14} cm^{-2} Ar doses into the contact-region, however, produced less reliable results. The output characteristics displayed a variety of linear, non-linear, and non-conducting I_{DS}-V_{DS} curves. For a device yielding linear output characteristics, a current of 0.52 µA/µm was observed (V_{DS} = 1 V, channel length = 1 µm), which is close to the 0.64 µA/µm observed for the 1 x 10^{14} cm^{-2} Cl dosed sample. The results are close for dose and species, and conclusion cannot be drawn between their effect.

The 1 x 10^{15} cm^{-2} dosed samples for both Cl and Ar produced highly resistive devices likely due to the damage observed in STM or surface oxidation observed in XPS. The samples were excluded from further analysis.

Through-contact implantations

For all doses, a massive reduction in current was observed for devices after receiving the through-contact implant. For unimplanted MoS$_2$ devices, current are typically in the single digit µA range, within the voltage ranges used. After through-contact implantation of the 1 x 10^{13} cm^{-2} dose, the current dropped nearly two orders of magnitude, into the tens of nA range. A similar result was attained for the 1 x 10^{14} cm^{-2} dose, however the 1 x 10^{15} cm^{-2} dose yielded an additional order of magnitude decrease in device current.

Discussion

The decrease in core peak binding energy observed with increasing dose in the XPS data is typically indicative of p-type doping, in contrast to the expected n-type doping of the Cl dopant [54], [42]. However, no activation was observed in the results so no n-type shift would be expected. Halogens attached to organic chains on the surface of MoS_2 have shown a p-type doping affect, likely pulling charge away due to their high electronegativity [106]. MoS_2 is well known to be naturally n-type, so a compensating p-doping, whether from implant damage or unactivated Cl, would explain the reduction in current observed with the channel implantations. However, if that were true, then a sizable difference between Cl and Ar implants would exist, and that was not observed.

Literature has reported the formation of sulfur vacancies and other defects upon ion bombardment, and models have correlated an increase in density of sulfur vacancies with an increase in current through a metal/MoS_2 interface [103], [102] A p-type shift in XPS peaks was also observed after irradiation of MoS_2 with Ar and was believed to be due to local S-loss that results in Mo-like clusters [47], [100]. STM and STS results here show defects with increased occupied states – more states near or in the valence band. These states are filled by pulling charge from the surrounding area, which would have the p-type effect observed in XPS. This suggests that localized defects induced by implantation create an altered metal/MoS_2 interface that yields a reduction in the Schottky barrier and linearizes the output characteristics.

MoS_2 has anisotropic resistance for current flow, with respect to in-plane (x-y) and out-of-plane (z) flow directions [107]. This implies that damage to the structure (from implants) would have an anisotropic effect: enhancing current from the contact into the MoS_2, while reducing channel mobility for in-plane current flow. The out-of-

85

plane improved the current behavior, observed in the STS tunneling current and contact-region implants. However, the two observations differed on how they trend with dose. This implies that nano-scale results cannot always be extrapolated into micron-scale results in situations like this, where large amounts of induced defects exist, and many are contacted by the micron-scale. Ultimately, for devices, the device-scale is more relevant, and it favored lower implanted doses. The highest dose was clearly destructive, though the difference in lower doses was close. Additional samples are required for drawing a conclusion between the effect of dose and species on contact-region implants.

Summary

200 eV Cl and Ar implantations of MoS_2 were studied. Angle-resolved XPS detected Cl within the first few MoS_2 layers and confirmed implantation. No dopant activation was observed. Results were solely due to implant damage, and that damage increased with implanted dose. The low-dose implant (1×10^{13} cm^{-2}) was optimal for imaging and characterizing individual damage sites with STM. At the higher implanted doses, structural order in the MoS_2 surface was lost.

Implant damage had an anisotropic effect: it degraded in-plane current (x-y) but enhanced out-of-plane current (z). The effect follows from the inherent anisotropic transport properties of layered materials like MoS_2. At the micron-scale, the out-of-plane effect resulted in linear I-V behavior for two-terminal devices, rather than the non-linear behavior common for unimplanted devices. At the atomic-scale, the out-of-plane effect resulted in enhanced tunneling current as damage was increased. Results from devices favored the lower implanted doses, which implies a limit to the practical application of inducing damage in MoS_2. The in-plane effect resulted in higher channel resistance,

and reduced device performance. The detrimental in-plane effect will limit the

application of ion impanation on MoS_2 unless a method can be developed for repairing

the implant damage.
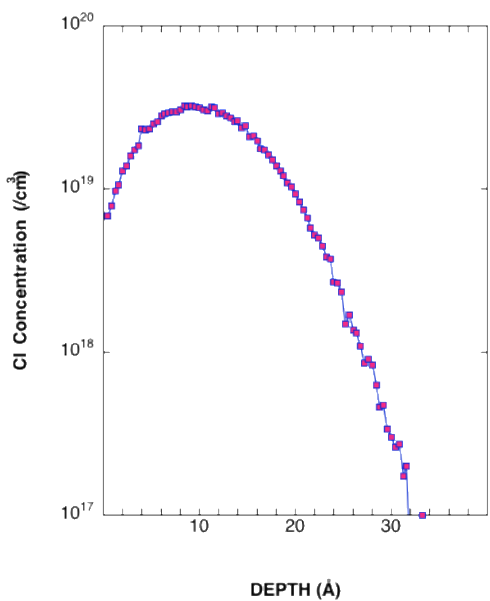
Figure 5-1. Concentration profile for 1 x 10^{13} cm^{-2} dose, 200 eV Cl implant into MoS$_2$.
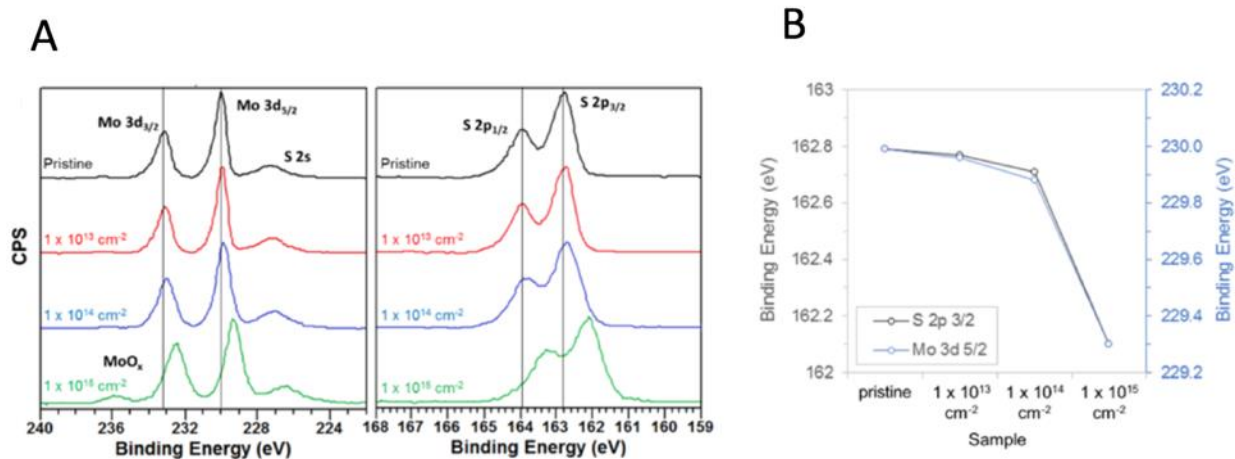
Figure 5-2. XPS analysis of the pristine and implanted bulk MoS$_2$. A) Core electron binding energy peaks. B) Shift in binding energy with dose. Data courtesy of Xueying Zhao.
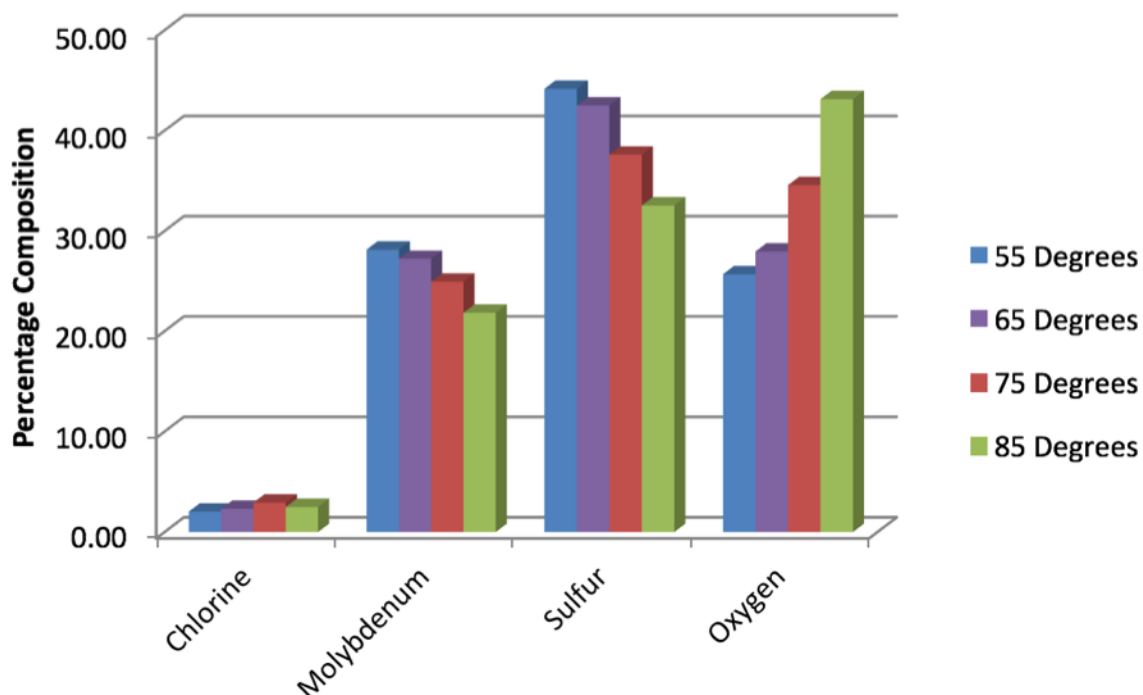
Figure 5-3. Element concentrations at the surface for the 1 x 10^{15} cm^{-2} dose implant. ARXPS data. Data courtesy of Xueying Zhao.
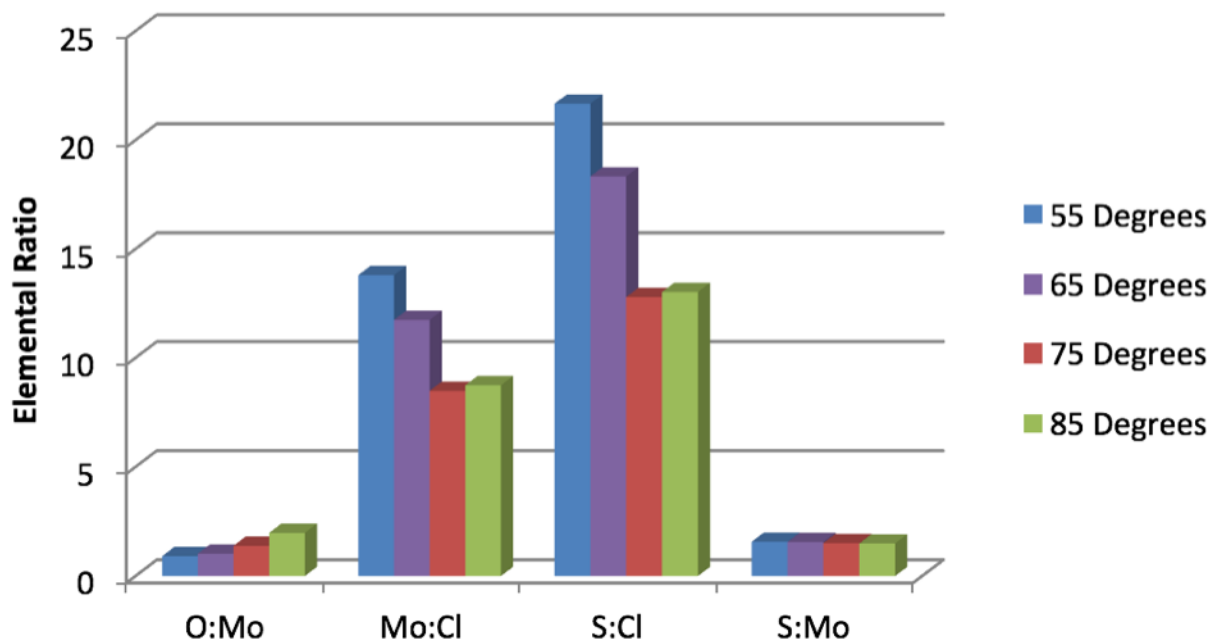
Figure 5-4. Element ratios at the surface for the 1 x 10^{15} cm^{-2} dose implant. ARXPS data. Data courtesy of Xueying Zhao.
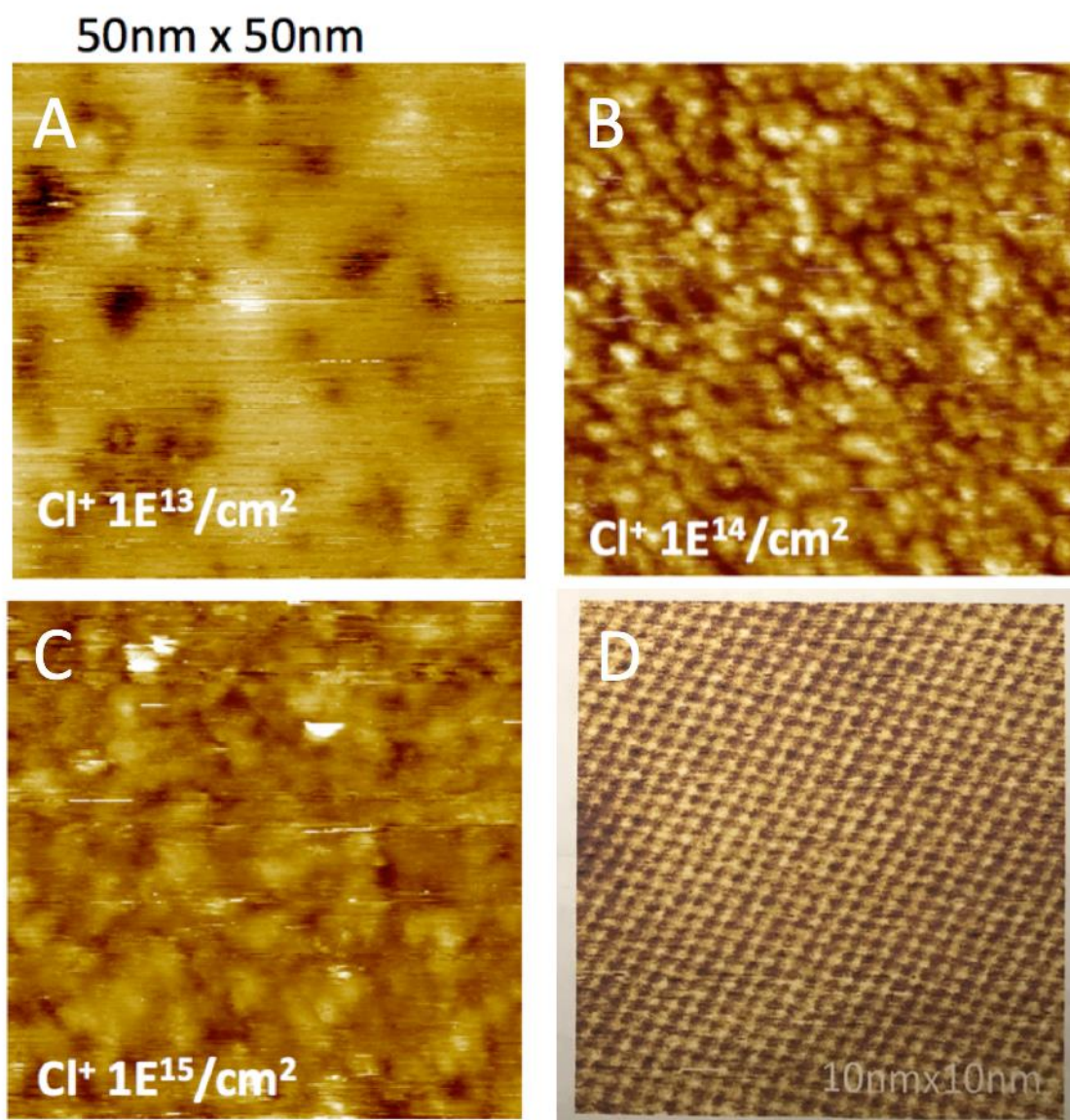
Figure 5-5. STM images for implanted samples. Image window is 50 x 50 nm^2 for A, B, C, and 10 x 10 nm^2 for D. A) 1 x 10^{13} cm^{-2} dose. B) 1 x 10^{14} cm^{-2} dose. C) 1 x 10^{15} cm^{-2} dose. D) Magnified image for the 1 x 10^{13} cm^{-2} dose showing that atomic resolution is still acheivable, though only for that dose. Data courtesy of Xueying Zhao.
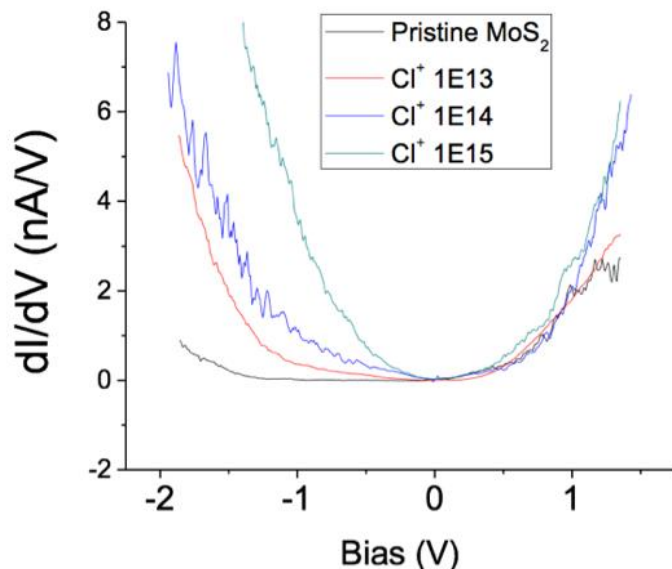
Figure 5-6. Surfaced-averaged STS scans with dose. Visualizes the average density of states across a localized surface. Implantation adds states and results in a reduction in the bandgap. As the dose increased, so did the reduciton in the badngap. Data courtesy of Xueying Zhao.

30nm x 30nm
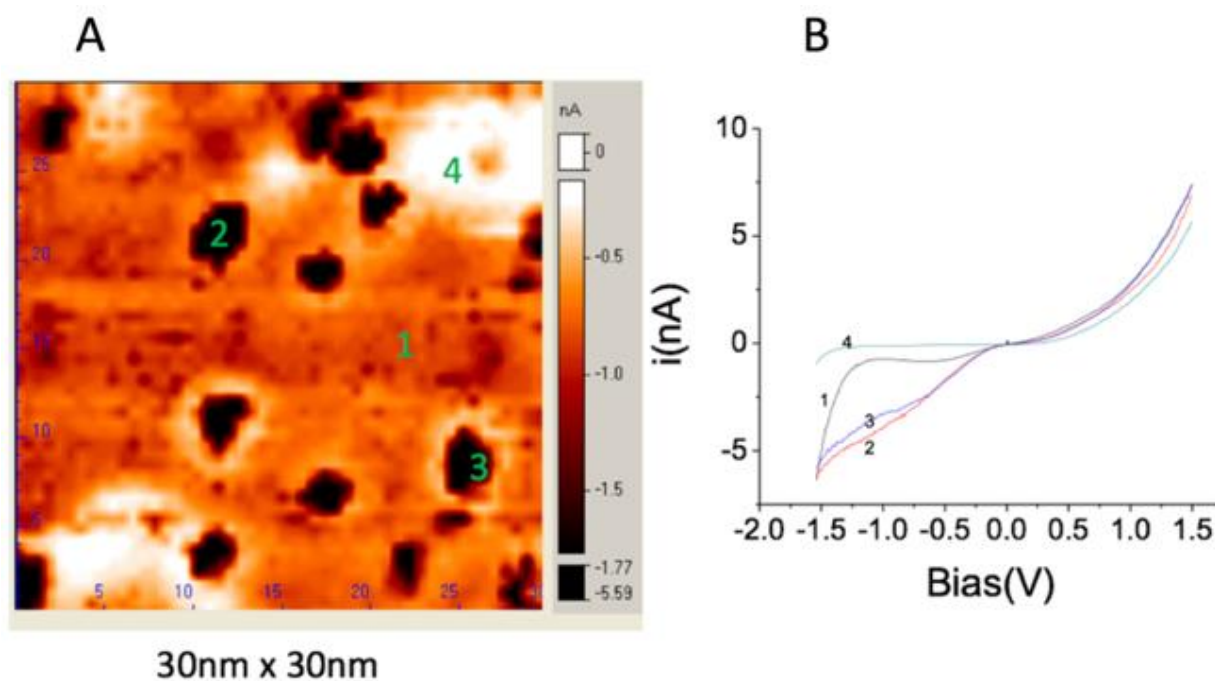
Figure 5-7. CITS performed on the MoS_2 surface after an implantation of Cl at 200 eV, 1×10^{13} cm^{-2}. Displays I-V characeristics at individual surface locations. Point 1 is the undamaged surface, Points 2-4 are defects. Note that the image contrast: a darker colors represents a larger current. Data courtesy of Xueying Zhao.
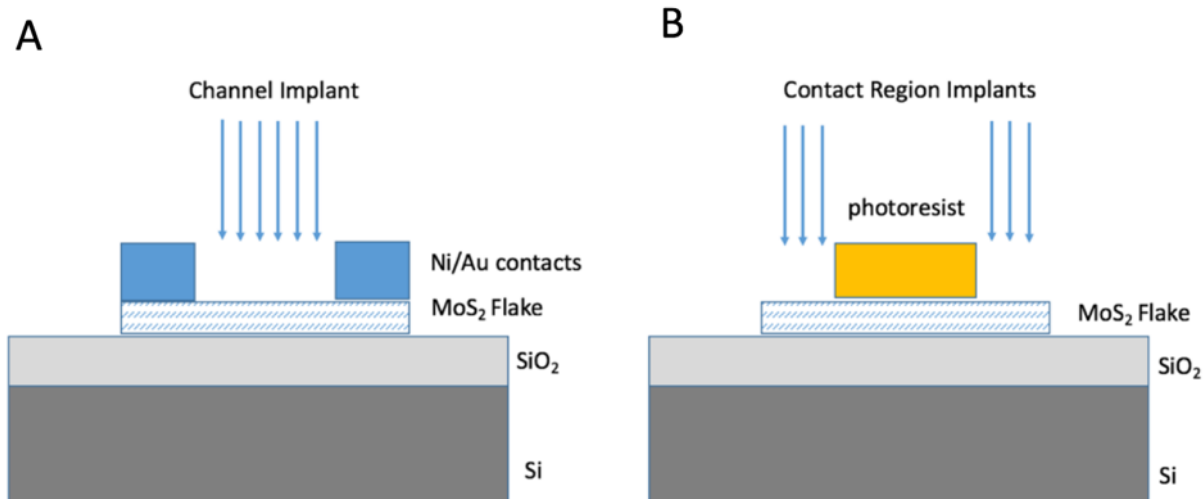
Figure 5-8. A depiction of two of the types of implants performed. A) Channel implants. B) Contact region implants.
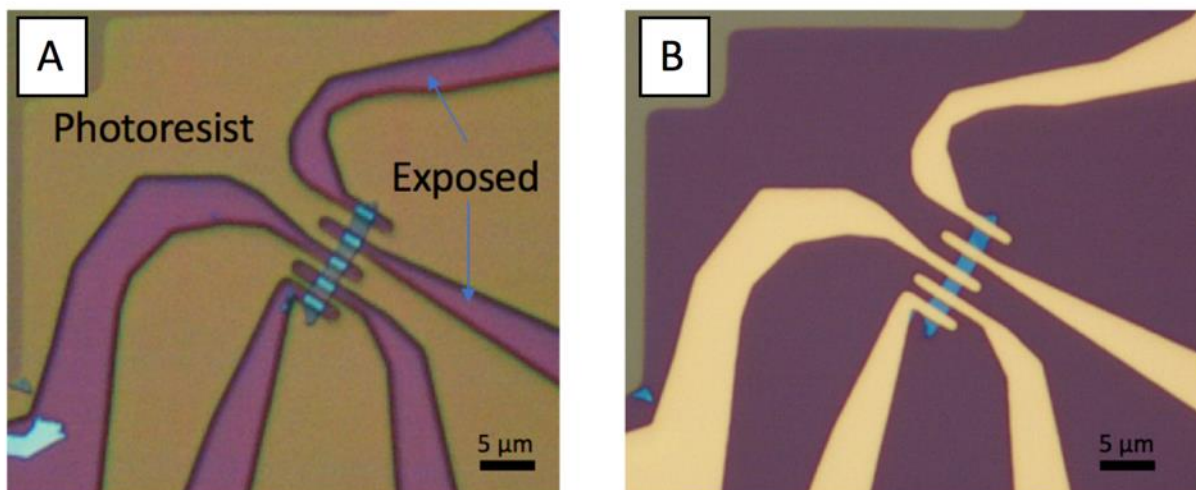
Figure 5-9. Optical microscope images depicting the process flow for contact region implanted samples. A) Photolithographic patterning was used to define the device channels, then implantation was performed, with the photoresist protecting the channel during implantation. B) The device after implantation and completed fabrication. Photos courtesy of author.
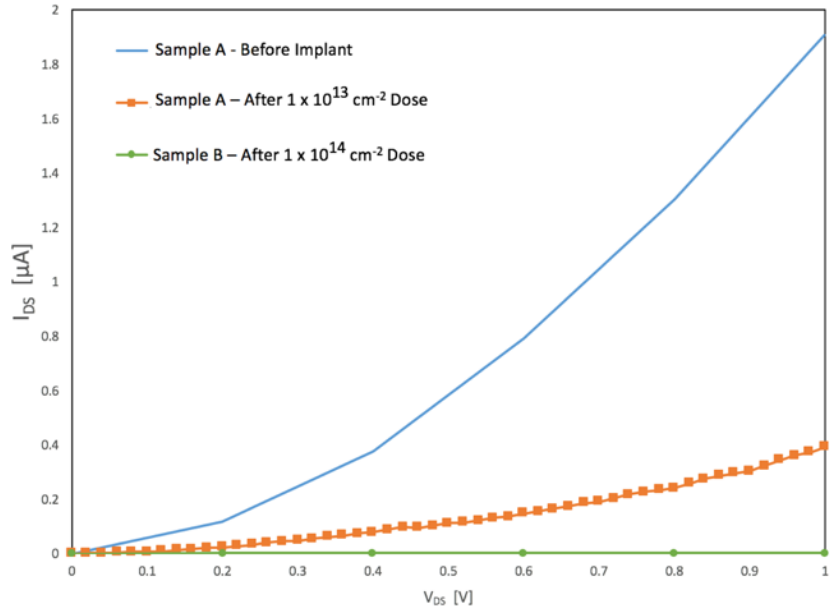
Figure 5-10. Output characteristics before and after implanting the channel with a 1 x 10^{13} cm^{-2} dose of Cl (Sample A), and a typical high-resistance result after implanting the channel with 1 x 10^{14} cm^{-2} dose of Cl (Sample B). A nearly 5x reduction in current is observed after implantation of the channel with a 1 x 10^{13} cm^{-2} dose of Cl (Sample A).
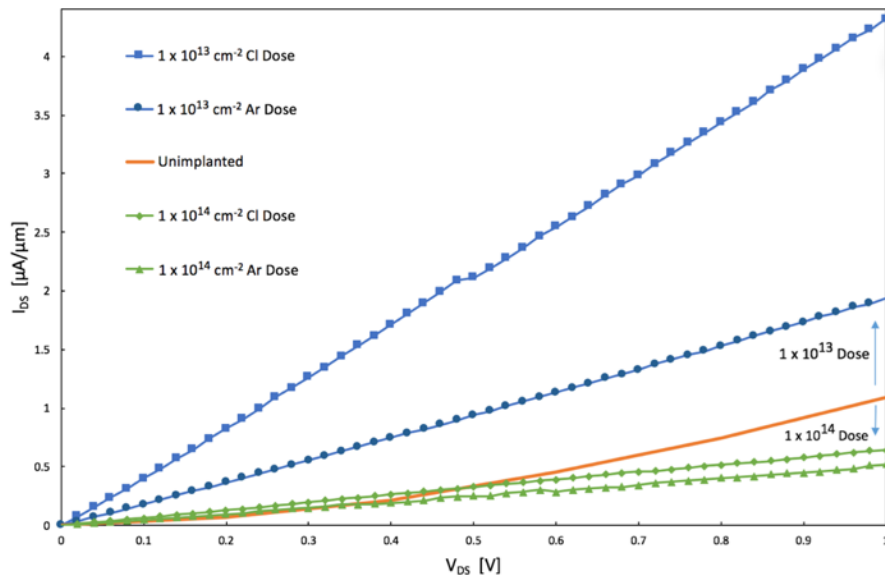
Figure 5-11. Output characteristics for the contact-region implanted samples. Cl and Ar implants. The 1 x 10^{13} cm^{-2} dose increases the current while the 1 x 10^{14} cm^{-2} doses reduces it. Cl implants yield higher currents than Ar implants for both doses.

CHAPTER 6
Cl AND Ar IMPLANTS AND ANNEALS ON GROWN MoS$_2$ FILMS

The previous chapter identified an anisotropic effect of implant damage on MoS$_2$. Device behavior on MoS$_2$ involves both the in-plane and out-of-plane currents, which makes it susceptible to defects that change those responses. Knowledge of that anisotropic behavior can make it a tool to be used, while ignorance of that relationship can leave the properties of the device up to chance. If ion implantation is to progress as a doping method for MoS$_2$, then the anisotropic behavior of the implant damage must be better understood, including how the damage effects the MoS$_2$, how the damage effects a device when it's in the channel, and how the damage effects a device when it's in the contact region. This chapter seeks to better understand those relationships by separating the in-plane and out-of-plane responses, by observing how undamaged, damaged, and annealed material affect those responses, for both the contact-region and the channel. This can be accomplished with proper sample set and analysis. TLM will provide R$_S$ and R$_C$, and insight into the in-plane and out-of-plane response. The sample set includes an unimplanted, unannealed control sample, contact-region implants, implants into the entire film prior to device fabrication, and anneals of the entire-film implants. These samples provide a range of undamaged, damaged, and annealed device areas. Additionally, another major issue is addressed that, if left unresolved, could prevent the widespread adoption of 2D materials: the use of grown films rather than exfoliated mineralogical flakes as the active material in electronic circuits.

Implantations

For the contact region implants, the same implant energy, doses, and species from the previous chapter were used: implant species Cl and Ar, an implant energy of 200 eV, and doses of 1 x 10^{13}, 1 x 10^{14}, and 1 x 10^{15} cm^{-2}. For the samples that received an implantation into the entire film, 200 eV implants were also used but the doses were lowered to 5 x 10^{12} and 1 x 10^{13} cm^{-2} due to the high material damage (Figure 5-5) and reduced device current (Figure 5-10) that was observed with high doses in the previous chapter. Due to limitations in the supply of grown films, only Cl was used for the entire-film implantations; no inert implant species were employed.

Anneals

Post-implantation anneals have dual effect: to repair damage induced by implantation, and to provide the energy for the implanted dopant (which sits interstitially after implantation) to substitute onto the crystal lattice where it becomes "active", or capable of contributing its carrier. Activation annealing temperatures can be quite high, from 800°C to over 1000°C, as they need to provide enough energy and motion for an atom to leave its lattice site so substitution can occur. The growth method for the MoS_2 films employed in this experiment involved a 1000°C anneal in an H_2S atmosphere, hence those conditions were used here [69]. For the film growth process, the 1000°C H_2S anneal is actually a second anneal, with the first being at 800°C for 30 minutes. The 1000°C was found to promote grain growth, observed by a sharpening of spots in electron diffraction patterns, thus it was chosen to help repair any damage, such as sulfur vacancies, that may originate from implantation. The H_2S overpressure may also help minimize oxidation from any residual oxygen remaining in the annealing chamber. Oxidation of MoS_2 can occur at as low as 330°C in air, with decomposition occurring

above 400˚C [108]. Additionally, upon heating above 1300 K, the MoS_2 surface

reconstructs into Mo_2S_3, though XRD results indicate that the bulk of the material

remains $2H-MoS_2$ [109]. The Mo_2S_3 phase is formed by the loss of one S atom per

Mo_2S_4 unit, which results in a higher specific density for the Mo_2S_3, relative to MoS_2,

and contracts the Mo_2S_3 layer. Sulfur loss from within the bulk is thought to be

kinetically limited by the surrounding layers and the contracted layer, causing the bulk to

remain MoS_2. The annealing temperature of 1000˚C is still below that phase-

reconstruction temperature, but only by 26˚C; the H_2S overpressure may help to limit

the surface S loss that encourages the Mo_2S_3 reconstruction.

However, after high temperature H_2S there is typically a yellow sulfur powder

deposited on the chamber walls, which induces a large population of hydrogen that has

freed from the H_2S. The high temperature and free hydrogen could lead to a reaction

with the SiO_2 substrates, forming H_2O that could then oxidize the MoS_2 [110]. Thus, the

annealing time was reduced to 5 minutes, down from the 20 minutes used in the growth

process, to minimize unwanted MoS_2 oxidation or disruption of the SiO_2 substrate.

Contact-region Implantations

Device Fabrication and Implantation

The grown MoS_2 films were first lithographically patterned with TLM arrays, as

described in Chapter 3 and shown in Figure 3-4. Device widths of 150, 200 and 300 µm

were used. The channel lengths varied from 2-25 µm and were measured in an optical

microscope after device fabrication. As in the previous chapter, the samples were

implanted after lithographic pattern exposure and before contact metal deposition and

liftoff; this ensured the channel was protected from the implantation by photoresist. After

implantation, the metal contacts (Ni/Au) were deposited and liftoff was performed. Poor

adhesion was observed between the MoS_2 film and metal contacts, which resulted in the failed fabrication of numerous devices. This necessitated comparison between devices of different widths in order to gather enough data points for TLM. Unfortunately, the poor adhesion issue was so prominent for the Ar 1 x 10^{13} cm^{-2} dosed sample that no useable measurements were achievable and that entire data set was disregarded.

After device fabrication, the samples were capped with 30 nm of Al_2O_3 to improve device performance, to protect the channels from environmental adsorbates, and to prevent oxidation for any anneals attempted after device fabrication.

Electrical Results

Like with the MoS_2 flakes, devices on the grown films yielded slightly non-linear output curves, which is indicative of a barrier for carrier transport at the MoS_2 /Contact interface. Again, like the flakes, contact-region implants induced defects that enhanced the out-of-plane current flow and linearized the output curves (Figure 6-1)

TLM results for the unimplanted films are shown in Figure 6-2. The TLM line-fits possess R^2 values as low as 0.79, which introduces error into the predicted values. The y-intercept, and therefore the R_C, is particularly sensitive to the error. Regression analysis on the line-fit provides the standard error of the estimate. TLM and error analysis are described in Chapter 3. For the control sample, the result is an of R_C of 0.56 ± 2.1 MΩ-µm and R_S of 4.6 ± 0.9 MΩ-µm. The error in R_C is ~4x bigger than the estimated value of R_C, so there is very little certainty on the value of R_C in the result. The error can mask results of the experiment. The estimated value is also 30x bigger than the reported value of 18 kΩ-µm for Ni contacts (the same metal used here) on exfoliated mineralogical flakes with no applied gate bias [111]. The significantly higher Rc on the grown films could be due to several possibilities, including but not limited to

the inherent grain boundaries within the film, residues or contamination leftover from the post-growth film transfer process, degradation of the film after lithographic processing (Figure 6-3), or the poor adhesion between the film and the contact metal.

For the implanted species, the Ar implants will be considered initially to first understand the damage effect (Figure 6-2). The immediate observation is the large increase in measured resistances for the 1×10^{14} cm^{-2} implant, as well as the increased error for the higher measured resistance. The result was a 1.3 - 18x increase in R_C (0.56 ± 2.1 to 9.89 ± 3.5 MΩ-μm). However, for the higher dose of 1×10^{15} cm^{-2}, the measured resistances dropped back down again (0.73 ± 3.5 MΩ-μm), to within error of the control.

For the Cl implants (Figure 6-4), a similar trend as with Ar emerged, where the resistances for the 1×10^{14} cm^{-2} dosed sample are much higher than the control sample, while the higher dose of 1×10^{15} cm^{-2} returned the resistances to near the unimplanted value. This time the 1×10^{15} cm^{-2} dosed sample was joined by the 1×10^{13} cm^{-2} dosed sample, with results within error of the unimplanted sample. The R_C values are displayed in Figure 6-5.

Furthermore, after performing the TLM measurements, the devices were annealed at 350°C for ten minutes in air, with hopes that the Al_2O_3 cap would prevent MoS_2 oxidation. This resulted in a 1-2x increase in current for all implanted samples, but a 1-2x decrease in current for the unimplanted samples (Figure 6-6). While this is an improvement for the implanted samples, the results must be discarded due to post-anneal sample degradations that were observed, which make it impossible to parse those effects from that of the implantation. The degradation is shown in Figure 6-7.

Bubbles appeared in the Al_2O_3 caps, which likely originated from a pressure buildup of remnant hydrogen leftover from the ALD process (H_2O was the oxygen precursor), which was trapped under the cap. This bubbling distorted the cap and likewise the dielectric environment above the MoS_2 device channel, which could have influenced the electrical results. Additionally, a different kind of bubbling also appeared on the Ni/Au contacts, due to well-known interactions between those metals even at low temperatures [112], [113]. Therefore, in future experiments, anneals should be avoided following device fabrication, unless non-reactive contact metals are used, or if the source of oxygen in the ALD process is switched from H_2O to an oxygen plasma, which eliminates H from the process.

Entire-film Implantations

Process

After the films were grown and implanted, some were set aside for H_2S annealing and some were set aside for device fabrication. After annealing, devices were subsequently lithographically fabricated on those samples as well. Ni/Au contacts were used for all devices. After device fabrication, all devices were also capped with 30 nm Al_2O_3. For material characterization, XPS was performed at all stages. Finally, SIMS was performed on the samples to observe the depth profile of the implanted species and to observe any effect of the anneal on that depth profile.

XPS Results

XPS characterizations were performed by Xueying Zhao in collaboration with Dr. Scott Perry at the University of Florida. Figure 6-8 shows the Mo 3d core peak binding energies for the unimplanted sample, and the 5×10^{13} cm^{-2} dosed sample before and after the anneal; this data is representative for the higher dosed sample as well. All XPS

peaks were aligned to the Si 2p peak in SiO_2 of 103.5 eV. As was seen with Cl implants into exfoliated flakes (Figure 5-2), the film implantations experienced a slight (0.1 eV) decrease in binding energy (Figure 6-9). After annealing, the implanted films experienced a BE reduction of 0.35 eV.

Electrical Results

TLM and error analysis are described in Chapter 3. The TLM plots are shown in Figure 6-10, with the resulting R_C and R_S values summarized in Figure 6-11. The annealed samples were not included in the plot. Annealing resulted in a 1.5-3 order of magnitude increase in the resistances. That brings them up from the MΩ-µm range, which was already very high, and into the GΩ-µm range. They will be addressed in the Discussions section.

For the unannealed samples, the unimplanted sample has an R_C of 0.56 ± 2.1 MΩ-µm and an R_S of 4.6 ± 0.9 MΩ-µm MΩ/sq. The 5 x 10^{12} cm^{-2} dose has a 3.2 - 4.6x lower R_S (1.16 ± 0.7 MΩ/sq), but a Rc (4.6 ± 0.9 MΩ-µm) within error of the unimplanted sample. The 1 x 10^{13} cm^{-2} dose increased R_C by 1.44 - 16x (4.0 ± 0.03 MΩ-µm), given the large error of the control, and R_S by nearly 2.2 - 3.1x (12.1 ± 0.08 MΩ/sq).

SIMS Results

SIMS characterizations were performed by Mikhail Klimov at the University of Central Florida. Dynamic SIMS was performed on the implanted films before and after annealing, as shown in Figure 6-12. There is no standard sample for calibrating the concentration of Cl in MoS_2, so only the relative counts from the same species can be compared between samples. The data indicates considerable diffusion of the implanted Cl dopant from the MoS_2 and into the SiO_2 substrate at the high temperature anneals.

Discussion

Devices

In general, the line fits for the TLM data are poor, with R^2 values sometimes in the 0.70-0.9 range. There is a significant amount of variation, and the standard error is often larger than the predicted value. This places most results within error of the unimplanted sample. It's unclear if the variation is inherent to the grown material, to MoS_2 itself, or as a result of the processing. In addition to any possible variation in the material, TLM assumes equal doping across the entire semiconductor, so the doping in the channel- and contact-regions should ideally be equal. When implanting into the contact-region only, the intent is to dope that specific location, which may introduce error into the TLM line fits for the contact-region implants. However, large variability and poor TLM line fits were also observed for the entire-film implants, where doping should be equal in the channel and under the contact.

The group who grew the films performed experiments to observe the effect that different top and bottom dielectrics would have on the transport properties of devices made on their films. Changing the dielectric environment surrounding a device would be expected to screen charges differently, which would have an impact on the mobility of carriers flowing through the channel [114]. However, the resulting mobility values were all within the margin of error, regardless of the dielectric. The result was attributed to a variety of different scattering mechanisms inherent to defects in the film, which overpowered the impact of the dielectric [115]. That report supports the argument that the variability in our TLM data arises from the material itself.

For the contact-region implants, the 1×10^{14} cm^{-2} dose clearly yields higher resistances for both Cl and Ar implantations. However, both the lower and higher doses

produce resistances that are within the error of the unimplanted sample, meaning any experimental effect on them cannot be detected. There have been reports showing drastic changes in MoS_2 based only on irradiated dose. The MoS_2 changed from semiconducting, to insulating, to metallic, and to insulating again as the dose increased and the damage evolved. However, this was for helium implants at much higher energies (30 keV) and much higher doses ($1 \times 10^{14} - 1 \times 10^{18}$ cm^{-2}) than were employed in these experiments [116]. It's unclear why the resistances for the mid-dose implant are so high.

The contact-region implants linearized the I-V behavior, which is a positive result for the defect-riddled films. It shows that, despite the high concentration of native defects, the defects induced by the implant behave like they do on natural MoS_2. The defects are not consumed by other defects, and their effect is not drowned out. Thus, it's still possible to have a degree of control over the film's properties, despite the dominance of the native defects. However, effects from the linearized I-V behavior did not translate into a measurable change in R_C or R_S, for the low- and high-dosed implants. So, the contact-region implants had an effect in one area, but not in another. The result could be from the variation in the films, though it could also imply that contact-region implants are not capable of showing the full effect of an implant, or any general doping method. If so, they are of limited use for doping experiments, other than for showing linearization of I-V behavior occurred.

Implants into the entire film show a more consistent trend. The lower dosed sample has a lower R_S than the control, even when accounting for error. However, R_C is within the error. The higher dose shows a clear increase in resistances over the

unimplanted and the lower-dosed sample. The increase in R_S from the control to the

higher dosed sample is nearly equal to the reduction in R_S from the control to the lower

dosed sample. It's difficult to discount the results of the lower dose without also

discounting the results from the higher dosed sample. Given the harmful result from the

in-plane effect of implant damage that was observed in the previous chapter, it's difficult

to believe that an implant would reduce the R_S, though it may suggest a damage

transition where the in-plane effect of damage is beneficial. A larger population size is

required to make a conclusion. Regardless of that possible beneficial transition in

implanted dose and induced damage, the results show that the damage induced

between the two implanted doses is the transition where harmful damage occurs to the

in-plane and out-of-plane properties of MoS_2.

Comparing the 1×10^{13} cm^{-2} dosed samples of the two implants, the contact-

region implant shows little effect, while the entire-film implant shows a strong effect. If

anything, they would be expected to have similar R_C values, since the contact-region

was implanted in both cases. If the result is not due to random variation, then it implies

that the increased resistance of the channel (in entire-film implant) is also felt in the R_C

approximations. The opposite can occur, doping the channel can give a perceived

reduction in R_C by reducing the barrier at the channel/contact-region interface [39]. The

effect is possible then, that the contact region was similarly damaged in both cases, but

the higher resistance in the channel for the entire film implant leads to a "false" increase

in R_C.

Anneals

. The SIMS data indicates that the dopant is effectively absent from the film after

the anneal, yet the anneal induces orders of magnitude increases in the resistances,

even for the unimplanted sample. The films are grown at the temperature, so theoretically the anneal should not damage them. The XPS data shows a modest p-type shift of in binding energy of 0.35 eV, indicative of p-type doping.

The issue lies in the substrate. The films are grown on Al_2O_3 and transferred to SiO_2, the SiO_2 never sees the anneals. When designing the anneals for these experiments, concerns were raised over free hydrogen from the H_2S reacting with the SiO_2 and eventually oxidizing the MoS_2. This led to a reduction of H_2S annealing time from 20 minutes (the growth time) to 5 minutes. Initial fears of MoS_2 oxidation were put to rest when the post-annealed Mo 3d core peak showed no oxidation in XPS. However, looking at the XPS data again indicates that there was indeed a reaction, but not with Mo. The O 1s peak (Figure 6-13) and the Si 2p peak (Figure 6-14) both show strong enhancements in intensity, only after the H_2S anneal. Whereas other peaks, like the Mo 3d peak in Figure 6-15, did not show such enhancements after the H_2S anneal. It's unclear the exact reaction or reactions that occurred but both the XPS data and electrical results cannot be trusted after annealing at 1000°C for 5 minutes in H_2S.

Summary

The experiment studied the effects of implant damage and repair on the electrical properties of grown MoS_2 films. A post-implantation anneal was performed for damage repair. The films contained a high concentration of native defects due to their growth process, which resulted in highly resistive and highly variable material. The variability added significant error into the results and made precise effect of the experiments unclear. Despite the native defects, the defects induced from contact-region implants behaved like they did in natural MoS_2: by enhancing out-of-plane current and linearizing device I-V behavior. However, the enhanced out-of-plane current did not translate into

an improved R_C. For the implants performed into the whole film, the implant damage was not significant enough to impair the in-plane and out-of-plane electrical properties until the implanted dose reached 1×10^{13} cm^{-2}, at which point R_C and R_s increased. Attempts to repair that damage revealed that the chosen annealing temperature (1000˚C) was too high: the implanted species diffused out of the sample and a SiO_2/H_2O reaction degraded the film. The prospect of damage repair and dopant activation in MoS_2 remained undetermined.
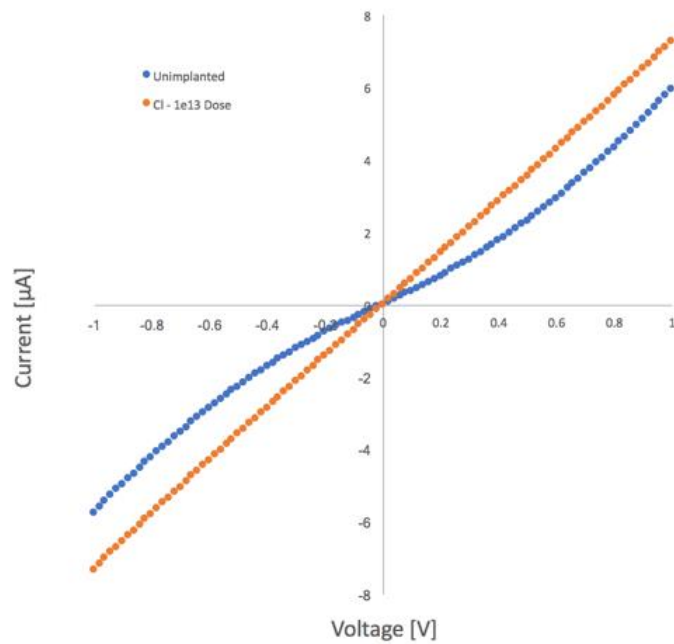
Figure 6-1. Output curves before and after a contact-region Cl implant of 1 x 10^{13} cm^{-2}. Nonlinear I-V response typically observed before implantation. Linear I-V response observed after contact-region implants.
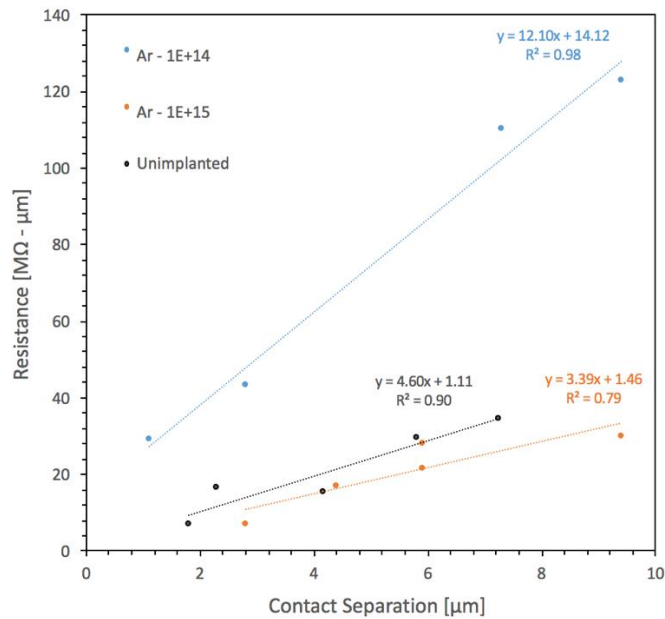
Figure 6-2. TLM data for unimplanted film and Ar implants, with 1x10^{14} and 1x10^{15} cm^{-2} dose.
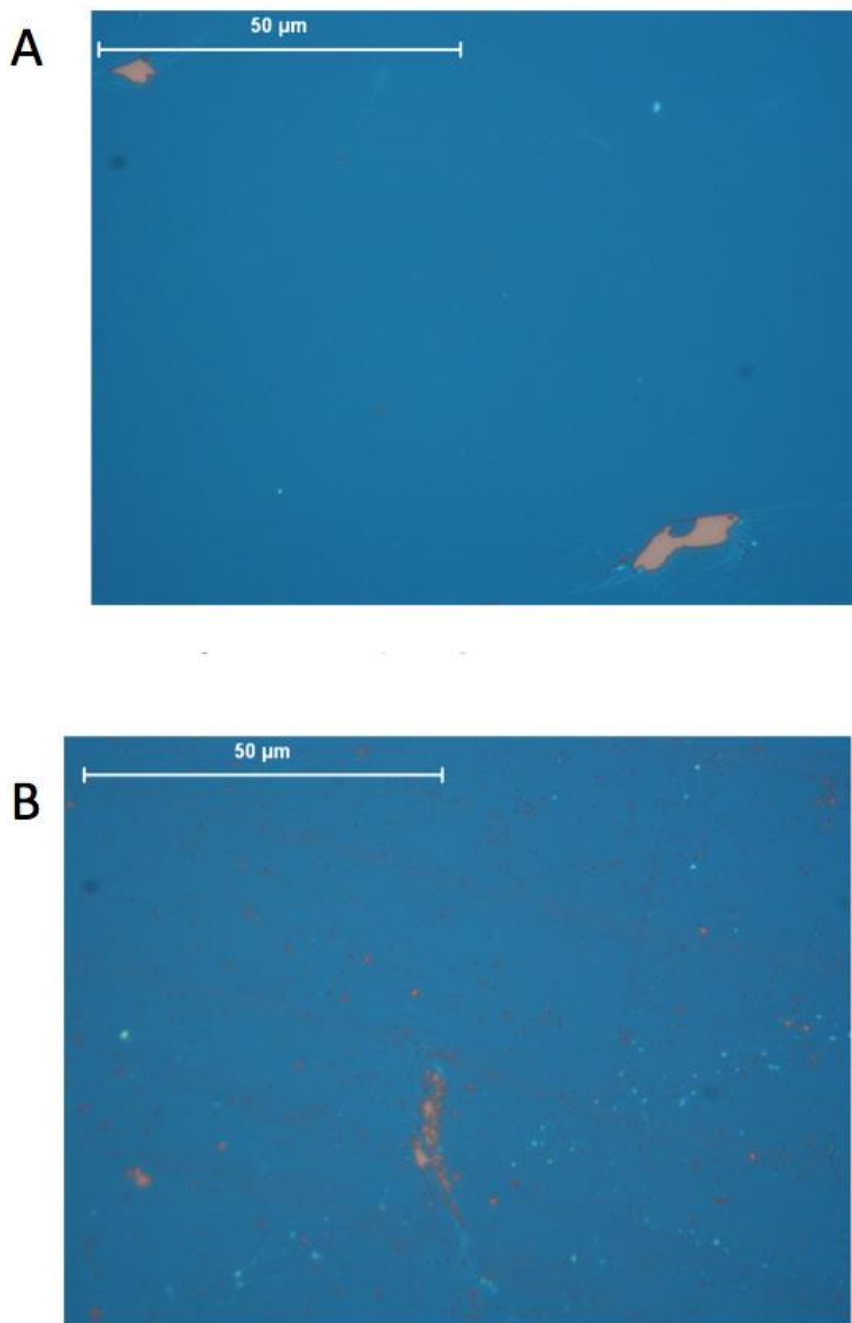
Figure 6-3. Optical image of grown MoS$_2$ film showing film degradation after processing. A) Before processing. B) After processing. Photos courtesy of author.
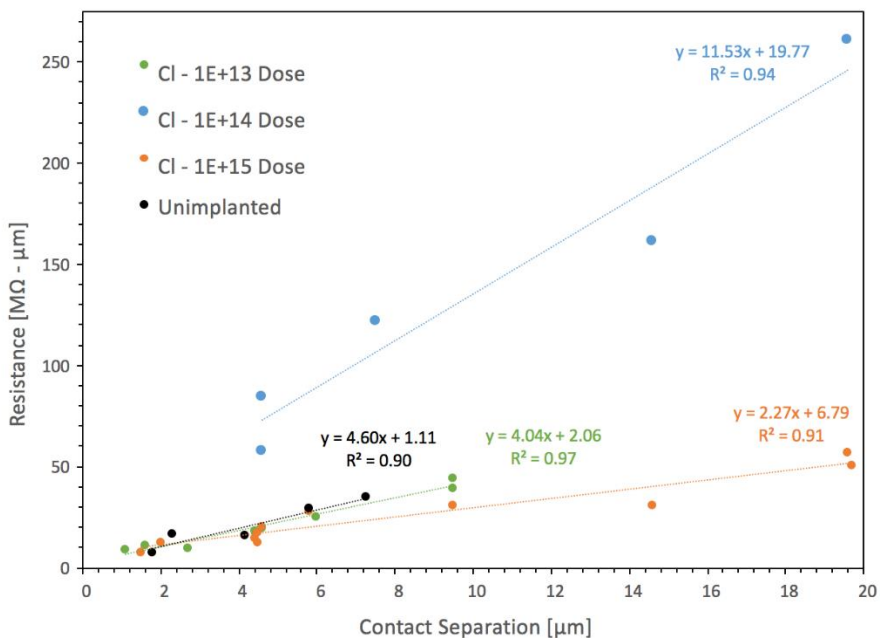
Figure 6-4. TLM data for unimplanted film and Cl implants, with 1×10^{13}, 1×10^{14}, and 1×10^{15} cm^{-2} dose.
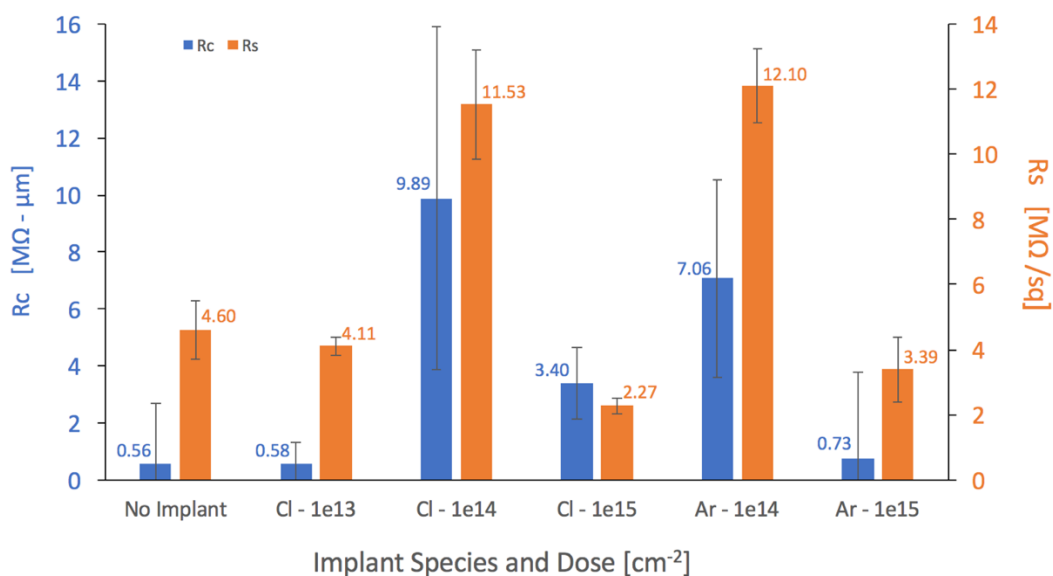
Figure 6-5. R_C and R_S data for implanted grown MoS$_2$ films. The error bars represent the accuracy of the TLM line-fits in Figures 6-2 and 6-4, and the standard error of the estimate for that fit.
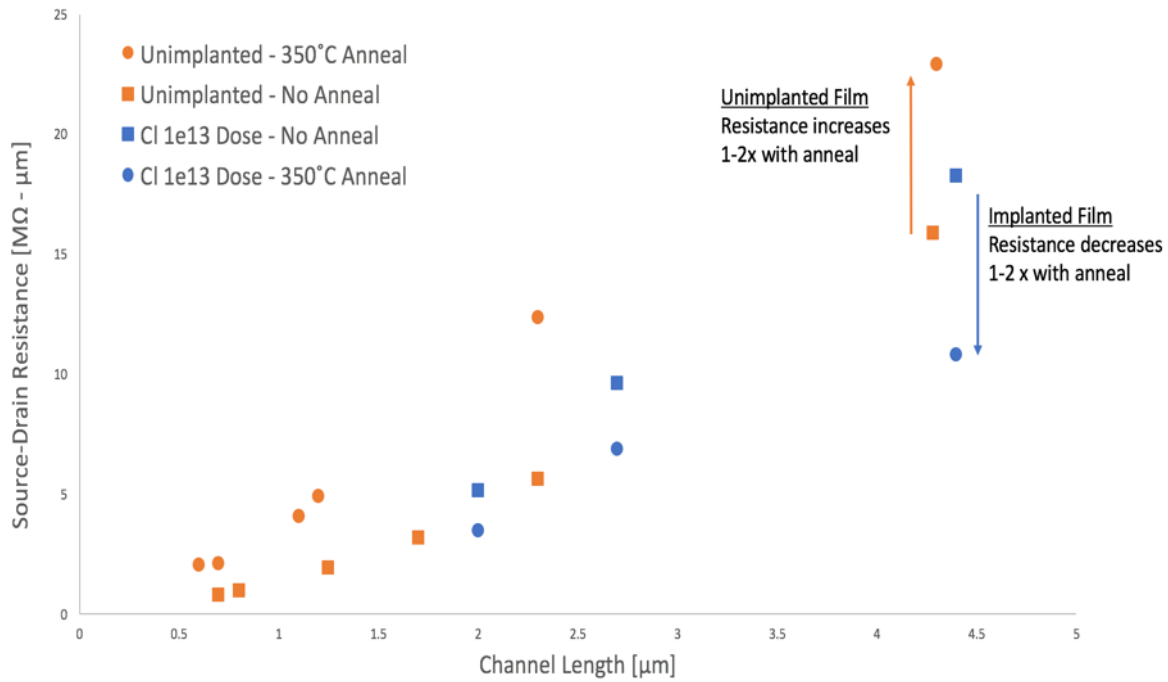
Figure 6-6. Impact on the total resistance of devices after annealing for 350˚C for 15 minutes. The anneals were performed after the devices were fabricated.

Figure 6-7. Degradation of devices and Al_2O_3 cap following 15 minute, 350˚C anneal. The anneals were performed after the devices were fabricated. Photo courtesy of author.
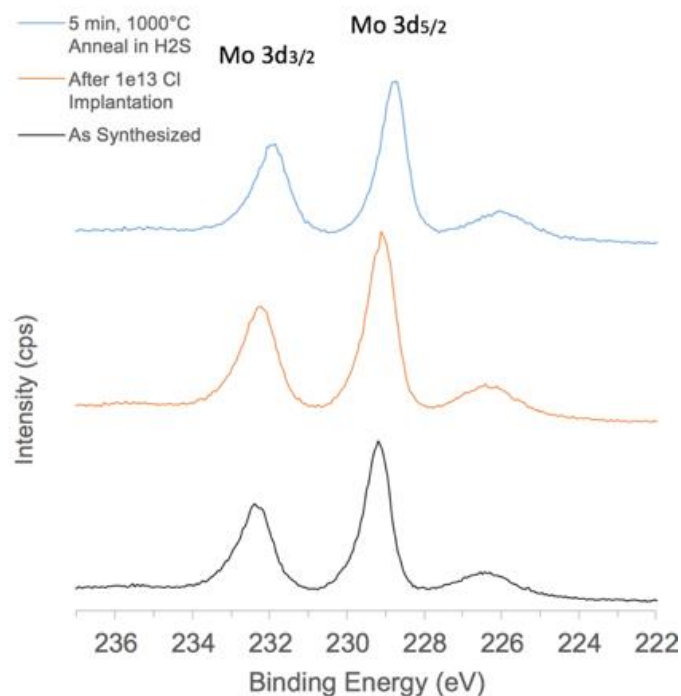
Figure 6-8. Mo 3d core electron binding energy peaks for the Cl, 5 x 10^{12} cm^{-2} dosed
          sample, before and after annealing. Data is representative of the 1 x 10^{13} cm^{-2}
          dosed sample as well. Data courtesy of Xueying Zhao.
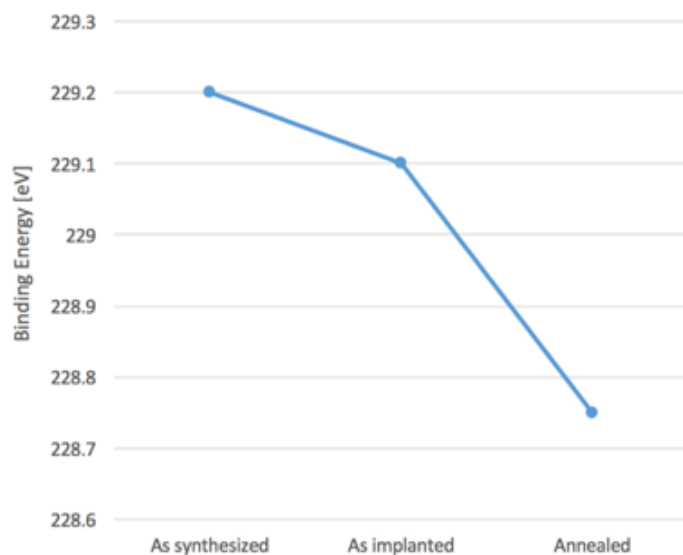
Figure 6-9. Mo 3d$_{5/2}$ binding energy shift after implant and anneal for both Cl
          implantations doses, and for an unimplanted grown MoS$_2$ film. Data courtesy
          of Xueying Zhao.
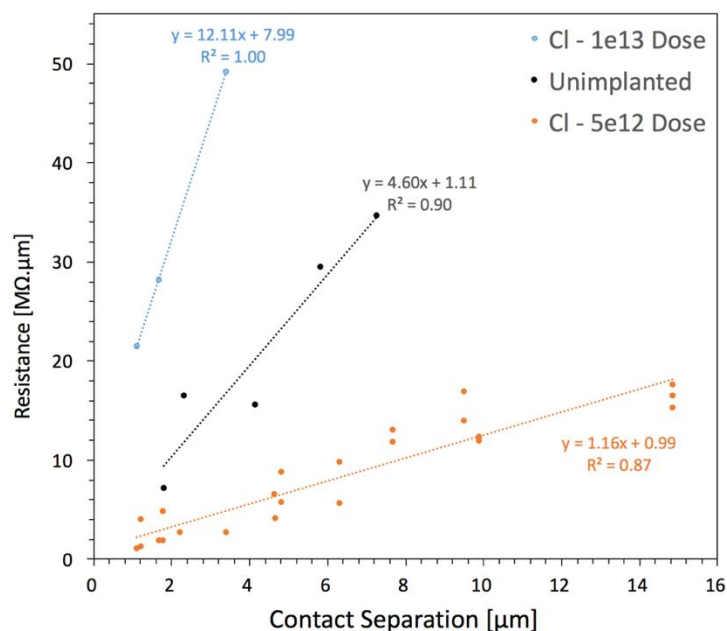
Figure 6-10. TLM data for films implanted with Cl at doses of 5 x 10^{12} cm^{-2} and 1 x 10^{13} cm^{-2}, before and after annealing in H_2S at 1000˚C for 5 minutes.
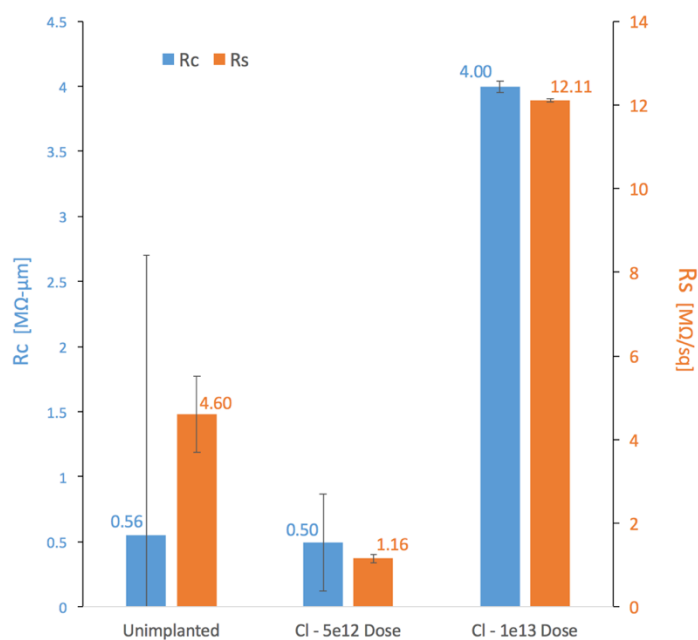
Figure 6-11. Sheet and contact resistance values extracted from TLM, before annealing in H_2S at 1000˚C for 5 minutes. The error bars represent the accuracy of the TLM line-fit in Figure 6-10, and the standard error of the estimate for that fit.
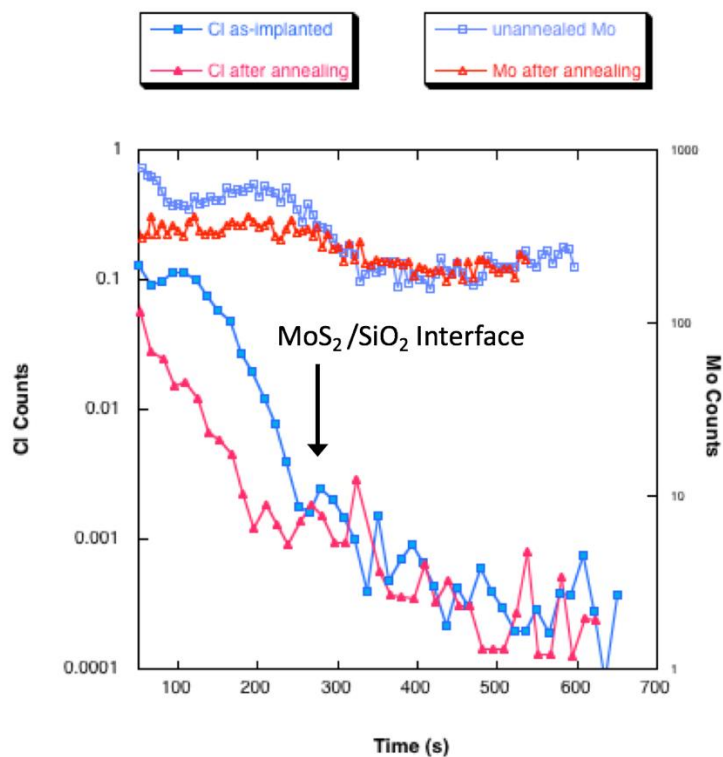
Figure 6-12. SIMS data tracking cocnetration of Cl and Mo with depth. For a grown MoS$_2$ film implanted with a 1 x 10^{13} cm^{-2} dose of Cl, before and after a 5 minute H$_2$S anneal at 1000˚C. Cl has diffused from the MoS$_2$ into the substrate following the anneal. Data courtesy of Mikhail Klimov.
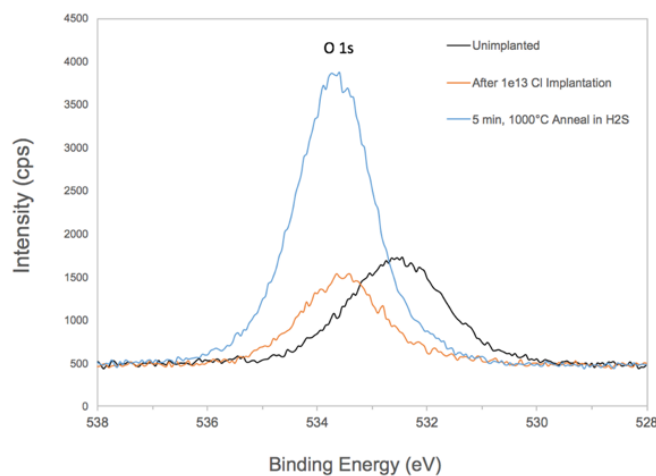
Figure 6-13. XPS spectra for O 1s binding energy. Oxygen peak intensity drastically increases following H$_2$S, 1000˚C, 5 minutes anneal. Data courtesy of Xueying Zhao.
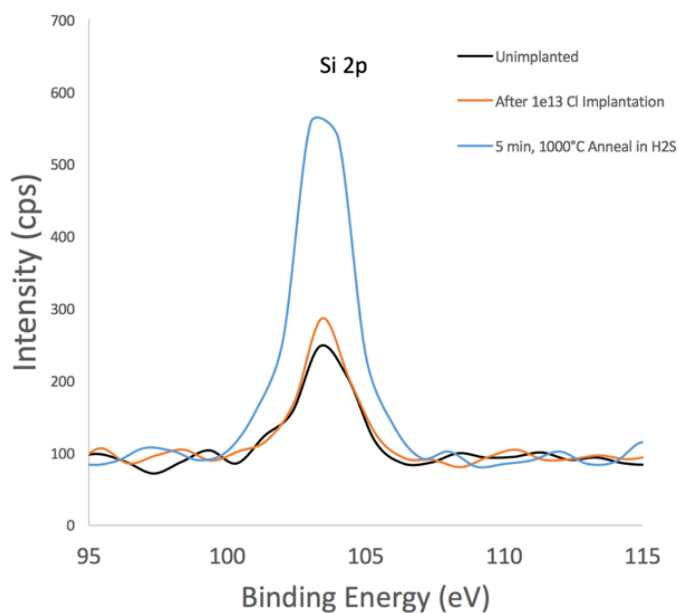
Figure 6-14. XPS spectra for S1 2p binding energy. Si peak intensity increases significantly following H_2S, 1000˚C, 5 minutes anneal. Data courtesy of Xueying Zhao.
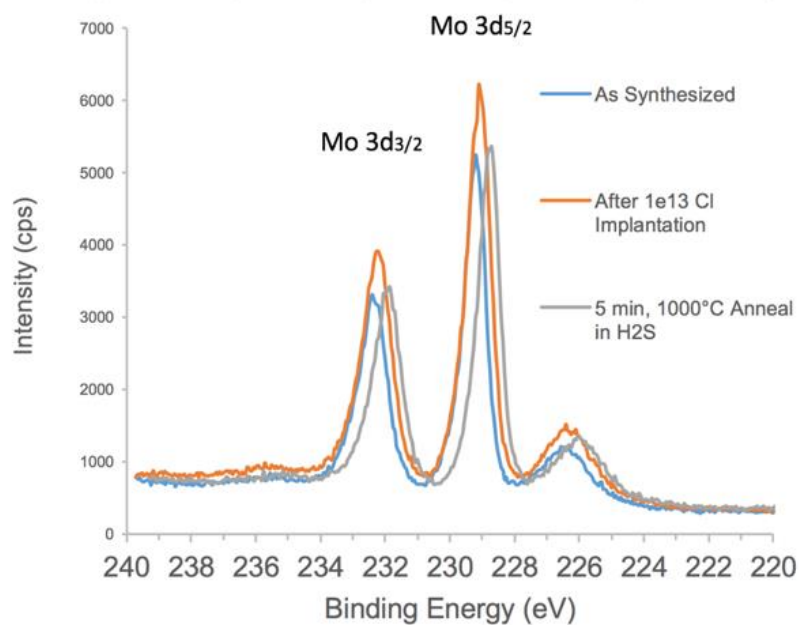
Figure 6-15. XPS spectra for Mo 3d binding energies. Mo signal dose not increase following H_2S, 1000˚C, 5 minutes anneal, unlike for Si and O signals. Data courtesy of Xueying Zhao.

CHAPTER 7
P, As, Ar, Kr IMPLANTS AND ANNEALS OF GROWN MoS_2 FILMS

The previous chapter left multiple questions unanswered. Specifically, appropriate dopant species for implantation were not identified, and post-implantation activation anneals were yet to be refined. The works in this chapter address those issues, with one noteworthy difference from the previous chapter: the switch from a n-type to a p-type dopant species. Additionally, only entire film implantations were performed. A focus was placed on post-implantation anneals, which were performed in a H_2S atmosphere over a broad temperature range. Raman and PL spectra were gathered throughout the process to observe MoS_2's physical response to the damaging and healing processes. Additionally, transfer characteristics of MoS_2 devices were measured and analyzed.

Implantations and Anneals

The full experimental matrix is shown in Figure 7-1. The supply of grown MoS_2 films was limited, thus the full experimental parameters were not applied to every implanted species. Additionally, sample 7 in Figure 7-1 was lost during processing, but it remains in the sample matrix to show the full breadth of the intended experiment.

Implant Energy and Dose

The implantation energy was kept consistent with that of the previous chapters, 200 eV. Based on the high damage observed for the high dose channel implants into MoS_2 flakes (Figure 5-5), the doses employed in this chapter were kept to a narrower range of 1 x 10^{13}, 5 x 10^{13}, and 1 x 10^{14} cm^{-2}.

Dopant Selection

MoS$_2$ is intrinsically n-type, but the CMOS technology requires both n-type and p-type transistors, and p-n junctions are important building blocks for numerous devices. Numerous potential solutions to this include using separate gates to electrostatically induce n- and p-type regions, using exotic device designs such electric double layer transistors, using two different TMDCs with different intrinsic doping types, or by selectively doping the MoS$_2$ [117], [118], [119]. It's worthwhile to explore all avenues, thus, a method for producing p-type or even ambipolar MoS$_2$ is a relevant pursuit.

Plasma immersion ion implantation (PIII) experiments have successfully p-doped MoS$_2$, in the form of ambipolar behavior, by using phosphorous as the dopant species [54]. In the studies, a bias was applied to MoS$_2$ during exposure to a phosphine plasma. The bias attracts ionized species and promotes implantation [120]. Three sample biases were used: 0 V, 1kV, and 2kV. Notably, only the 0 V PIII phosphorous exposure produced ambipolar behavior in MoS$_2$, while the higher sample biases and doses yielded devices that could not be modulated by an applied gate bias. Exposing MoS$_2$ to a plasma (SF$_6$, CHF$_3$, CF$_4$, O$_2$) with no applied sample bias was reported to have a significant effect in the form of p-doping or film etching, depending on the plasma species and exposure dose [121], [122]. The PIII report also observed film etching, approximately 3-4 nm for the highest energy (2 kV) exposure, though no value was reported for the other sample biases.

. The PIII exposure conditions were reported as a function of simultaneous increases in both implant energy and dose, so it's impossible to separate the effect of each and determine whether it's the implant energy or dose that inhibits modulation. This is an important considerations because high implantation doses (>1 x 10^{13} cm^{-2})

into MoS$_2$ have been correlated with surface damage and degradation of device output characteristics [123].

Models have predicted P to be favorable in two criteria that are critical for effective dopants: a low ionization energy and an energetic preference for moving to the optimal lattice site. That is, the ionization energy for a dopant should be within a few kT (also known as the thermal energy, ~26 meV at room temperature) of the nearest energy band or the dopant will not effectively contribute carriers at room temperature. Phosphorous in MoS$_2$ has been predicted to have an ionization energy of ~100 eV, or just under 4kT [94]. Additionally, a dopant can have different doping effects depending on its location in the lattice, for example whether it's substitutional or adsorbed on the 2D MoS$_2$ surface. It's important that the formation energy for dopant substitution vs. adsorption favors the site where the intended doping will occur. Indeed that is the case for P, as models predict a more favorable formation energy for substitution onto S sites rather than for surface adsorption [94]. This contrasts with Cl, where the formation energies for adsorption and substitution are less disparate, implying less of an energetic drive for the intended substitution. However, substitution for Cl was still favored over adsorption, though in this sense the models suggest that P may be a more effective dopant than Cl.

The successful p doping with phosphorous in PIII and the predicted efficacy of P as a dopant provide solid motivation for choosing P as the dopant for the following ion implantation experiments. Likewise, argon is the corresponding dopant for observing the damage effect. In addition to these species, models also predict arsenic to produce electronic states even closer to the valence band than phosphorous, hence As could be

116

a more effective p-type dopant than P [124]. The corresponding noble gas for exploring

the damage effect relative to As is krypton. Thus, As and Kr were utilized in addition to

P and Ar.

Anneals

The results from the previous chapter indicated that 1000°C was too high for

post-implantation anneals in H_2S due to two reasons: diffusion of the dopant (Cl) from

the MoS_2 and into the substrate (Figure 6-12), and a reaction between H_2S and the

oxide that negatively affected the films. However, activation typically requires high

temperatures; there may exist only a small window between dopant activation and

dopant out-diffusion with MoS_2. Again looking at the success of the phosphorous PIII

report for guidance, they utilized a low temperature post-exposure anneal of 300°C for

15 minutes in a nitrogen ambient [54]. The report claimed activation of P based on the

XPS P $2p_{3/2}$ core peak binding energy (BE) of 133.4 eV closely matching that of P in

MoP. However, this appears to be a dubious claim. Both their reference and their

reference's reference specifically do not attribute the P peak near 133.4 to P in MoP,

rather they clearly attribute it to phosphorous oxides, such as PO_4^{3-} or P_2O_5. The P peak

arising from MoP is ascribed to a peak doublet that occurs at 130.1 and 129.2 eV,

neither of which were reported after PIII [125], [126]. So, the P peak observed after PIII

appears to be from a phosphorous oxide and not come from an interaction with Mo,

however that does not preclude P substitution. The PIII report does not indicate which

dose they used for detecting P in XPS. With Cl implants into flakes, Cl was only

detected in XPS for high doses that also caused significant lattice damage that

promoted Mo oxidation [123]. It's possible that the PIII report also utilized a high dose in

order to detect the P in XPS, which could have caused extensive damage and

117

oxidation. That oxidation may have been avoided for the lower energy, lower dosed samples, which were the exact samples that yielded the ambipolar MoS_2 behavior.

Regardless of the issues with the PIII XPS data, the 300°C anneal did have a benefit after PIII. Raman spectra indicated a considerable increase in the FWHM of both MoS_2 Raman peaks after PIII, which is indicative of lattice damage. Annealing returned the FWHM to nearly their pre-exposure values. Thus, with or without dopant activation, the anneal repaired much of the implantation damage.

With that knowledge, and remembering that 1000°C anneals lead to out-diffusion of the implanted species, 15 minute anneals at temperatures of 300°C and 800°C were chosen for these experiments. Additionally, H_2S was again chosen for the annealing ambient in an attempt to further repair implantation damage and prevent any sulfur loss that might occur at elevated temperatures [127].

Device Fabrication and Results

To start, grown films were implanted and annealed. Following that, devices were patterned on the films using standard photolithography processes with Ni/Pd contact stacks. The devices had widths varying from 80 μm to 300 μm. The channel length was 8 μm. First examining the damage effect of Argon implantations in Figure 7-2, the low dose of 1×10^{13} cm^{-2} reduced the device's on-state current by approximately 2.5 orders of magnitude. A respectable I_{ON}/I_{OFF} ratio of nearly 5 orders of magnitude was maintained. However, increasing the implantation dose to 1×10^{14} cm^{-2} resulted in a loss of device modulation. Moving on to P implants, it would be expected that P follows Ar with respect to dose, and indeed that is the case, as shown in Figure 7-3. A dose of 1×10^{13} cm^{-2} reduces the on current by multiple orders of magnitude while larger doses inhibit device modulation. In the case of P, the on current for the 1×10^{13} cm^{-2} dosed

sample is reduced by four orders of magnitude, compared to the two orders of magnitude from Ar implants, and the I_{ON}/I_{OFF} ratio is reduced from five to three after implantation.

Figure 7-4 shows that with each successive anneal, from 300˚C to 800˚C, the on current is increased by approximately one order of magnitude. Mobility values were extracted from the transfer curves of multiple devices using Equation 3-1, and were averaged around a point on the transfer curve to account for error in the I_{DS}/V_G slope (Figure 7-5). The error bars represent the standard error of the mean from those data sets, as described in Chapter 3. The results indicate a reduction of 4 orders of magnitude following the 1×10^{13} cm^{-2} implant. Each successive post-implantation anneal yielded orders of magnitude increases in the mobility. However, even after the highest reasonable anneal, the mobility after implantation is still two orders of magnitude lower than that of the control sample. The 2D carrier concentrations (taken at a backgate value of $V_G = V_T + 20$ V, and using Equation 3-2) were all found to hover a value of 4.6×10^{12} cm^{-2} (Figure 7-5). No correlative affect was observed for implant or anneal. The As and Kr implants mimicked those of P and Ar, though the highest annealing temperature sample for As was lost during handling, before a measurement could be made. Their results are not shown.

Material Characterization Techniques and Results

Material characterizations were performed to observe and understand the structural damage that might occur from implantation, and the repair that might occur after post-implantation anneals. STM is a powerful tool for those purposes, however the inherently defective surface of the as-grown film would likely render any implantation-

induced defects to be indistinguishable from the native defects. Thus, Raman and photoluminescence studies were performed.

Raman Results

Figure 7-6 shows representative spectra for various P implanted samples. The FWHM for the A_{1g} and E_{2g} Raman peaks (Figure 7-7) show an increase in FWHM with increasing implantation dose. Broadening of the Raman peak can be attributed to lattice defects resulting from the implantation [128]. Annealing is shown to improve the FWHM, with the 800˚C anneal returning the value approximately to that of the unimplanted control sample.

Photoluminescence Results

The PL data for the lower doses retains the signature peaks, however the data shows a loss of the peak for the higher dose of 1×10^{14} cm^{-2}, for both implant species, indicating severe structural damage (Figure 7-8). For lower doses, the PL peak FWHM is improved with annealing, like the Raman Data (Figure 7-9). The 300˚C anneal improves the PL yield, while the 800˚C produces a narrower PL peak.

<div align="center">

Discussion

</div>

The films were easily damaged by the implantation. This has been reported before. A study that irradiated natural and grown MoS_2 found that the S-loss occurred more rapidly in the grown film than in the natural material. Native defects within the films can allow for easier defect formation, though that effect will vary across growth methods, due to the different defects that dominate different methods [100], [129], [130], [71].

Implantation induced a defect that lowered mobility. The defect was repaired with annealing, but not fully. The defect did not compensate carriers. The lack of carrier

compensation for implanted films has been reported [100].Polycrystalline MoS_2 films did not experience the same peak BE shifts in XPS that the natural material did, believed to be due to the native defects in the films acting like the implanted damage.

The electrical results indicate that implantation doses higher than 1×10^{13} cm^{-2} are unfit for doping, due to the structural damage and loss of device modulation. For the 1×10^{13} cm^{-2} dosed sample, modulation remains after implantation, but while annealing does repair the damage induced by implantation (indicated by the improved Raman and PL FWHM following anneals), the I_{ON} remains an order of magnitude lower than those of unimplanted devices. Additionally, the transfer curve for every device was found to be n-type; no p-type devices were created, in contrast to the P implants with PIII. However, the with PIII, ambipolar behavior was only observed for the 0V implants, while our implants were performed at 200 eV. This suggests that even at accelerating voltages that are ultra-low compared to typical implantations in bulk semiconductors, the damage created by implantation is too much to overcome even with annealing in H_2S.

There are two possibilities for why the on-current is so low even after the Raman FWHM has return: implantation-induced defects remain after annealing, or the p-type dopant (whether adsorbed or activated) compensates the natural n-type behavior of the MoS_2. The 2D carrier densities showed little difference between each other (Figure 7-5) so the doping effect is not expected. The effect is only observed on the mobility.

It is also likely that the grown film itself has significant impacts on the damage and repair process. The film is textured, with grain boundaries that are terminated by S and S_2 antibonding sites [71]. Studies have shown anomalous pathways for vacancy formation that can drastically lower or alter their formation energies, for grown films with

defects [131]. The grain boundaries play an important role in these pathways, as do vacancies, which would be created during implantation. It's possible that the implantation damage combined with the anneal altered the overall defect character in the films, though additional simulations would need to be performed to determine the effect of an implantation on those pathways. The grown material may not be the ideal material for studying a doping method that is inherently damaging, or one that relies on the diffusion of the dopant. For example, grain boundaries could getter the dopants and prevent their diffusion to an active lattice site.

Summary

The experiment studied damage, repair, and dopant activation for implants on grown MoS_2 films. Samples were compared to unimplanted, unannealed devices on grown MoS_2 films. The grown films were highly vulnerable to implant damage, in agreement with reports [100]. Implant damage reduced I_{ON} by $10^3 - 10^5x$ and broadened the Raman peak FWHM. Damage and structural disorder from the high-dose implant (1×10^{14} cm^{-2}) was significant: films no longer produced the characteristic PL peaks for MoS_2, and devices would not modulate under an applied gate voltage. In contrast, the reduced damage from the low-dose implant (1×10^{13} cm^{-2}) yielded functioning devices with an I_{ON}/I_{OFF} of $10^3 - 10^5$. The defects created from the low-dose implant affected carrier mobility, which decreased in parallel with I_{ON}, but the defects did not compensate carriers. Annealing was beneficial but was unable to fully repair the implant damage: I_{ON} and μ remained 10x lower than the control, following the highest temperature anneal. The origin of the remaining defect was not identified, and its relation to the high concentration of native defects in grown films was not determined. No dopant activation was observed. Damage dominated the results.

Sample	Species	Dose	Anneal
1	P	1e13	none
2	P	1e13	15 min, 300°C sulfur anneal
3	P	1e13	15 min 800°C sulfur anneal
4	P	5e13	none
5	P	1e14	none
6	P	1e14	15 min, 300°C sulfur anneal
✗ 7	P	1e14	15 min 800°C sulfur anneal
8	As	1e13	none
9	As	1e13	15 min, 300°C sulfur anneal
10	As	5e13	none
11	As	1e14	none
12	As	1e14	15 min, 300°C sulfur anneal
13	Ar	1e13	none
14	Ar	1e14	none
15	Kr	1e13	none
16	Kr	1e14	none

Figure 7-1. Experimental design matrix. Succintly enumerates the implantations and anneals that were performed. Sample 7, with the red X, was destroyed during processing so there are no results for that condition.
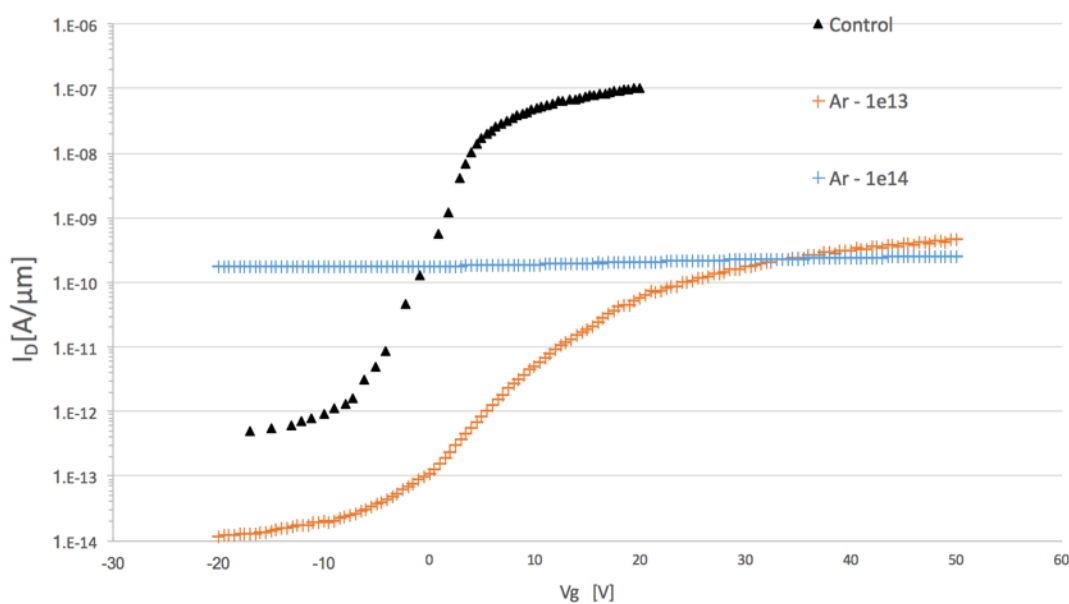
Figure 7-2. Transfer curves for MoS_2 films implanted with Ar at 500 eV, and at doses of 1×10^{13} and 1×10^{14} cm^{-2}. Compared against an unimplanted, unannealed control sample.
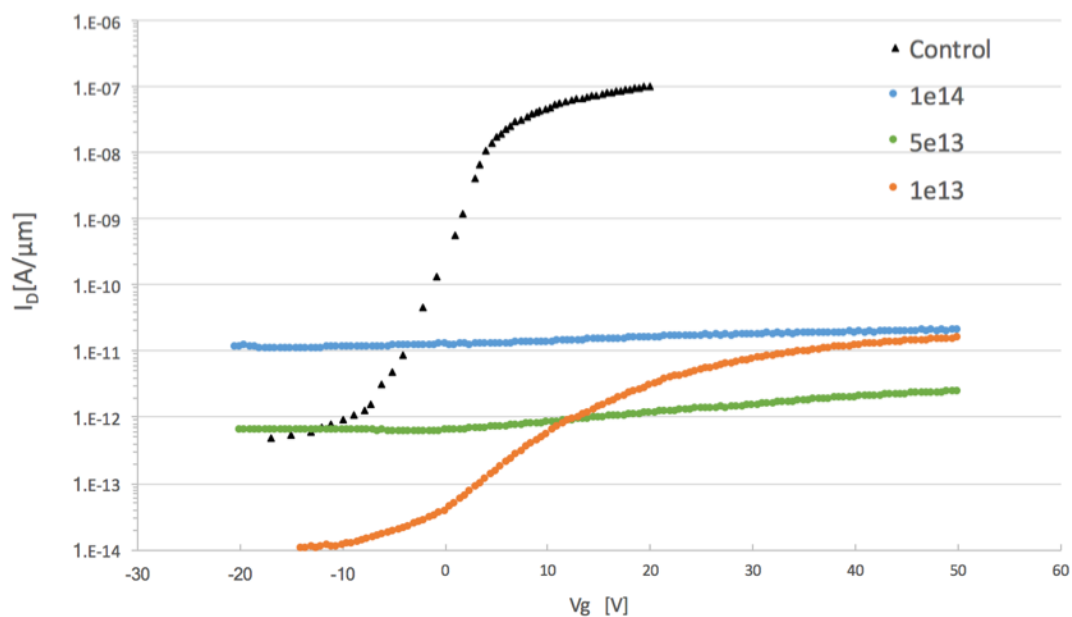
Figure 7-3. Transfer curves for MoS$_2$ films implanted with P at 500 eV, and at doses of 1 x 10^{13}, 5 x 10^{13}, and 1 x 10^{14} cm^{-2}. Compared against an unimplanted, unannealed control sample.
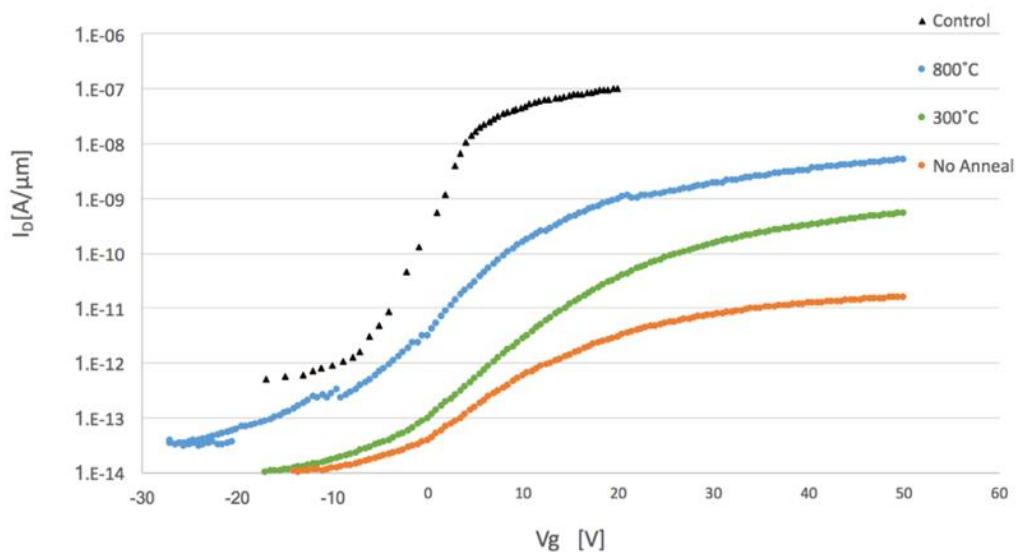
Figure 7-4. Transfer curves for MoS$_2$ films implanted with P at 500 eV, and at a dose of 1 x 10^{13} cm^{-2}, and annealed in H$_2$S for 15 minutes at 300˚C, 550˚C, and 800˚C. Compared against an unimplanted, unannealed control sample.
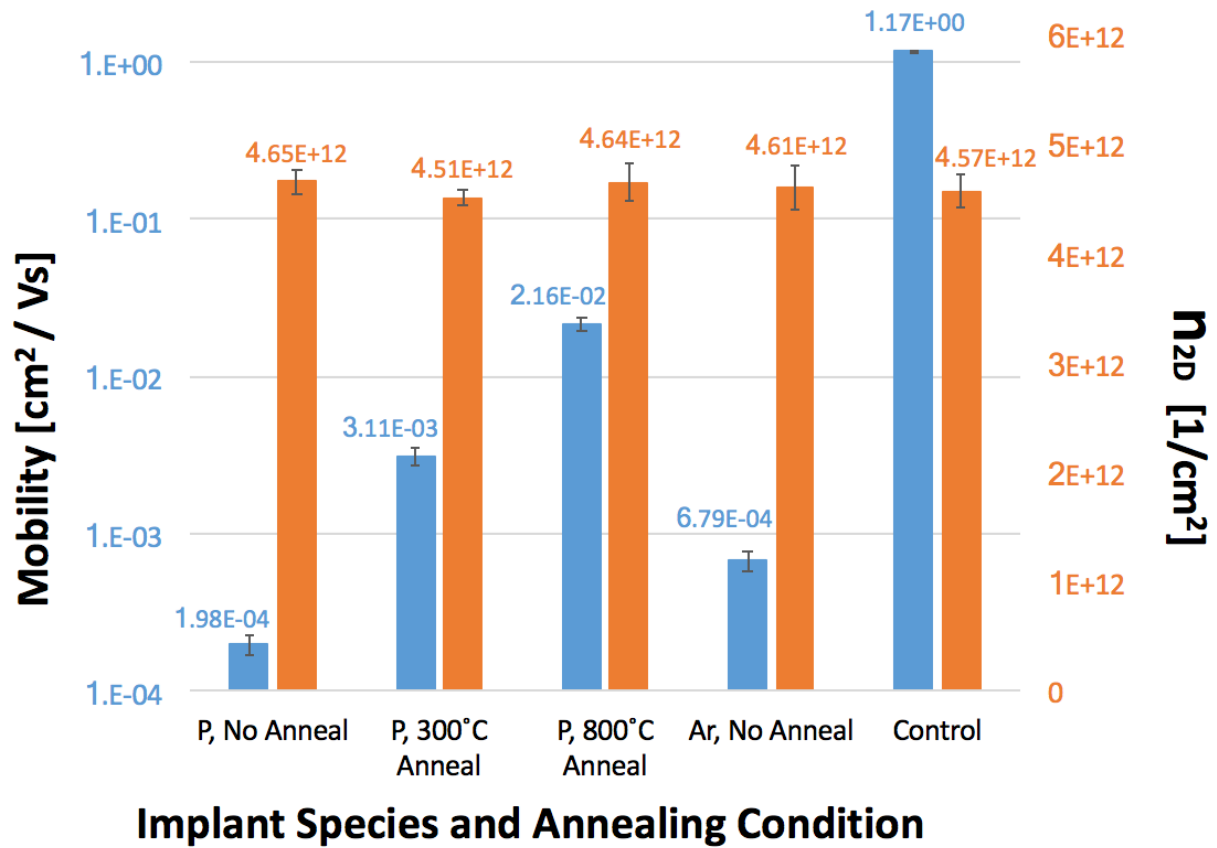
Figure 7-5. Mobilities and 2D carrier densities for implanted and annealed films. Values were extracted from the transfer curves of multiple devices. The error bars represent the standard error of the mean of those data sets.
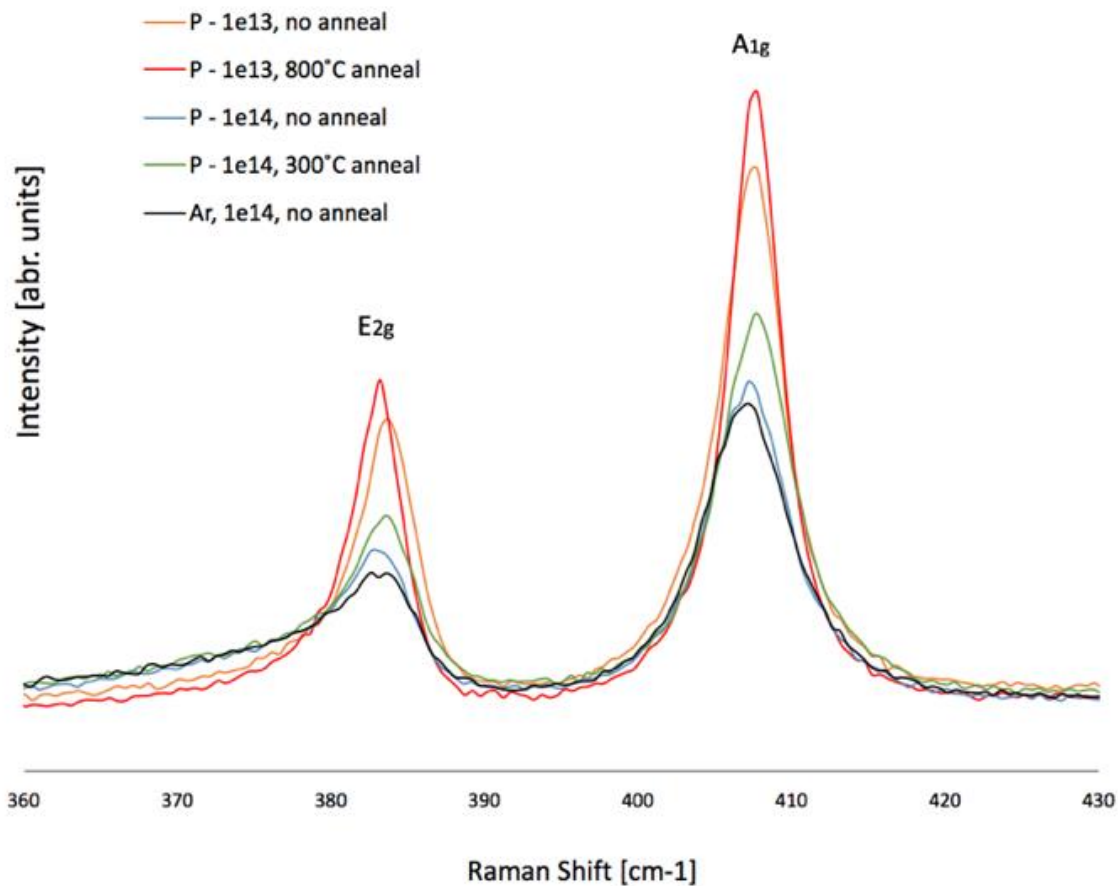
Figure 7-6. Raman spectra for MoS_2 films implanted at 200 eV with the listed species and dose, and annealed in H_2S for 15 minutes at the listed temperature.
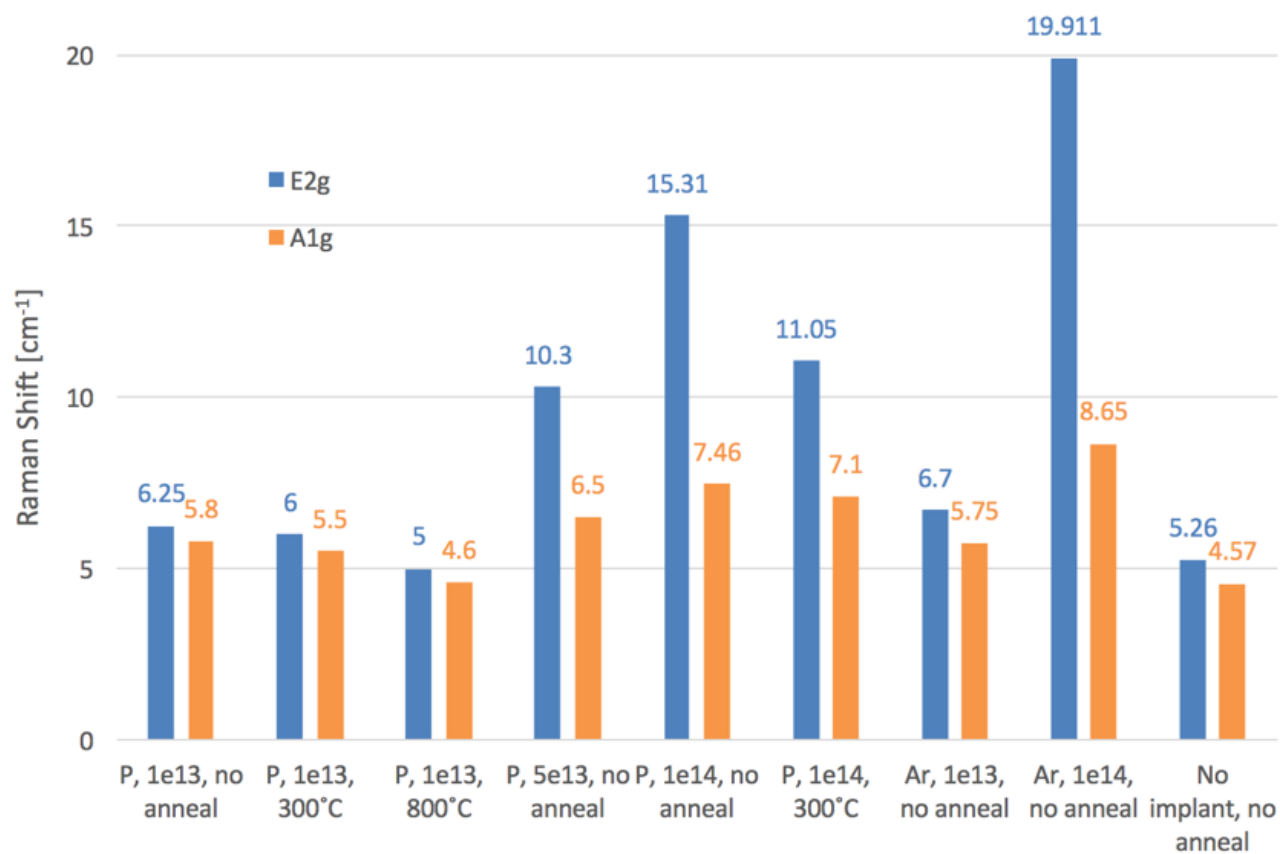
Figure 7-7. FWHM of Raman peaks for MoS_2 films implanted at 200 eV with the listed species and dose, and annealed in H_2S for 15 minutes at the listed temperature.
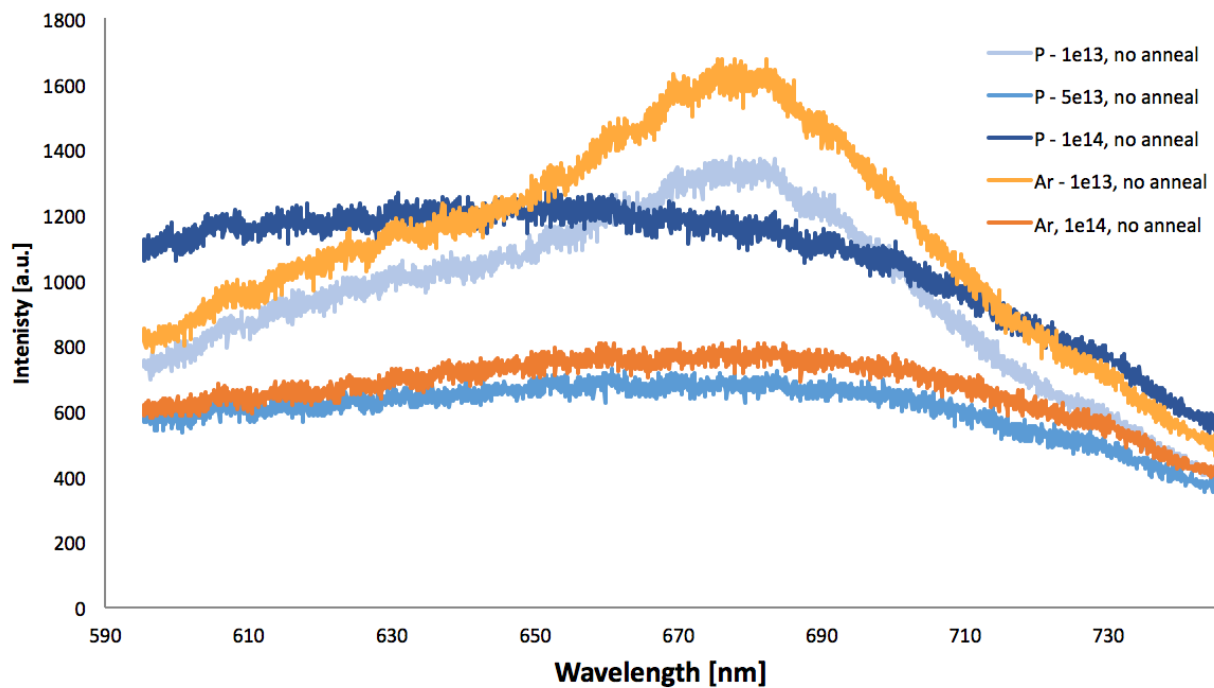
Figure 7-8. Photoluminescence data for MoS$_2$ films implanted at 200 eV, with the listed species and dose
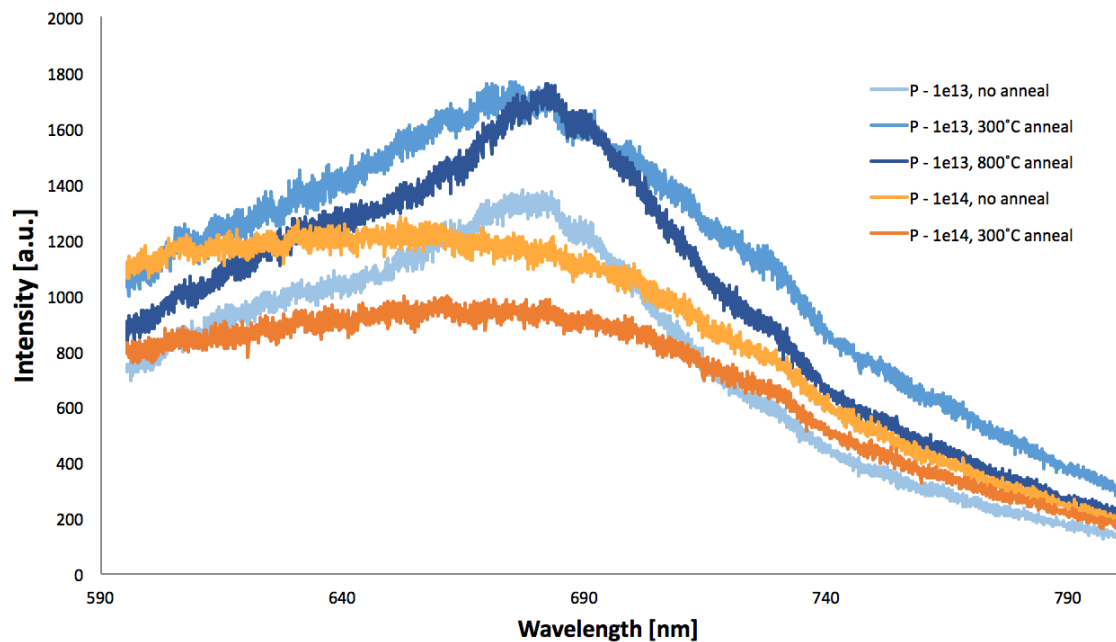
Figure 7-9. Photoluminescence data for implanted and annealed MoS$_2$ films.

CHAPTER 8
F AND P IMPLANTS AND ANNEALS OF NATURAL MoS$_2$

The previous chapter made progress by employing characterization techniques to correlate a cause and effect. Raman and PL measurements showed that a higher implanted dose leads to increased structural disorder of the MoS$_2$, as was initially shown with STM in Chapter 5. Annealing in a H$_2$S ambient was also seen to reduce the structural disorder. Meanwhile, characterization of fabricated electrical devices indicated that the material's electrical properties follow that of its structural, as would be expected.

However, ion implantation is a process that at its basic level involves, and ideally controls, the creation and repair of defects. This makes ion implantation experiments particularly susceptible to effects from pre-existing defects. Consequently, the inherent defective nature of the grown films used in the previous chapter may have masked or exaggerated aspects of the experiment. For example, it's unclear how the low grain size (~10-100 nm in diameter) and high concentration of grain boundaries influenced dopant activation or the reduction in disorder during the post-implantation anneals [69]. Trends in the results were certainly clear for the grown films, but atomically resolving and parsing the high concentration of native defects from the experimentally-induced defects was not feasible through accessible tools. Thus, the fundamental material reasons that drove the observable trends could not be identified. This chapter seeks to eliminate those concerns by using pristine, exfoliated MoS$_2$, which will always have a concentration of native defects but typically at much lower levels than grown films, as can be seen with the reduced mobility in devices fabricated on grown films, [115], [132]. Reducing the added variable of the pre-existing defects may provide a clearer picture of the phenomena at play and may help answer questions regarding the types of defects

formed by implantation, the evolution of the defects with annealing, and the role of the implanted species throughout the anneals.

The dose for these experiments was limited to 1×10^{13} cm^{-2}, at an energy of 500 eV. Both an n-type (fluorine) and a p-type (phosphorous) dopant species were used. Post-implantation anneals were performed in an H_2S atmosphere. Implanted exfoliated flakes were used to fabricate and characterize devices, while bulk material was used to probe the atomic surface through conductive AFM (CAFM).

Implantations and Anneals

In line with experiments performed in the previous chapters, phosphorous was used as the p-type dopant species. However, the previously used n-type dopant, chlorine, was unavailable due to limitations with the ion implanter tool. Fluorine was thus chosen as the n-type dopant.

Like Cl, F has an additional valence electron when compared to S, giving F the potential to be an n-type dopant in MoS_2. Fluorine been modeled to have a favorable formation energy of -5 eV for substituting onto an S vacancy, and to be an n-type dopant that creates energy states below the conduction band, near where the Fermi level is pinned at the metal/MoS_2 interface [129], [124]. Additionally, other models suggest that F in an MoSF alloy will donate its electron so readily that it will drive the Fermi level into the conduction band [133]. However, fluorine's efficacy as a dopant remains to be experimentally reported, and the high electronegativity of fluorine might imply it is less willing to donate an electron. This has been somewhat corroborated experimentally [106]. However, in that case the F atoms were present as ligands on a long chain attached to the MoS_2 surface, and they were not chemically bonded with the Mo, as would happen with substitutional doping. Additionally, the p-type effect was

130

observed as only a minimal compensation of the native n-type 2D carrier density reducing it from 9×10^{11} cm^{-2} to 7×10^{11} cm^{-2}. However, chlorine also has a high electronegativity and it has been shown to be an effective n-type dopant in MoS$_2$, so F may indeed be an electron donor in MoS$_2$ [42].

Due to an additional limitation of the implant tool, the implant energy was increased from 200 eV, as used in the previous chapters, to 500 eV. SRIM results suggest a projected range of 2.1 nm and 1.8 nm, for F and P, respectively. No inert species were implanted. Only a single dose was used, 1×10^{13} cm^{-2}. Following implantation, H$_2$S anneals were performed at temperatures of 300˚C, 550˚C, and 800˚C for 15 minutes prior to device fabrication (the 550˚C annealed sample was only used for structural characterization). A control sample did not receive any implantation or anneal.

Device Fabrication and Electrical Results

Flakes of MoS$_2$ were mechanically exfoliated onto Si/SiO$_2$ (25 nm) substrates. Flakes ~10 layers thick were identified under an optical microscope based on matching their optical contrast (see Chapter 3) to that of flakes whose thickness had previously been determined with AFM. The flakes were first implanted and then annealed. Devices were patterned onto the flakes using masked optical lithography, by aligning features on the mask to desired flakes. The features were large contact pads separated by a 5 µm channel. The resulting transfer curves are presented in Figures 8-1 and 8-2 with I$_{DS}$ in a log and linear scale, respectively. The control sample exhibited an excellent I$_{ON}$/I$_{OFF}$ of 9.2×10^7 (Figure 8-3). The as-implanted, 300˚C, and 800˚C I$_{ON}$/I$_{OFF}$ ratios for the P implant were 2×10^6, 3×10^7 and 1×10^7. For the F implant they were 2.8×10^6, $.6 \times 10^7$, and 6.1×10^6. A pattern emerged for both species: the unannealed sample has the

lowest I_{ON}/I_{OFF}, the 300˚C annealed sample has the highest I_{ON}/I_{OFF}, and the 800˚C

sample is in between the other two.

A clear trend is present when comparing the on-currents in each device (Figure

8-4). For this comparison, V_G for all devices was taken to the same overdrive voltage,

arbitrarily chosen as 7 V. That is, I_{DS} is taken along the transfer curve at the point where

V_G is 7 V above the threshold voltage. This ensures each sample is under similar

electrostatic effects and allows for fair comparisons to be made between devices. The

values were averaged around that point on the transfer curve to account for error in the

I_{DS}/V_G slope. The error bars represent the standard error of the mean from those data

sets. The control sample has the highest on-current (4.55 µA/µm), and both

implantation species follow the same trend. Implantation reduces the on-current, to 0.63

µA/µm for P, and to 0.19 µA/µm for F, which are reductions of 7x and 23.5x relative to

the control sample. For the 300˚C anneal, the on-current for the P implant increased to

1.73 µA/µm, and the on-current for F increased to 0.63 µA/µm. The 800˚C anneal

increased the on-current for the P implant to 2.13 µA/µm, and to 1.4 µA/µm for the F

implant. Thus, each anneal improved the on-current by a factor of 1-3, though even

after the 800˚C anneal, the highest on-current is less than half that of the control sample

(2.13 µA/µm, for the P implant, compared to 4.55 µA/µm for the control). The P-

implanted material always yielded higher on-currents compared with the F implants.

Equation 3-1 and Equation 3-2 were utilized to extract the field effect mobility, µ,

and 2D doping density, n_{2D} (Figure 8-5). Effects of the contact were not removed in this

analysis, so this is the extrinsic mobility and is a low estimate. The values were

extracted at $V_G = V_T + 7$, like in the comparison of I_{ON}, and were averaged from multiple

points around that point to account for error in the V_T and I_{DS}/V_G slope calculations, as described in Chapter 3.

The trend for mobility is the same as that of the on-currents: implanting reduces the value and annealing improves it, but never back to that of the control sample (17.35 cm^2/Vs). The μ values for the as-implanted, 300˚C annealed, and 800˚C annealed samples for the P implants were 2.75, 7.81, and 11.19 cm^2/Vs, and for the F implants were 0.88, 3.32, 7.39 cm^2/Vs. Like the on currents, mobility was always higher for the P implants. Thus, the mobility is initially reduced by ~7x and ~17x following the P and F implants, and it remains 1.5x and 2.2x lower for the P and F implants after the 800˚C anneal, when compared to the pristine material. The n_{2D} values for the implanted and annealed samples fluctuate from 6.05 to 6.68 x 10^{12} cm^{-2} and do not appear to follow a trend. For comparison, n_{2D} for the control sample is 9.10 x 10^{12} cm^{-2}; n_{2D} was reduced by ~30% on average following implantation.

Surface Analysis: Conductive AFM

The topological and electrical properties of the MoS_2 surface were probed with conductive AFM (CAFM) in constant-force mode. CAFM characterizations were performed by Xueying Zhao in collaboration with Dr. Scott Perry at the University of Florida. Images were taken on pristine material, on implanted material, and after each anneal. Conductive AFM is similar to STM. However, with CAFM, the AFM tip is pressing on the surface while applying a constant force, whereas the STM tip tunnels current through a gap. The CAFM tip scans the surface and applies a voltage. Any changes in the electrical properties will be recorded, but the tip will not toward or away from the sample, like in STM, because the force that the tip applies to the sample is

held constant. This allows for simultaneous measurements of the electrical and topological properties of a region with high resolution.

Pristine MoS_2 (Figure 8-6) was found to contain defect-free regions as well as regions with defect concentrations of 9 x 10^{10} cm^{-2}. The defects are observed as regions of darker contrast where a reduced current was measured. The lack of visible defects in Figure 8-6A does not suggest there are no defects in the nearby area, it only means defects exist in concentrations lower than are visible within the length scales of the image frame. The 80 x 80 nm^2 area in Figure 8-6A places an upper limit of 1.5 x 10^{10} cm^{-2} for the defect concentration in that area, which is within an order of magnitude of the defect concentration observed in Figure 8-6B. Local variations in the concentration of surface defects is expected and commonly reported for MoS_2 [132], [134].

Figure 8-7 reveals images of the MoS_2 surface after implantation with a 1 x 10^{13} cm^{-2} dose of F at 500 eV. There is a clear emergence of defects when compared to the pristine sample image in Figure 8-6A. The implant defects have a density of ~1.5 x 10^{12} cm^{-2}, or approximately one order of magnitude lower than the implanted dose, and approximately 1.5 orders of magnitude higher than the native defects (9 x 10^{10} cm^{-2}) seen in Figure 8-6B. Notably, the defects in Figure 8-6B and Figure 8-7 are of demonstrably different sizes: the average diameter of the native defects in Figure 8-6B is approximately 15 nm, while the implant defects in Figure 8-7 are roughly 2-3 nm in average diameter.

Figure 8-8 is a high-resolution image of the MoS_2 surface after implantation and the lowest temperature anneal: 300°C for 15 minutes in H_2S. It is a simultaneous capture of the surface topology (Figure 8-8A) and electrical topology (Figure 8-8B) of

the same area. The result was consistent across the sample and across every sample imaged. The figure highlights an important aspect observed among defects for every implant and anneal condition in this experiment.

The topologies of Figures 8-8A and 8-8B are from the same area but do not correlate: the surface topology in Figure 8-8A is flat, while Figure 8-8B shows a non-uniform electrical topology with peaks and valleys. A minor topological defect in Figure 8-8A could not induce the electronic response observed in Figure 8-8B. Thus, for the implantation parameters used in this experiment, the defects induced by implantation can influence the local electrical environment of the surface, but the defects are located in the subsurface region and do not disrupt the local structural order at the surface. Similar results have been found for CAFM studies on defects in pristine MoS_2 surfaces that received no implantation or other treatment [104]. Models have predicted that the S atom on the bottom of the tri-layer sheet will sputter more easily than the S on the top, due to the rigid structure below the top S holding it in place, which could partially explain the observations in Figure 8-8 [129].

Figures 8-9, 8-10, and 8-11 portray the evolution of defects throughout the experimental annealing range. Attempts to quantify any observed damage repair could include methods such as counting the number of defects, extracting a density, and comparing it to the as-implanted value of ~1.5 x 10^{12} cm^{-2} extracted from Figure 8-7, as well as to the native value of 10^{10} cm^{-2} from Figure 8-6. However, the images of annealed samples do not provide a clear path for that method. The annealed samples contain defects, but not discrete defects that are easily counted when imaged through CAFM, unlike the defects observed after implantation and before annealing (Figure 8-7).

Comparing the images qualitatively, the defects almost appear to coalesce or agglomerate with increasing annealing temperature, as opposed to healing in a manner that would return the surface back to the uniformity observed prior to implantation (Figure 8-6A). This potential defect agglomeration or enhancement is highlighted by comparing the pristine, as-implanted, and 800°C annealed samples side by side. This is provided for convenience in Figure 8-12. Additionally, Figure 8-13 reveals a larger surface area than the previous images to provide a more macroscopic view of the surface following the highest temperature anneal used in this study (800°C).

With a lack of discretely countable defects after annealing, the surface defect environment was quantified based on image contrast. The image analysis software ImageJ was used to reduce image contrast to black and white. The process involves choosing a threshold contrast value in the initial image. After processing, all contrast values above or below the threshold were split into black or white. The threshold value was manually set, which could introduce a source of human error. The threshold value was chosen to best fit the dark area of a defect, and to exclude the contrast gradient surrounding defects.

Figure 8-14. compares the total perimeter of the defects with the total area of defects (represented as a percentage of the total area). Defect perimeter is seen to decrease with annealing temperature, while total defect area is seen to increase. If the defects were combining to reduce their interfacial energy with the pristine material, then the perimeter would decrease while the area remained constant. In the case of these implanted and annealed samples, the total defect perimeter decreases but the total defect area increases, implying additional reactions are dominating the defect evolution.

Discussion

Irradiation has been shown to remove S, and lead to the creation of Mo-clusters, which compensate charge. This could explain some initial reduction in 2D carrier density following implantation [99], [100]. However, annealing at high temperatures would expect to repair that damage. MoS_2 is grown at 800°C from Mo and H_2S [69]. The result points to a different defect, but it does not rule out the Mo-cluster as source for the continued carrier compensation.

Numerous factors influence defects and their behavior in a system like this, which throws this system beyond the bounds of many modeled predictions. Three factors contribute significantly.

First, the material has been implanted and it contains a higher density of defects (~10^{12} cm^{-2}) than MoS_2 typically does (~10^{11} cm$_{-2}$). Defects have been shown to reduce the barrier of diffusion for other nearby defects, for example, the energy barrier for S vacancy (V_S) diffusion will reduce from 2.4 to 0.8 eV in the presence of a nearby vacancy [135]. Defects have also been shown to lower the formation energy (E_f) of other defects. Models indicate that nearby V_S can have a 0.05-0.2 eV advantage for forming a line, and for chains longer than eight vacancies, a double vacancy is favorable [135]. The double line would occur with one line on top and one line on bottom of the Mo, on opposite sides. Other models have shown that when a Mo vacancy forms (V_{Mo}), the system will want to remove three sulfur atoms and relax into a MoS_3 vacancy (V_{MoS3}) [136].

Second, it's a S-rich environment, with the H_2S atmosphere. This influences the chemical potential of S, μ_s, which is directly relatable to the E_f of defects in the system.

This will drive down E_f for some defects, but raise it for others. For example, E_f for an S sitting on a Mo site (S_{Mo}) reduces to 1.9 eV at the S-rich limit, down from 9 eV at the S-poor limit [93]. The sulfur interstitial defect (S_i) has lowest E_f for the S-rich environment, at ~1.1 eV [131]. S_i diffusion through the gap has a low barrier of only 0.08 eV, so in a H_2S anneal there could be a high density of fast moving S_i [93]

Third, it's an anneal and high temperatures are involved. Atoms will have more energy than what many models have accounted for. Combined with the other two factors, species will be able to diffuse more often, and defects will be created more often.

The three factors will feed off each other. Some defects will not recover. If a Mo atom vacates is lattice (E_f = 3 eV at the S-Rich limit), and diffuses out of the system, it will not be repaired by the H_2S anneal.

Additionally, it should be noted that the observed defect evolution with anneals is different from reports and from experimental observations. In previous experiments not reported here, MoS_2 samples were implanted with a 200 eV, 1 x 10^{13} cm^{-2} dose of Cl and were scanned with STM. The system was heated to 550°C for 5 minutes in the STM chamber (10^{-10} torr), allowed to return to room temperature, and imaged again. The process was repeated for 750°C. The images reveled no major changes after annealing, and the defect density ranged from 4.2, to 3.4, to 2.7 x 10^{12} cm^{-2} throughout the anneals, which are similar to the density seen in the as-implanted sample in this experiment (1.5 x 10^{12}, Figure 5-7). Reports have also irradiated MoS_2 with Ar at 1 keV, heated them, and imaged them with STM [137]. The samples were imaged at room temperature, heated to 600°C and imaged at temperature, heated to 800°C and

measured at temperature again. The samples were then allowed to return to room temperature, and were measured again. The defect density was not reported, but a count of the reported images before, during, and after the anneals reveals a density of $1.7 - 3.4 \times 10^{11}$ cm^{-2} for a dose of 1×10^{12} cm^{-2}. The defect density to dose ratio (~0.1) is roughly similar to that observed in these experiments (1.5×10^{12} cm^{-2} defect density and 1×10^{13} cm^{-2} dose, Figure 8-7). The only reported effect from the anneal was a reduction in the defect diameter at high temperatures, but it was not retained when the sample returned to room temperature. For both room temperature images, the defects were 6-8 nm in diameter, and they were 2-4 nm for both high temperature measurements, implying a reversible relaxation of the defect edge. That relaxed edge may provide for a reaction site at the high temperatures.

The major difference between those experiments (which saw no damage evolution) and these experiments (which saw damage evolution) was the H_2S atmosphere. The implant species were different, but Ar is relatively inert, and Cl would be expected to behave similarly to F, given their relation as highly electronegative halogens. The catalyst for damage evolution appears to be the H_2S atmosphere. That result is counterintuitive, because synthetic MoS_2 is often grown or later annealed in H_2S, which results in improved crystallinity [69].

As mentioned, an S-rich environment will shift defect E_f, while also introducing fast moving S_i defects into the MoS_2 gap [93], [93]. The implant damage occurred beneath the surface (Figure 8-8), so the mobile S_i will have easier access to these sites. S_i defects are not expected to be a dopant [138]. With the abundance of free S, S

vacancies are likely not the source for the damage evolution, but it does not rule out S from being an intermediary in the damage evolution.

The electrical measurements on devices were shown to improve with anneal, despite the damage evolution. The electrical performance can be can be broken down into its mobility and carrier density components, both of which decreased after implantation. The carrier density fluctuated with no correlation to the anneal, while the mobility was clearly seen to improve with the anneal. This implies a difference in the origin of the responses. The implant creates a defect that is not repaired by the H_2S anneal, and this defect compensates the intrinsic charge. A Mo vacancy (V_{Mo}) or vacancy complex would not be repaired by an H_2S anneal, since H_2S cannot supply the Mo. Models have predicted V_{Mo} to be a strong acceptor in bulk MoS_2, with a stable charge state ranging from -1 to -3, so Mo would likely contribute to the reduction in n_{2D} [93].

Additional anneals and CAFM studies are necessary to further characterize the behavior. Modeling of the system will aid in identifying the interactions taking place.

Summary

Damage, repair, and dopant activation for implants on natural MoS_2 was studied. CAFM observed the implant damage as dark areas with reduced conductivity, 2-3 nm in diameter, at a density ~10x lower than the implanted dose. The defects were located in the subsurface region: in CAFM, they were not physically located on the surface, but they were electrically felt at the surface. Results suggest multiple types of defects are induced by implantation. One defect that reduced mobility (up to 17x), and is partially, but not fully (66% of original), repaired by annealing up to 800°C in H_2S. And another defect that compensates carriers (by ~30%), and is unaffected by annealing up to 800°C

in H_2S. The initial carrier compensation is often attributed to S-loss and Mo-cluster formation. However, that would be expected to be repaired in H_2S at 800˚C. Analysis of CAFM images found an increase in the total dark, defect area with increasing annealing temperature. The result suggests a surface that is damaged with annealing, however that conflicts with the improvement in mobility. Numerous defects are likely involved. The combination of high temperatures, a sulfur-rich atmosphere, and a defect-inducing process (ion implantation) complicates defect analysis. Additional experiments and CAFM analysis, aided by computer simulations, are required to identify the reactions within the complex, dynamic environment created in these experiments. No dopant activation was observed. Damage dominated the results.

.
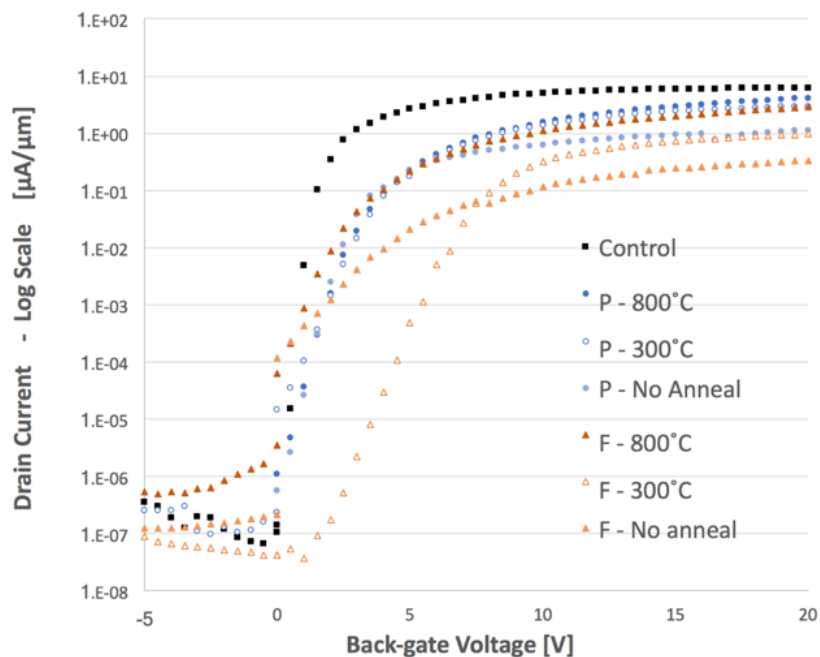
Figure 8-1. Transfer curves for devices fabricated on exfoliated MoS$_2$ flakes. Prior to device fabrication, the flakes were implanted with a 500 eV, 1 x 10^{13} cm^{-2} dose of P or F, followed by 15-min post-implantation anneals in H$_2$S.
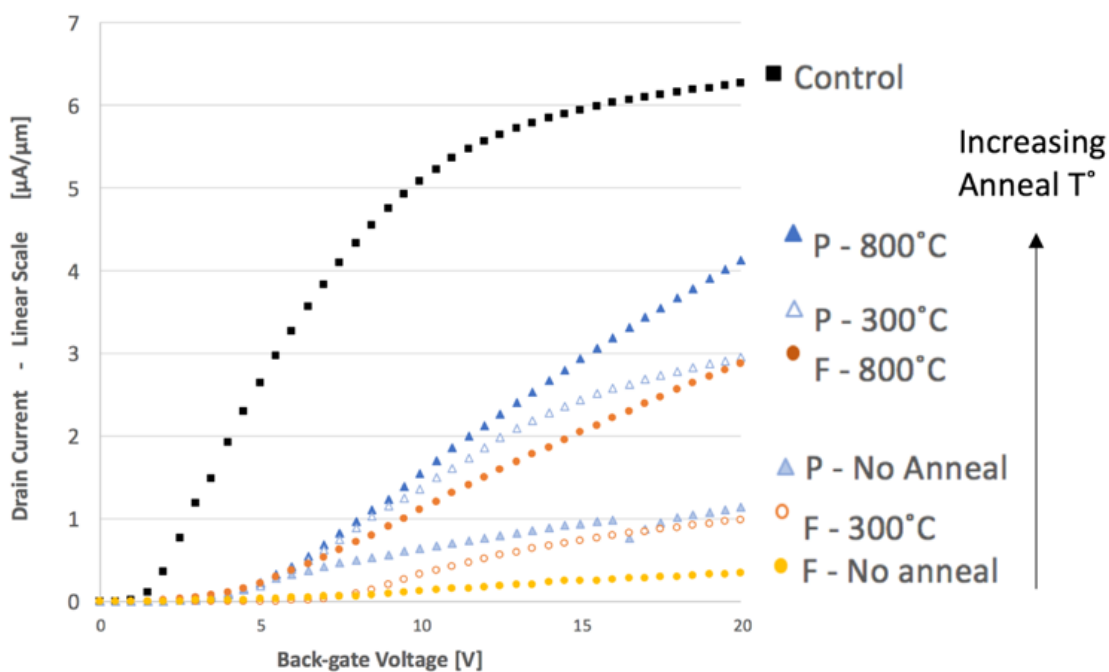
Figure 8-2. A linear plot of the same data as Figure 8-1. Prior to device fabrication, the flakes were implanted with a 500 eV, 1 x 10^{13} cm^{-2} dose of P or F, followed by 15-min post-implantation anneals in H$_2$S

142
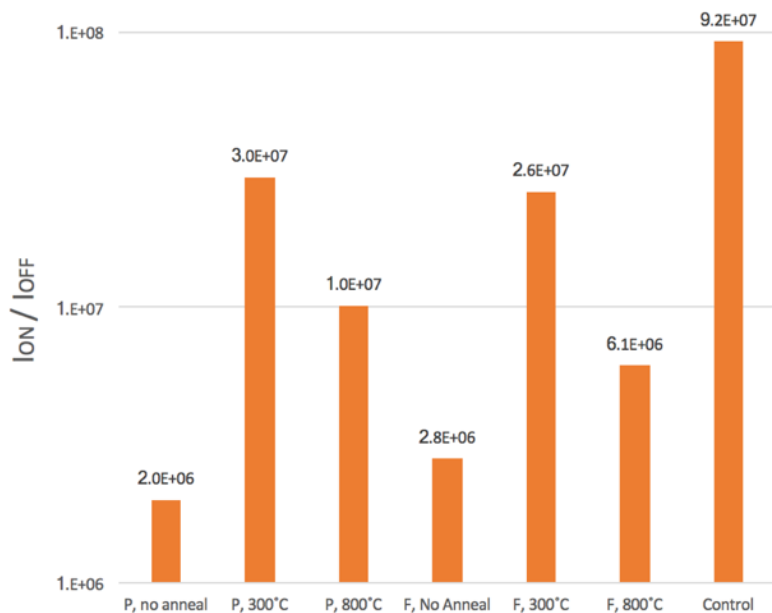
Figure 8-3. A comparison of I_{ON}/I_{OFF} for the data in Figure 8-1. Prior to device fabrication, the flakes were implanted with a 500 eV, 1 x 10^{13} cm^{-2} dose of P or F, followed by 15-min post-implantation anneals in H_2S.

*All values calculated with $V_G = V_T + 7$
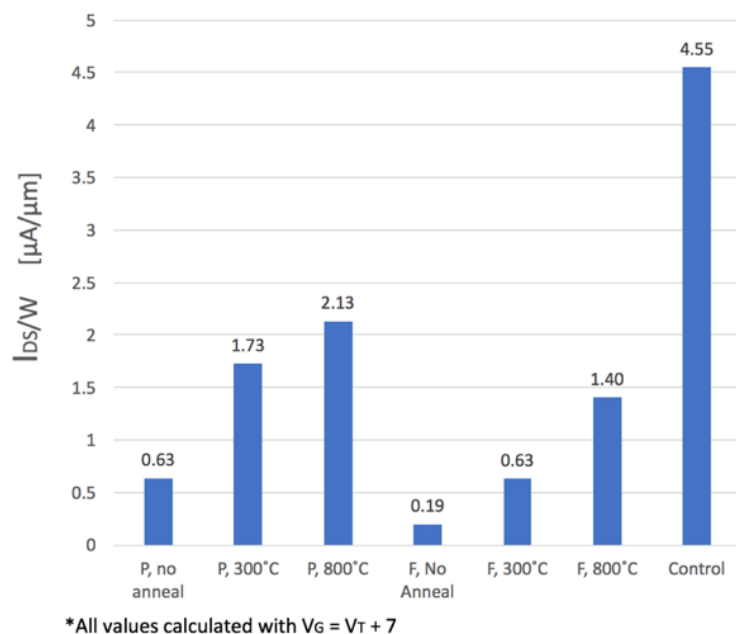
Figure 8-4. A comparison of I_{ON} for the data in Figure 8-1. Prior to device fabrication, the flakes were implanted with a 500 eV, 1 x 10^{13} cm^{-2} dose of P or F, followed by 15-min post-implantation anneals in H_2S.
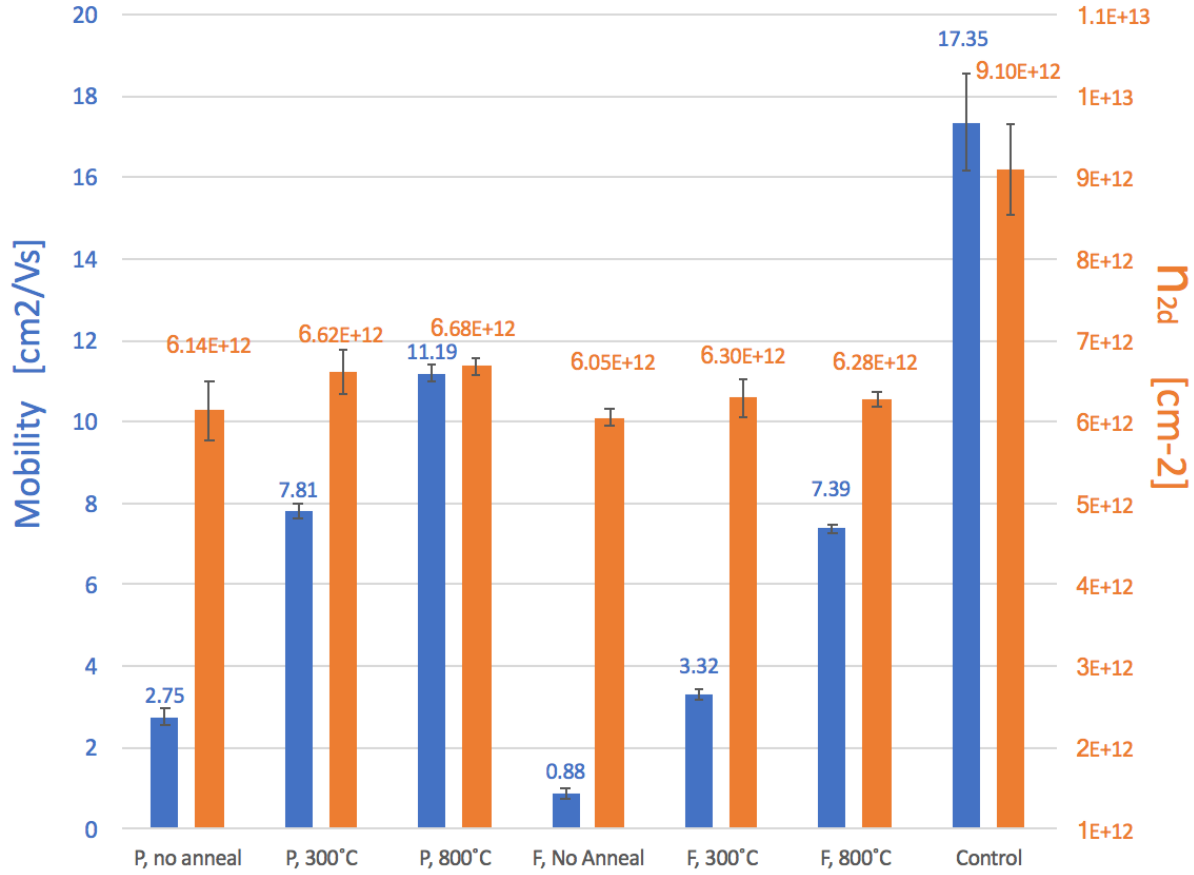
Figure 8-5. The extracted field effect mobility and 2D doping density for the data in Figure 8-1. Prior to device fabrication, the flakes were implanted with a 500 eV, 1 x 10^{13} cm^{-2} dose of P or F, followed by 15-min post-implantation anneals in H_2S. The data points were averaged over multiple nearby points along the transfer curve, to account for error in the approximation if the linear slope I_{DS}/V_G. The error bars represent the standard error of the mean of those data sets.
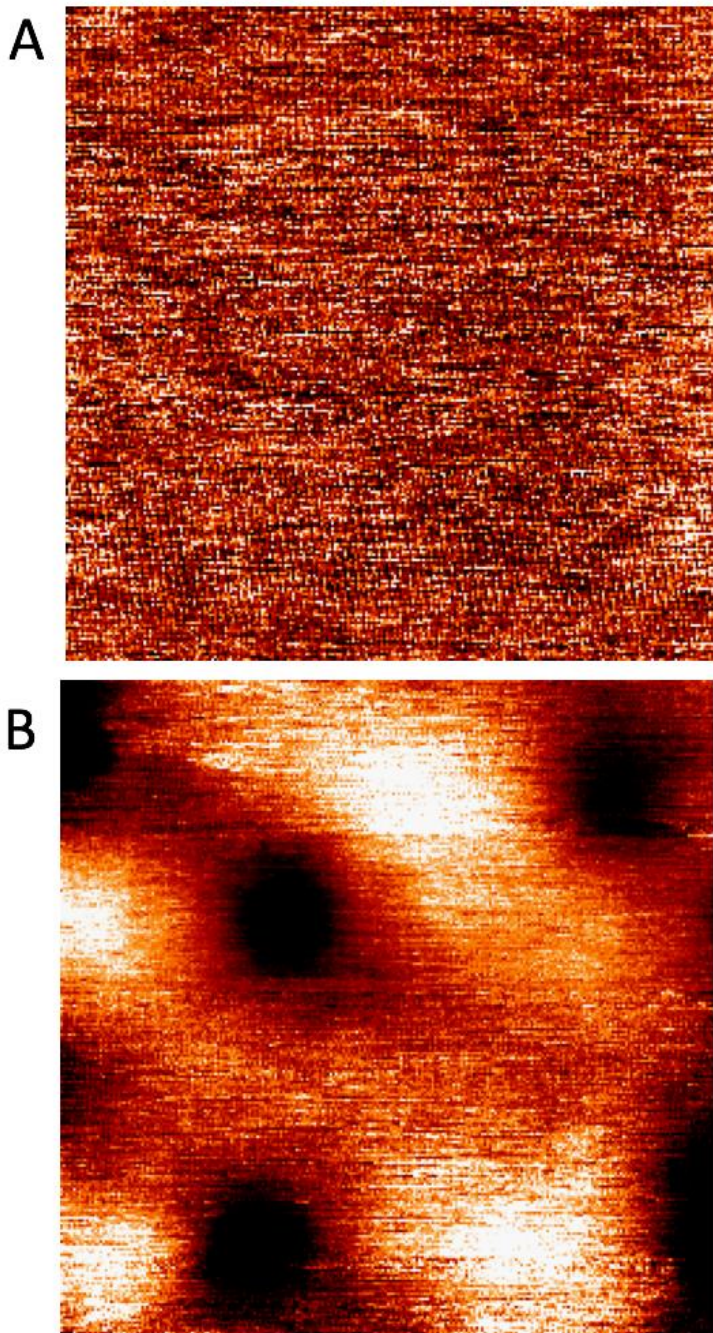
Figure 8-6. CAFM scan of pristine MoS$_2$ (no implant or anneal). A) an area with no defects, 80 nm x 80 nm, V = +1 V B) An area with dark (low-conductivity) defects, ~15 nm in diameter. Six defects at that scale yields a defect concentration of 9.3 x 10^{10} cm^{-2}, 80 nm x 80 nm, V = 0.5 V. Data courtesy of Xueying Zhao.
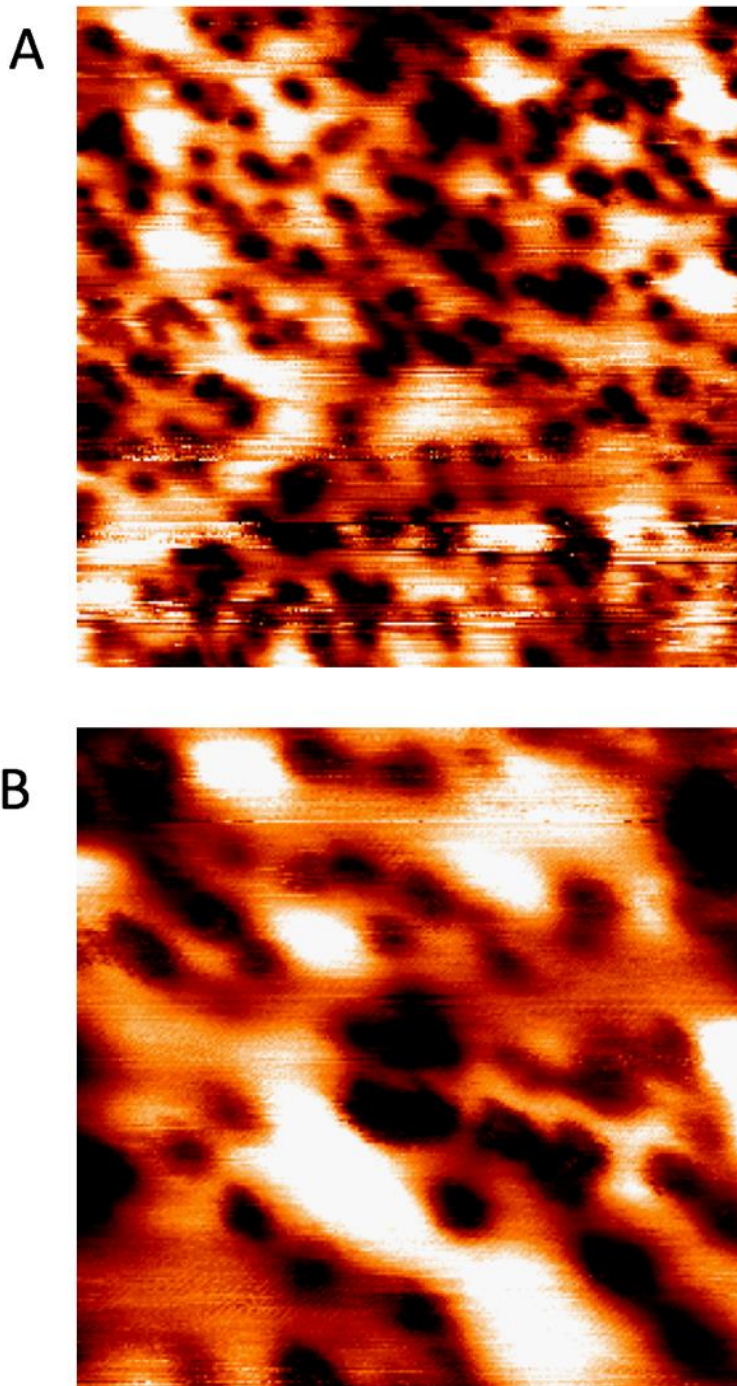
Figure 8-7. CAFM image of MoS_2 after 500 eV, 1 x 10^{13} cm^{-2}, F implant, and 15 minute, 300˚C, H_2S anneal. A) 80 nm x 80 nm, V = +1.5 V. B) 40 nm x 40 nm, V = 1.5 V. Data courtesy of Xueying Zhao.
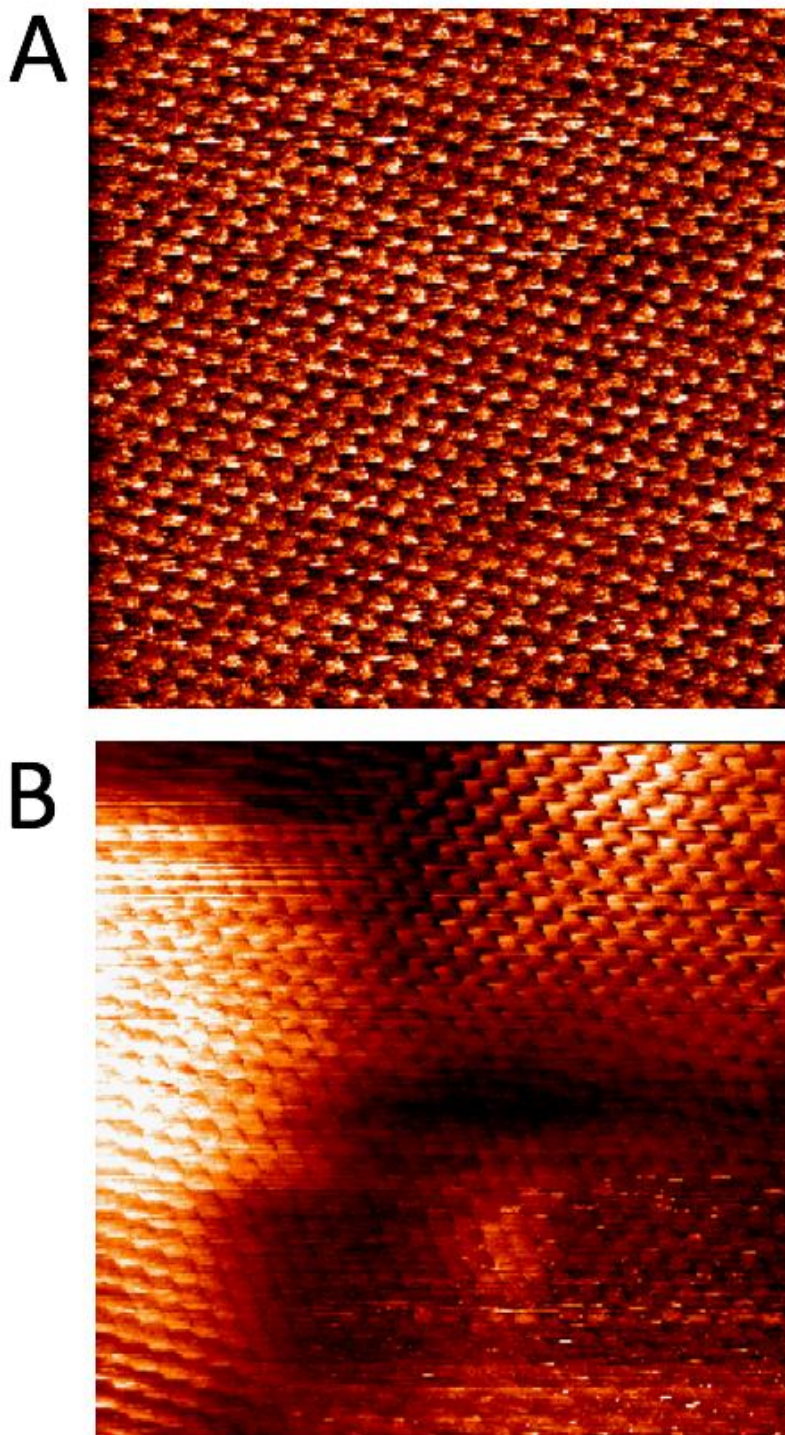
Figure 8-8. CAFM image of MoS_2 after 500 eV, 1 x 10^{13} cm^{-2}, F implant, and 15 minute, 300˚C, H_2S anneal. A) Height image, 8 nm x 8 nm, V = +2.0 V. B) Current image. 8 nm x 8 nm, V = +2.0 V. Data courtesy of Xueying Zhao.
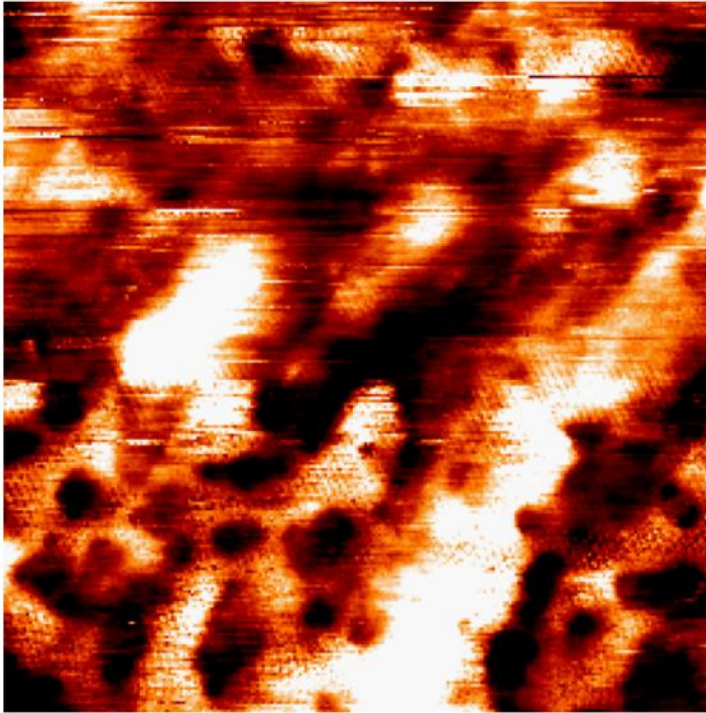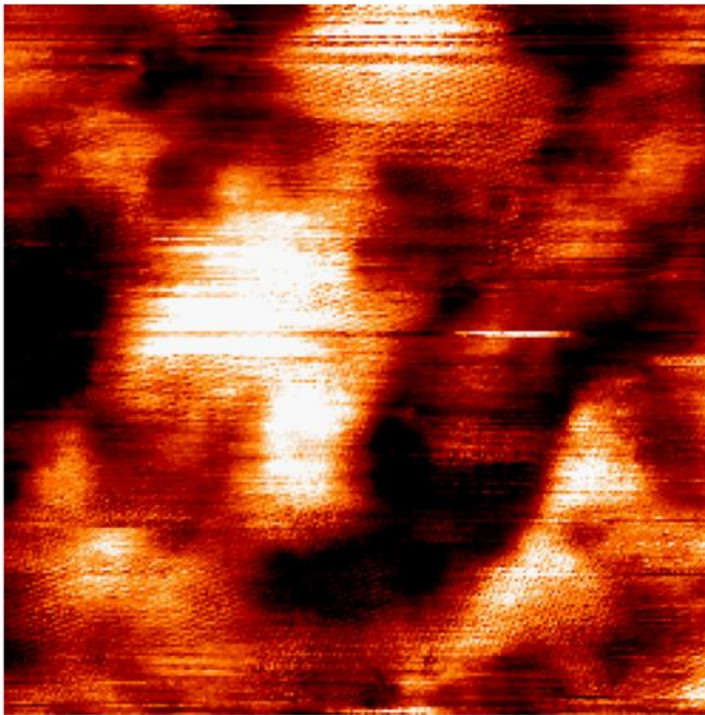
Figure 8-9. CAFM image of MoS_2 after 500 eV, 1 x 10^{13} cm^{-2}, F implant, and 15 minute, 300˚C, H_2S anneal. A) 80 nm x 80 nm, V = +2.0 V. B) 40 nm x 40 nm, V = +2.0 V. Data courtesy of Xueying Zhao.
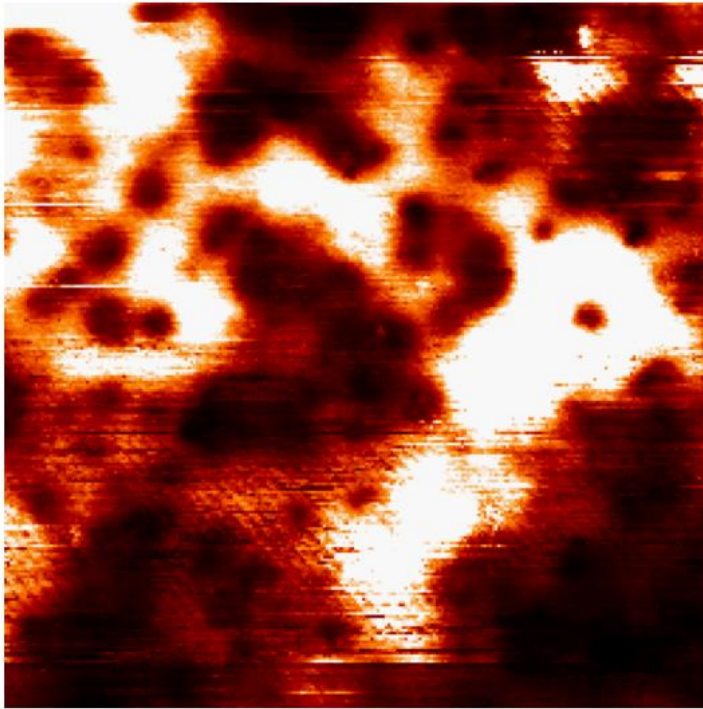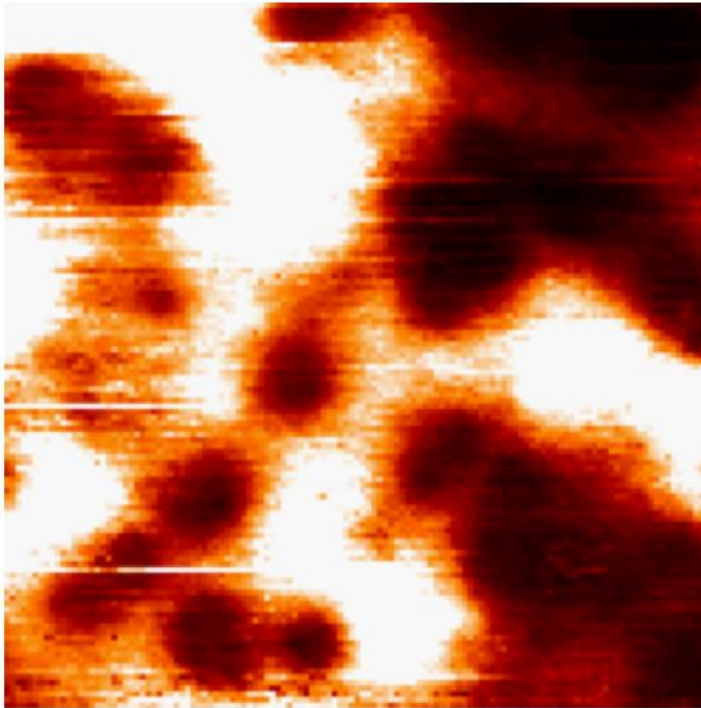
Figure 8-10. CAFM image of MoS_2 after 500 eV, 1 x 10^{13} cm^{-2}, F implant, and 15 minute, 550˚C, H_2S anneal. A) 80 nm x 80 nm, V = +2.5 V. B) 40 nm x 40 nm, V = +2.5 V. Data courtesy of Xueying Zhao.
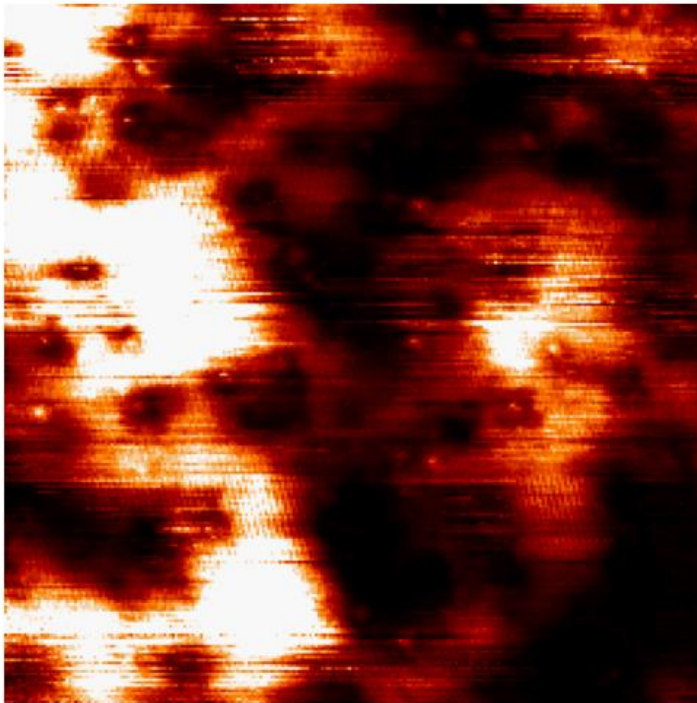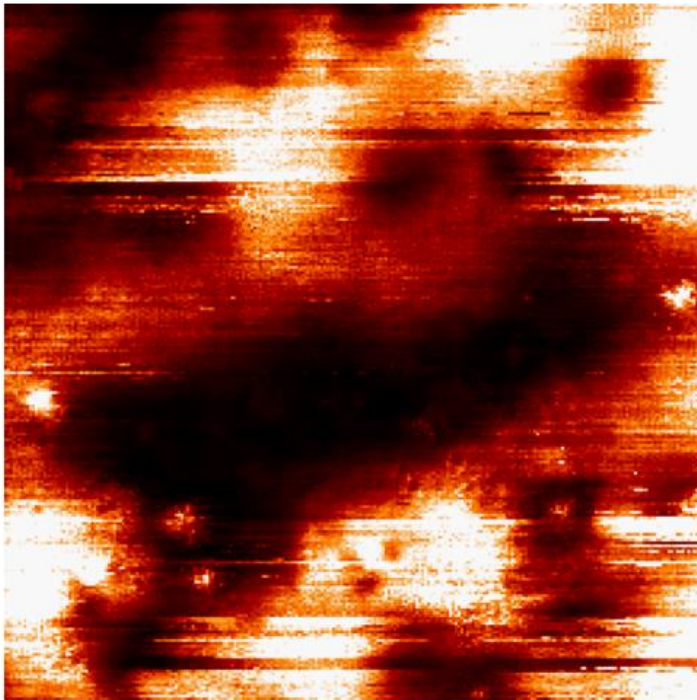
Figure 8-11. CAFM image of MoS$_2$ after 500 eV, 1 x 10^{13} cm^{-2}, F implant, and 15 minute, 800˚C, H$_2$S anneal. A) 80 nm x 80 nm, V = +0.8 V. B) 40 nm x 40 nm, V = +0.8 V. Data courtesy of Xueying Zhao.
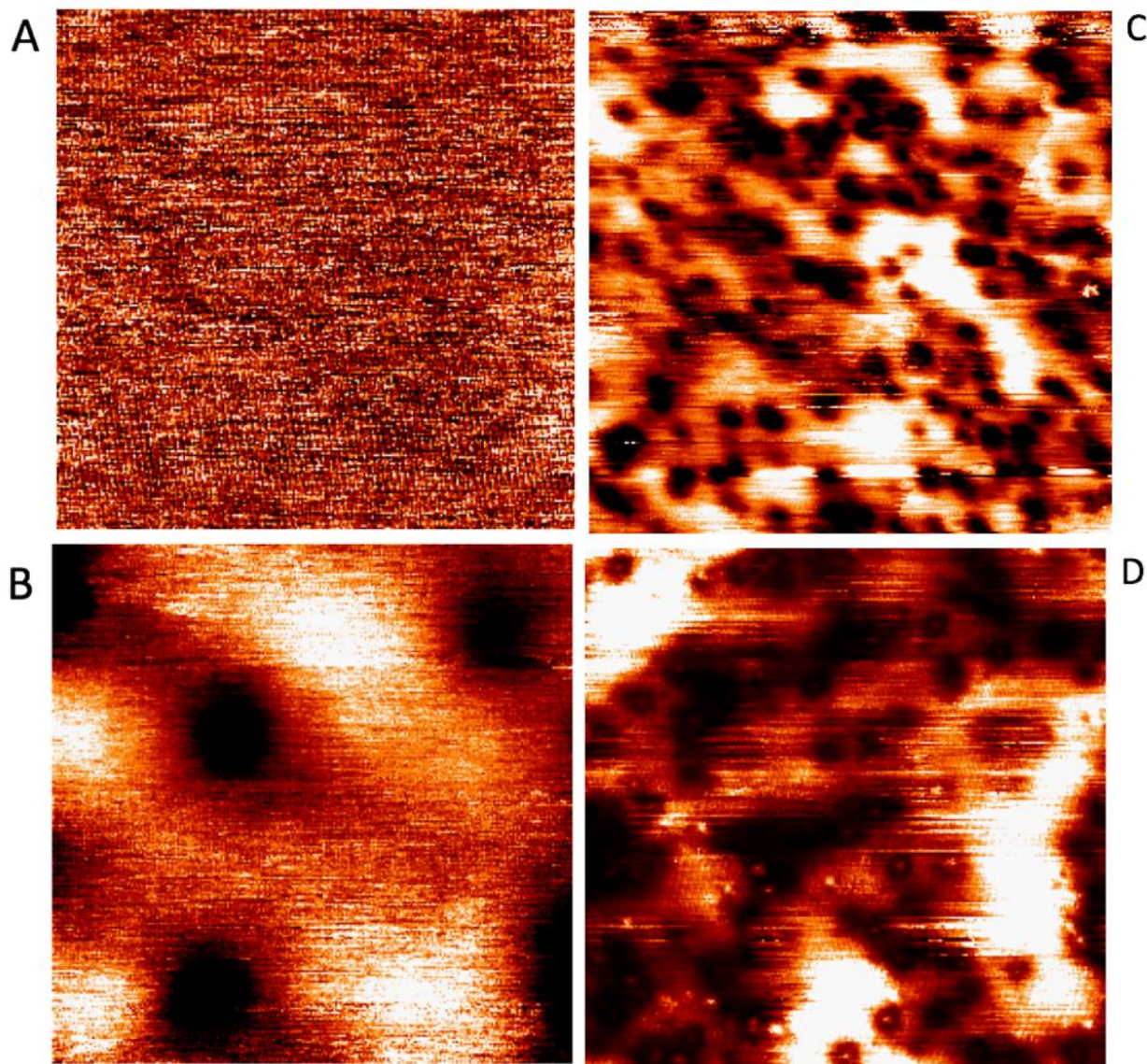
Figure 8-12. CAFM images of the MoS_2 surface. Side by side comparisons of the sample extrema that highlights an apparent enhancement of the defects after annealing, rather than a repair. A) Unimplanted, unannealed MoS_2. Region with no defects. B) Same material as in A), but in a region with defects present. C) As-implanted MoS_2 surface - 500 eV, 1 x 10^{13} cm^{-2}, fluorine. D) Implanted as in C, and annealed at 800˚C for 15 minutes in H_2S. Data courtesy of Xueying Zhao.
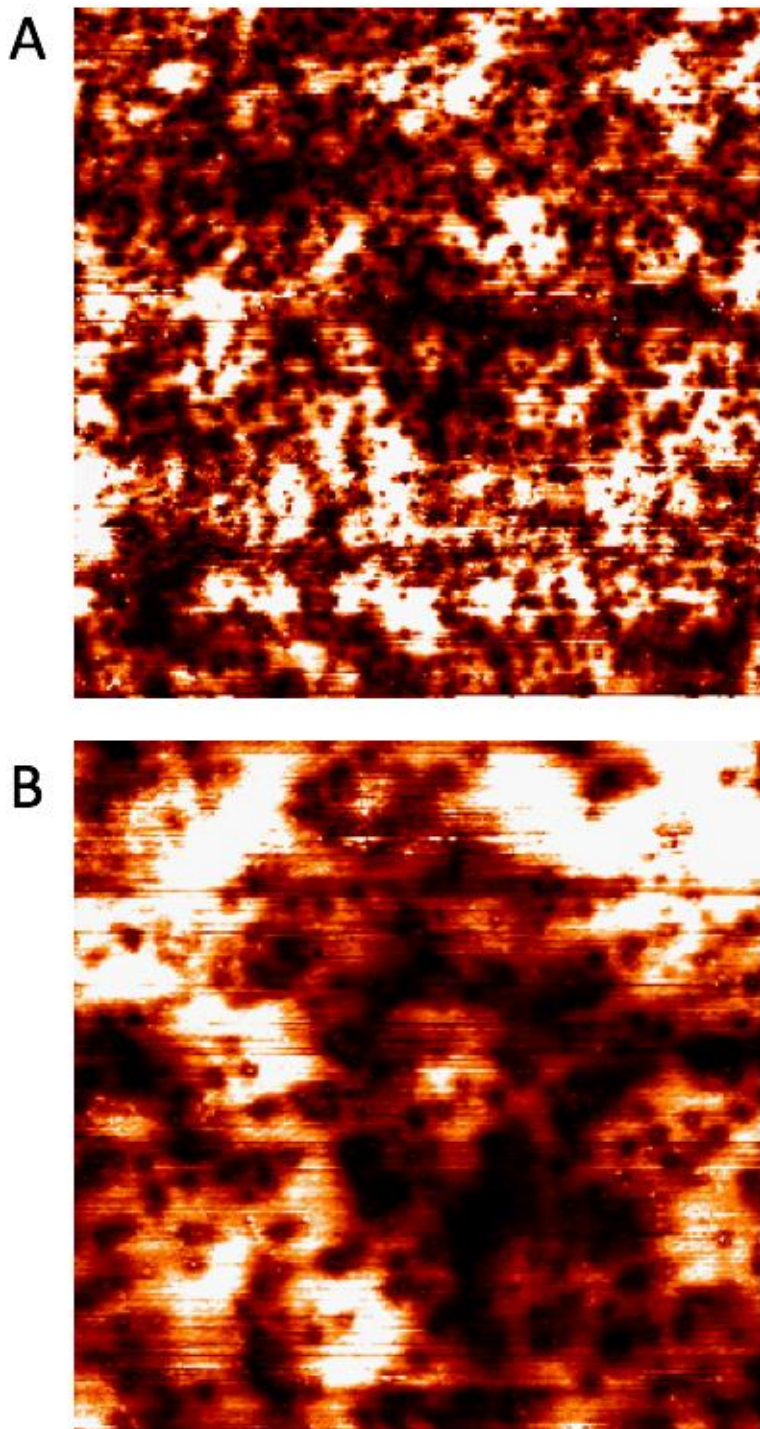
Figure 8-13. CAFM image of MoS$_2$ after 500 eV, 1 x 10^{13} cm^{-2}, F implant, and 15 minute, 800˚C, H$_2$S anneal. A) 400 nm x 400 nm, V = +1.0 V. B) 160 nm x 160 nm, V = +1.0 V. Data courtesy of Xueying Zhao.
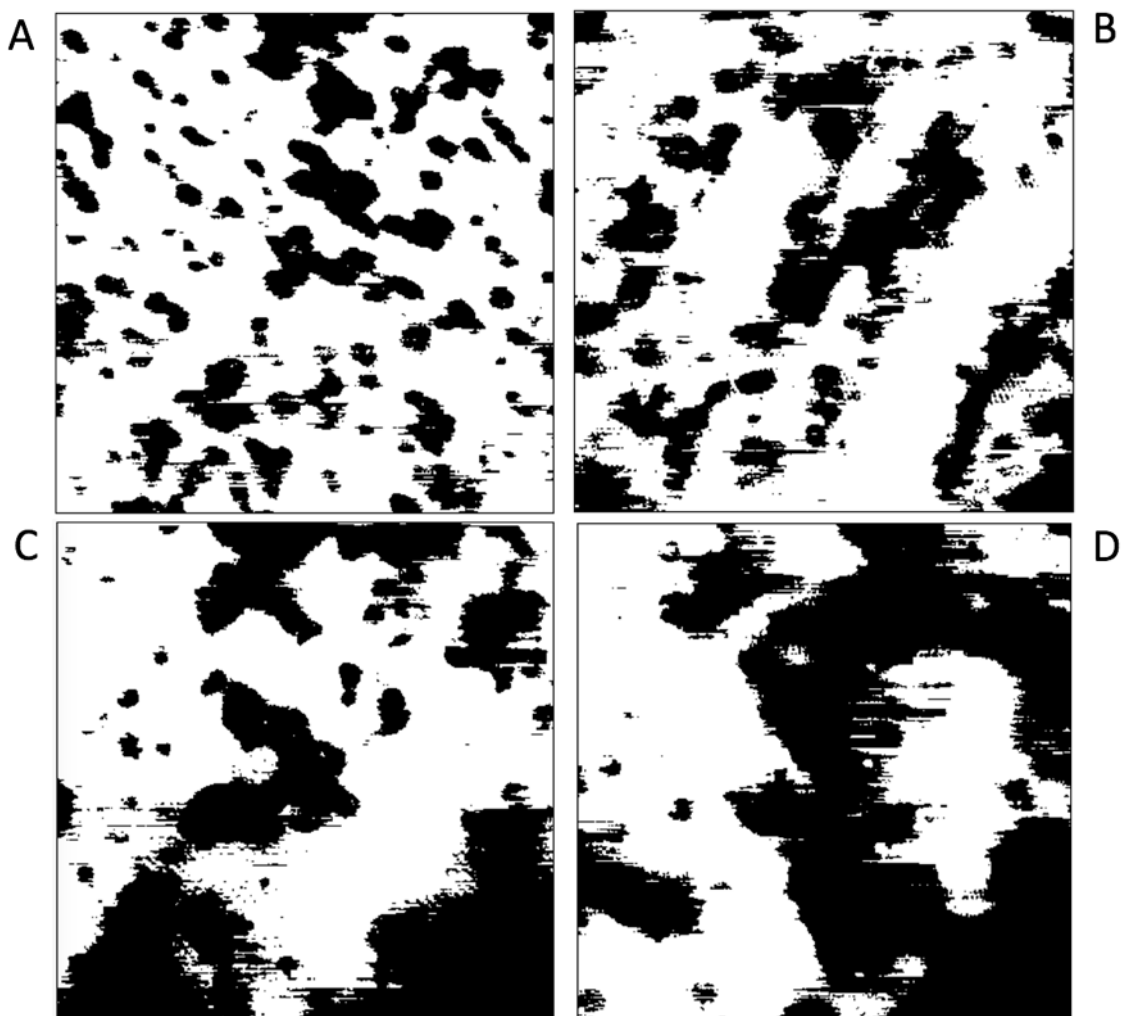
Figure 8-14. Black and white casting of initial images, used for quantifying defects. Original images were CAFM images of MoS_2 after 500 eV, 1 x 10^{13} cm^{-2}, F implant, and 15 minute, H_2S anneal. A) No anneal. B) 300˚C anneal. C) 550˚anneal. D) 800˚C anneal.
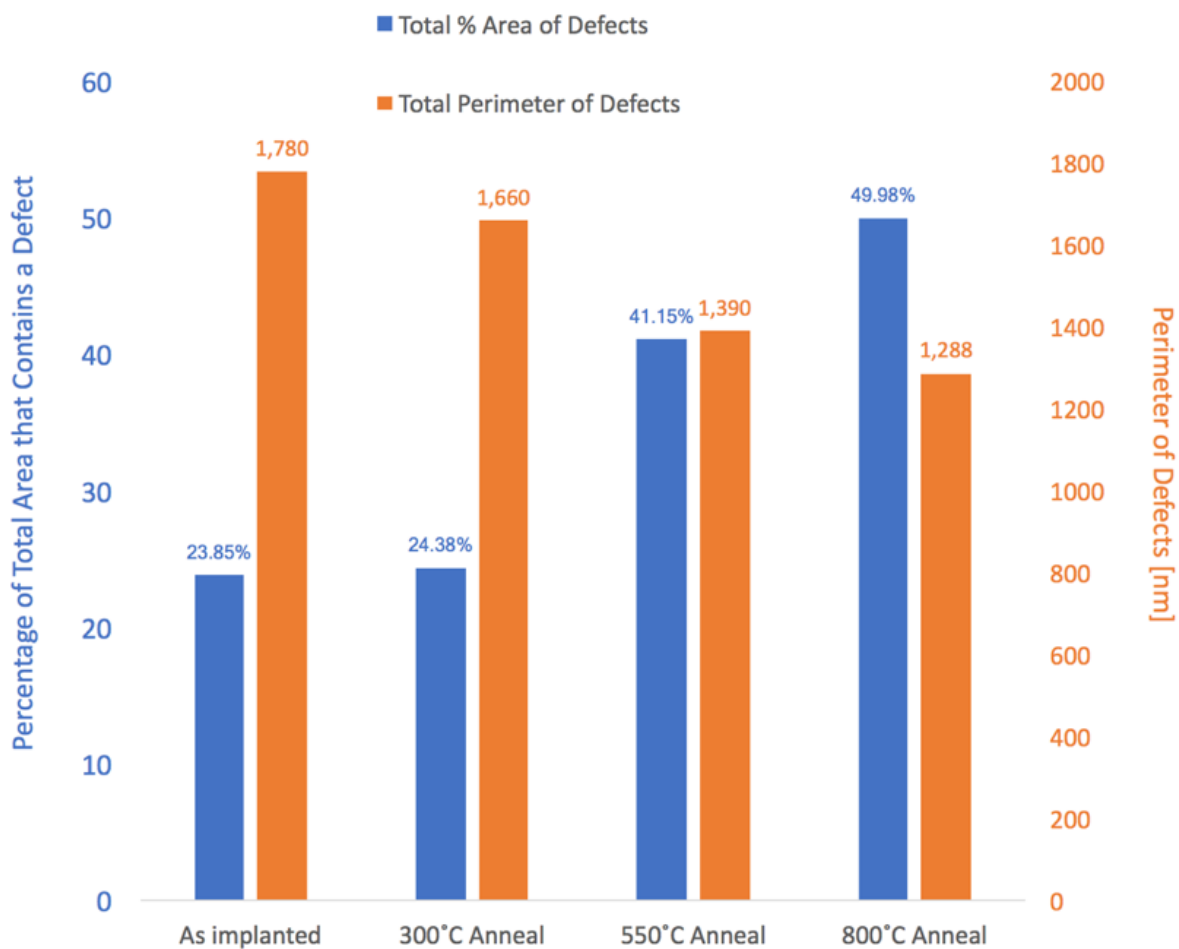
Figure 8-15. Analysis of black and white images in Figure 8-14 showing the total perimeter of defects and total percentage of defect area as a function of annealing temperature. The initial images covered an 80 x 80 nm^2 area. Samples were implanted with a 500 eV, 1 x 10^{13} cm^{-2} dose of F.
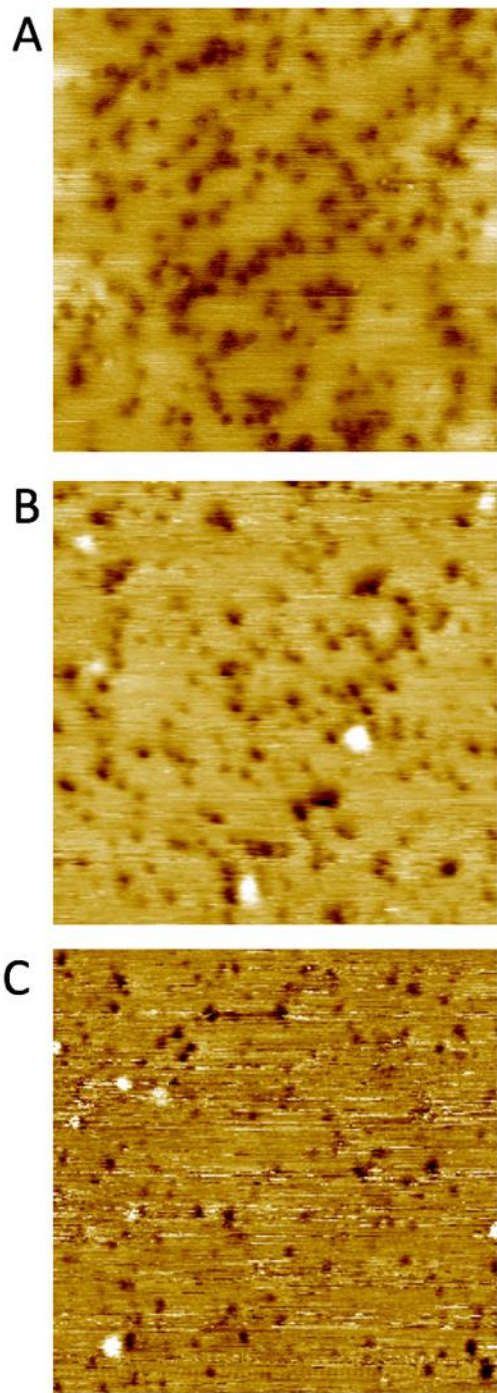
Figure 8-16. STM image of the MoS$_2$ surface after a 200 eV, 1 x 10^{13} cm^{-2} Cl implant, with anneals in vacuum (10^{-10} torr). No major changes observed with anneal. A) before anneal. B) 550˚C, 5 minute anneal. C) 750˚C anneal. Data courtesy of Xueying Zhao.

CHAPTER 9
CONCLUSIONS AND FUTURE WORK

Conclusions

Ion implantation did not prove to be an effective doping method for MoS_2, within the experimental parameters used. The low-energy 200 eV implants were not low enough and they damaged the MoS_2. The damage dominated the effect of ion implantation in MoS_2. Implanted MoS_2 was never repaired to its pre-implanted ability. Dopant activation was never detected. Implant damage increased with implanted dose.

Early experiments observed an anisotropic effect of implant damage. The out-of-plane response seemed beneficial, however, it never yielded a significant increase in current or reduction in contact resistance at the device-scale. The in-plane effect was clearly detrimental, and was never overcome by anneals. Some induced defects were observed to impair mobility, and be partially repaired by H_2S anneals at 800˚C. Other defects compensated carriers and were not repaired in H_2S anneals up to 800˚C. The origin of the unrepaired defects is unclear. The initial carrier compensation is often attributed to S-loss and Mo-cluster formation. However, MoS_2 is grown at the annealed temperature with Mo and H_2S, so Mo-cluster would be expected to form MoS_2 in the anneal.

The defects could be of a type that is not repaired in H_2S, such as a Mo vacancy. Or, the defect-repair process could require temperatures higher than 800˚C. Mo vacancies seem likely to be involved, however multiple defects are expected to contribute. Higher annealing temperatures cannot be explored for damage repair or dopant activation, due to the loss of the implanted species that was observed at

1000°C. If it's possible to repair damage and activate dopants without losing them, it would seem to occur at a narrow, precisely controlled thermal window.

The nature of these experiments complicates defect analysis. Defects feed off each other. They can increase and decrease the energy of formation, or mobility of other defects. Ion implantation induces defects, and defect mobility. The sulfur rich atmosphere of the anneal will favor uncommon reactions. The high temperature within the anneal feeds the other behaviors. These situations create a dynamic environment that is difficult to predict, especially for grown films, which have additional native defects.

These results find relevance for future 2DM electronics, even if the ion implantation didn't work. In fact, it's precisely because it didn't work. The results highlight the sensitivity of MoS_2 to irradiation. Other 2DMs likely behave similarly. This makes electronics made with 2DMs sensitive to phenomena such as single event upsets (SEU). In environments where irradiation can be expected, such as in the electronics or solar panels of a satellite or space craft, these results might preclude 2DMs from participation. Electronics with 2DMs will likely require additional radiation hardening steps.

Based on the results presented in this dissertation, and within the parameters of the presented experiments, ion implantation is not an effective method for doping MoS_2. The experiments only succeeded in damaging MoS_2, and partially repairing it. If ion implantation is ever going to succeed in effectively doping MoS_2, priority number one is to develop a method for repairing the implant damage, or preventing it in the first place.

Future Work

The anneals used in these experiments were for a relatively long time, 15 minutes. Spike anneals may provide the thermal energy required to activate dopants while preventing them from diffusing out of the MoS_2. It's also possible that pre-treating the MoS_2 in a manner that creates sulfur vacancies, prior to implantation, could encourage dopant substitution. Hydrogen plasma treatments have been used for similar results. Another unexplored option is lightly heating the sample during the implantation.

Perhaps the most promising future approach is with lower energy implants, even 0 eV "exposures". The 0 eV exposures can occur in a plasma chamber, preferably a remote chamber to minimize damage to the MoS_2. The plasma species will be ionized and will have a kinetic energy when they interact with the MoS_2, but it will likely be at a much lower energy than the implantations. In this way, the process is essentially a soft deposition of the dopant. Even then, new annealing schemes will likely need to be explored to minimize the chance for dopant out-diffusion while enabling substitution.

LIST OF REFERENCES

[1]   K. S. Novoselov, A. K. Geim, S. V. Morozov, D. Jiang, Y. Zhang, S. V. Dubonos, I. V. Grigorieva, and A. A. Firsov, "Electric Field Effect in Atomically Thin Carbon Films," *Science*, vol. 306, no. 5696, pp. 666–669, 2004.

[2]   A. Castellanos-Gomez, L. Vicarelli, and E. Prada, "Isolation and characterization of few-layer black phosphorus," *2D Materials*, vol. 1, 2014.

[3]   Y. Lin and J. W. Connell, "Advances in 2D boron nitride nanostructures: nanosheets, nanoribbons, nanomeshes, and hybrids with graphene," *Nanoscale*, vol. 4, no. 22, pp. 6908–33, 2012.

[4]   X. Duan, C. Wang, A. Pan, R. Yu, and X. Duan, "Two-dimensional transition metal dichalcogenides as atomically thin semiconductors: opportunities and challenges," *Chemical Society Reviews*, pp. 1–18, Oct. 2015.

[5]   R. G. Dickinson and L. Pauling, "The Crystal Structure of Molybdenite," *J. Am. Chem. Soc.*, vol. 45, no. 6, pp. 1466–1471, 1923.

[6]   I. Song, C. Park, and H. C. Choi, "Synthesis and properties of molybdenum disulphide: from bulk to atomic layers," *RSC Advances*, vol. 5, pp. 7495–7514, Dec. 2014.

[7]   J.-W. Jiang, "Graphene versus MoS_2: A short review," *Front. Phys.*, vol. 10, no. 3, pp. 287–302, Feb. 2015.

[8]   N. Izyumskaya, D. O. Demchenko, V. Avrutin, Ü. Özgür, And H. Morkoç, "Two-dimensional MoS_2 as a new material for electronic devices," *Turk J Phys*, vol. 38, pp. 478–496, 2014.

[9]   W. Liu, J. Kang, W. Cao, and D. Sarkar, "High-Performance Few-Layer-MoS_2 Field-Effect-Transistor with Record Low Contact-Resistance," presented at the IEDM, 2013, pp. 19.4.1–19.4.4.

[10]   M.-W. Lin, I. I. Kravchenko, J. Fowlkes, X. Li, A. A. Puretzky, C. M. Rouleau, D. B. Geohegan, and K. Xiao, "Thickness-dependent charge transport in few-layer MoS_2 field-effect transistors," *Nanotechnology*, vol. 27, no. 16, pp. 165203–8, Mar. 2016.

[11]   G. W. Neudeck and R. F. Pierret, *Advanced Semiconductor Fundamentals*, Second. vol. VI. Pearson Education, Inc, 2003.

[12]   G. E. Moore, "Cramming more components onto integrated circuits," *Electronics*, vol. 38, Electronics Magazine, pp. 114–117, 19-Apr-1965.

[13]   T. N. Theis and H. Wong, "The End of Moore's Law: A New Beginning for Information Technology," *Computing in Science & Engineering*, vol. 19, no. 2, pp. 41–50, 2017.

[14]   *International Technology Working Groups.* [Online]. Available: http://www.itrs2.net/itrs-reports.html. [Accessed: 10-Jun-2017].

[15]   S. S. Sylvia, H.-H. Park, M. A. Khayer, K. Alam, G. Klimeck, and R. K. Lake, "Material Selection for Minimizing Direct Tunneling in Nanowire Transistors," *IEEE Trans. Electron Devices*, vol. 59, no. 8, pp. 2064–2069, Jul. 2012.

[16]   K. P. Cheung, "On the 60 mV/dec @300 K limit for MOSFET subthreshold swing," presented at the Proceedings of 2010 International Symposium on VLSI Technology, System and Application IS -, 2010, pp. 72–73.

[17]   M. Luisier, M. Lundstrom, D. A. Antoniadis, and J. Bokor, "Ultimate device scaling: Intrinsic performance comparisons of carbon-based, InGaAs, and Si field-effect transistors for 5 nm gate length," presented at the 2011 International Electron Devices Meeting IS -, 2011, pp. 11.2.1–11.2.4.

[18]   K. Suzuki, T. Tanaka, Y. Tosaka, H. Horie, and Y. Arimoto, "Scaling theory for double-gate SOI MOSFET's," *IEEE Trans. Electron Devices*, vol. 40, no. 12, pp. 2326–2329, Dec. 1993.

[19]   W.-S. Cho and K. Roy, "The Effects of Direct Source-to-Drain Tunneling and Variation in the Body Thickness on (100) and (110) Sub-10-nm Si Double-Gate Transistors," *IEEE Electron Device Lett.*, vol. 36, no. 5, pp. 427–429, Apr. 2015.

[20]   D. Wickramaratne, F. Zahid, and R. K. Lake, "Electronic and thermoelectric properties of few-layer transition metal dichalcogenides," *The Journal of Chemical Physics*, vol. 140, no. 12, pp. 124710–14, Mar. 2014.

[21]   H. D. Barber, "Effective mass and intrinsic concentration in silicon," *Solid State Electronics*, vol. 10, no. 11, pp. 1039–1051, 1967.

[22]   K. Alam and R. K. Lake, "Monolayer MoS_2 Transistors Beyond the Technology Road Map," *IEEE Trans. Electron Devices*, vol. 59, no. 12, pp. 3250–3254, Mar. 2015.

[23]   Y. Yoon, K. Ganapathi, and S. Salahuddin, "How Good Can Monolayer MoS_2 Transistors Be?" *Nano Lett.*, vol. 11, no. 9, pp. 3768–3773, Sep. 2011.

[24]   B. Radisavljevic, A. Radenovic, J. Brivio, V. Giacometti, and A. Kis, "Single-layer MoS_2 transistors," pp. 1–5, Feb. 2015.

[25]   Y. Liu, J. Guo, Y. Wu, E. Zhu, N. O. Weiss, Q. He, H. Wu, H.-C. Cheng, Y. Xu, I. Shakir, Y. Huang, and X. Duan, "Pushing the Performance Limit of Sub-100 nm Molybdenum Disulfide Transistors," *Nano Lett.*, vol. 16, no. 10, pp. 6337–6342, Oct. 2016.

[26]   J. Pu, Y. Yomogida, K.-K. Liu, L.-J. Li, Y. Iwasa, and T. Takenobu, "Highly Flexible MoS_2 Thin-Film Transistors with Ion Gel Dielectrics," *Nano Lett.*, vol. 12, no. 8, pp. 4013–4017, Aug. 2012.

[27]   R. Cheng, D. Li, H. Zhou, C. Wang, A. Yin, S. Jiang, Y. Liu, Y. Chen, Y. Huang, and X. Duan, "Electroluminescence and Photocurrent Generation from Atomically Sharp WSe_2/MoS_2 Heterojunction p-n Diodes," *Nano Lett.*, vol. 14, no. 10, pp. 5590–5597, Oct. 2014.

[28]   C. Gong, H. Zhang, W. Wang, and L. Colombo, "Band alignment of two-dimensional transition metal dichalcogenides: Application in tunnel field effect transistors," *Applied Physics Letters*, 2013.

[29]   H. Liu, A. T. Neal, and P. D. Ye, "Channel Length Scaling of MoS_2 MOSFETs," *ACS Nano*, vol. 6, no. 10, pp. 8563–8569, Oct. 2012.

[30]   J. Kang, W. Liu, and K. Banerjee, "High-performance MoS_2 transistors with low-resistance molybdenum contacts," *Appl. Phys. Lett.*, vol. 104, no. 9, pp. 093106–6, Mar. 2014.

[31]   I. R. committee, "International Technology Roadmap For Semiconductors 2.0, 2015 Edition," Jun. 2016.

[32]   C. Gong, L. Colombo, R. M. Wallace, and K. Cho, "The Unusual Mechanism of Partial Fermi Level Pinning at Metal–MoS_2 Interfaces," *Nano Lett.*, vol. 14, no. 4, pp. 1714–1720, Apr. 2014.

[33]   S. Das, H.-Y. Chen, A. V. Penumatcha, and J. Appenzeller, "High Performance Multilayer MoS_2 Transistors with Scandium Contacts," *Nano Lett.*, vol. 13, no. 1, pp. 100–105, Jan. 2013.

[34]   W. Park, Y. Kim, S. K. Lee, U. Jung, and J. H. Yang, "Contact resistance reduction using Fermi level de-pinning layer for MoS_2 FETs," *… (IEDM)*, pp. 5.1.1–5.1.4, 2014.

[35]   N. Kaushik, D. Karmakar, A. Nipane, S. Karande, and S. Lodha, "Interfacial n-Doping Using an Ultrathin TiO_2 Layer for Contact Resistance Reduction in MoS_2," *ACS Appl. Mater. Interfaces*, vol. 8, no. 1, pp. 256–263, Jan. 2016.

[36]   F. Wypych and R. Sch llhorn, "1T-MoS_2, a new metallic modification of molybdenum disulfide," *J. Chem. Soc., Chem. Commun.*, vol. 21, no. 19, pp. 1386–1388, 1992.

[37]   R. Kappera, D. Voiry, S. E. Yalcin, W. Jen, M. Acerce, S. Torrel, B. Branch, S. Lei, W. Chen, S. Najmaei, J. Lou, P. M. Ajayan, G. Gupta, A. D. Mohite, and M. Chhowalla, "Metallic 1T phase source/drain electrodes for field effect transistors from chemical vapor deposited MoS_2," *APL Materials*, vol. 2, no. 9, pp. 092516–7, Sep. 2014.

[38]   J. Suh, T.-E. Park, D.-Y. Lin, D. Fu, J. Park, H. J. Jung, Y. Chen, C. Ko, C. Jang, Y. Sun, R. Sinclair, J. Chang, S. Tongay, and J. Wu, "Doping against the Native Propensity of MoS_2: Degenerate Hole Doping by Cation Substitution," *Nano Lett.*, vol. 14, no. 12, pp. 6976–6982, Dec. 2014.

[39]   C. J. Lockhart de la Rosa, A. Nourbakhsh, M. Heyne, I. Asselberghs, C. Huyghebaert, I. Radu, M. Heyns, and S. De Gendt, "Highly efficient and stable MoS_2 FETs with reversible n-doping using a dehydrated poly(vinyl-alcohol) coating," *Nanoscale*, vol. 9, no. 1, pp. 258–265, 2017.

[40]   Y. Du, H. Liu, A. T. Neal, M. Si, and P. D. Ye, "Molecular Doping of Multilayer MoS_2 Field-Effect Transistors: Reduction in Sheet and Contact Resistances," *IEEE Electron Device Lett.*, vol. 34, no. 10, pp. 1328–1330, Nov. 2015.

[41]   D. Kiriya, M. Tosun, P. Zhao, J. S. Kang, and A. Javey, "Air-Stable Surface Charge Transfer Doping of MoS_2 by Benzyl Viologen," *J. Am. Chem. Soc.*, vol. 136, no. 22, pp. 7853–7856, Jun. 2014.

[42]   L. Yang, K. Majumdar, H. Liu, Y. Du, H. Wu, M. Hatzistergos, P. Y. Hung, R. Tieckelmann, W. Tsai, C. Hobbs, and P. D. Ye, "Chloride Molecular Doping Technique on 2D Materials: WS_2 and MoS_2," *Nano Lett.*, vol. 14, no. 11, pp. 6275–6280, Nov. 2014.

[43]   M. P. Seah, "A review of the analysis of surfaces and thin films by AES and XPS," *Vacuum*, vol. 34, no. 3, pp. 463–478, 1984.

[44]   C. D. Wagner, "NIST x-ray photoelectron spectroscopy (XPS) database," National Bureau of Standards, Gaithersburg, MD, 1990.

[45]   C. R. Brundle and A. D. Baker, *Electron spectroscopy*, vol. 2. Academic Press, 1978.

[46]   G. Greczynski and L. Hultman, "C 1s Peak of Adventitious Carbon Aligns to the Vacuum Level: Dire Consequences for Material's Bonding Assignment by Photoelectron Spectroscopy," *ChemPhysChem*, vol. 110, pp. 776–7, Apr. 2017.

[47]   Q. Ma, P. M. Odenthal, J. Mann, D. Le, C. S. Wang, Y. Zhu, T. Chen, D. Sun, K. Yamaguchi, T. Tran, M. Wurch, J. L. McKinley, J. Wyrick, K. Magnone, T. F. Heinz, T. S. Rahman, R. Kawakami, and L. Bartels, "Controlled argon beam-induced desulfurization of monolayer molybdenum disulfide," *J. Phys.: Condens. Matter*, vol. 25, no. 25, pp. 252201–6, May 2013.

[48]   D. Ganta, S. Sinha, and R. T. Haasch, "2-D Material Molybdenum Disulfide Analyzed by XPS," *Surface Science Spectra*, vol. 21, no. 1, pp. 19–27, Dec. 2014.

[49]   I. S. Kim, V. K. Sangwan, D. Jariwala, J. D. Wood, S. Park, K.-S. Chen, F. Shi, F. Ruiz-Zepeda, A. Ponce, M. Jose-Yacaman, V. P. Dravid, T. J. Marks, M. C. Hersam, and L. J. Lauhon, "Influence of Stoichiometry on the Optical and Electrical Properties of Chemical Vapor Deposition Derived MoS_2," *ACS Nano*, vol. 8, no. 10, pp. 10551–10558, Oct. 2014.

[50]   A. Tarasov, S. Zhang, M.-Y. Tsai, P. M. Campbell, S. Graham, S. Barlow, S. R. Marder, and E. M. Vogel, "Controlled Doping of Large-Area Trilayer MoS_2 with Molecular Reductants and Oxidants," *Adv. Mater.*, vol. 27, no. 7, pp. 1175–1181, Jan. 2015.

[51]   E. Smith and G. Dent, *Modern Raman Spectroscopy a practical approach*. John Wiley & Sons Ltd, 2005.

[52]   H. Li, Q. Zhang, C. C. R. Yap, B. K. Tay, T. H. T. Edwin, A. Olivier, and D. Baillargeat, "From Bulk to Monolayer MoS_2: Evolution of Raman Scattering," *Adv. Funct. Mater.*, vol. 22, no. 7, pp. 1385–1390, Jan. 2012.

[53]   M. R. Laskar, L. Ma, S. Kannappan, P. Sung Park, S. Krishnamoorthy, D. N. Nath, W. Lu, Y. Wu, and S. Rajan, "Large area single crystal (0001) oriented MoS_2," *Appl. Phys. Lett.*, vol. 102, no. 25, pp. 252108–6, Jun. 2013.

[54]   A. Nipane, D. Karmakar, N. Kaushik, S. Karande, and S. Lodha, "Few-Layer MoS_2 p-Type Devices Enabled by Selective Doping Using Low Energy Phosphorus Implantation," *ACS Nano*, vol. 10, no. 2, pp. 2128–2137, Feb. 2016.

[55]   J. R. Lakowicz, *Principles of Fluorescence Spectroscopy.*, Third. Springer Science+Business Media, LLC, 2006.

[56]   G. Bemski, "Recombination Properties of Gold in Silicon," *Phys. Rev.*, vol. 111, no. 6, pp. 1515–1518, Sep. 1958.

[57]   A. Splendiani, L. Sun, Y. Zhang, T. Li, J. Kim, C.-Y. Chim, G. Galli, and F. Wang, "Emerging Photoluminescence in Monolayer MoS_2," *Nano Lett.*, vol. 10, no. 4, pp. 1271–1275, Apr. 2010.

[58]   K. F. Mak, C. Lee, J. Hone, J. Shan, and T. F. Heinz, "Atomically Thin MoS2: A New Direct-Gap Semiconductor," *Phys. Rev. Lett.*, vol. 105, no. 13, pp. 136805–4, Sep. 2010.

[59]   Y. Guo, Y. Han, J. Li, A. Xiang, X. Wei, S. Gao, and Q. Chen, "Study on the Resistance Distribution at the Contact between Molybdenum Disulfide and Metals," *ACS Nano*, vol. 8, no. 8, pp. 7771–7779, Aug. 2014.

[60]   D. Curran-Everett, "Explorations in statistics: standard deviations and standard errors," *AJP: Advances in Physiology Education*, vol. 32, no. 3, pp. 203–208, Sep. 2008.

[61]   P. Barde and M. Barde, "What to use to express the variability of data: Standard deviation or standard error of mean?," *Perspect Clin Res*, vol. 3, no. 3, pp. 113–4, 2012.

[62]   A. A. Firsov, Y. Zhang, and K. S. Novoselov, "Electric field effect in atomically thin carbon films.," *Science*, 2004.

[63]   M. Yi and Z. Shen, "A review on mechanical exfoliation for the scalable production of graphene," *Journal of Materials Chemistry A: Materials for energy and sustainability*, vol. 3, pp. 11700–11715, May 2015.

[64]   X. Gu, B. Li, and R. Yang, "Layer thickness-dependent phonon properties and thermal conductivity of MoS_2," *Journal of Applied Physics*, vol. 119, no. 8, pp. 085106–9, Feb. 2016.

[65]   Y. P. Venkata Subbaiah, K. J. Saji, and A. Tiwari, "Atomically Thin MoS_2: A Versatile Nongraphene 2D Material," *Adv. Funct. Mater.*, vol. 26, no. 13, pp. 2046–2069, Feb. 2016.

[66]   J. Hong, C. Lee, J.-S. Park, and J. H. Shim, "Control of valley degeneracy in MoS_2 by layer thickness and electric field and its effect on thermoelectric properties," *Phys. Rev. B*, vol. 93, no. 3, pp. 035445–6, Jan. 2016.

[67]   M. M. Benameur, B. Radisavljevic, J. S. Héron, S. Sahoo, H. Berger, and A. Kis, "Visibility of dichalcogenide nanolayers," *Nanotechnology*, vol. 22, no. 12, pp. 125706–6, Feb. 2011.

[68]   H. Li, J. Wu, X. Huang, G. Lu, J. Yang, X. Lu, Q. Xiong, and H. Zhang, "Rapid and Reliable Thickness Identification of Two-Dimensional Nanosheets Using Optical Microscopy," *ACS Nano*, vol. 7, no. 11, pp. 10344–10353, Nov. 2013.

[69]   D. Chiappe, I. Asselberghs, S. Sutar, S. Iacovo, V. Afanas'ev, A. Stesmans, Y. Balaji, L. Peters, M. Heyne, M. Mannarino, W. Vandervorst, S. Sayan, C. Huyghebaert, M. Caymax, M. Heyns, S. De Gendt, I. Radu, and A. Thean, "Controlled Sulfurization Process for the Synthesis of Large Area MoS_2 Films and MoS_2/WS_2 Heterostructures," *Adv. Mater. Interfaces*, vol. 3, no. 4, pp. 1500635–10, Dec. 2015.

[70]   A. Gurarslan, Y. Yu, L. Su, Y. Yu, F. Suarez, S. Yao, Y. Zhu, M. Ozturk, Y. Zhang, and L. Cao, "Surface-Energy-Assisted Perfect Transfer of Centimeter-Scale Monolayer and Few-Layer MoS_2 Films onto Arbitrary Substrates," *ACS Nano*, vol. 8, no. 11, pp. 11522–11528, Nov. 2014.

[71]   A. Stesmans, S. Iacovo, D. Chiappe, I. Radu, C. Huyghebaert, S. De Gendt, and V. V. Afanas'ev, "Paramagnetic Intrinsic Defects in Polycrystalline Large-Area 2D MoS_2 Films Grown on SiO_2 by Mo Sulfurization," pp. 1–5, Apr. 2017.

[72]   K. Kaasbjerg, K. S. Thygesen, and K. W. Jacobsen, "Phonon-limited mobility in n-type single-layer MoS_2 from first principles," *Phys. Rev. B*, vol. 85, no. 11, pp. 232405–16, Mar. 2012.

[73]   A. Pezeshki, S. H. H. Shokouh, S. R. A. Raza, J. S. Kim, S.-W. Min, I. Shackery, S. C. Jun, and S. Im, "Top and back gate molybdenum disulfide transistors coupled for logic and photo-inverter operation," *Journal of Materials Chemistry C: Materials for optical and electronic devices*, vol. 2, pp. 8023–8028, Sep. 2014.

[74]   L. Yang, K. Majumdar, Y. Du, H. Liu, and H. Wu, "High-performance MoS_2 field-effect transistors enabled by chloride doping: Record low contact resistance (0.5 kΩ· μm) and record high drain current (460 μA/μm)," 2014, pp. 1–2.

[75]   D. Jena and A. Konar, "Enhancement of Carrier Mobility in Semiconductor Nanostructures by Dielectric Engineering," *Phys. Rev. Lett.*, vol. 98, no. 13, pp. 136805–4, Mar. 2007.

[76]   N. Ma and D. Jena, "Charge Scattering and Mobility in Atomically Thin Semiconductors," *Phys. Rev. X*, vol. 4, no. 1, pp. 011043–9, Mar. 2014.

[77]   Z. Yu, Z.-Y. Ong, Y. Pan, Y. Cui, R. Xin, Y. Shi, B. Wang, Y. Wu, T. Chen, Y.-W. Zhang, G. Zhang, and X. Wang, "Realization of Room-Temperature Phonon-Limited Carrier Transport in Monolayer MoS_2 by Dielectric and Carrier Screening," *Adv. Mater.*, vol. 28, no. 3, pp. 547–552, Nov. 2015.

[78]   Q. Yue, Z. Shao, S. Chang, and J. Li, "Adsorption of gas molecules on monolayer MoS_2 and effect of applied electric field," *Nanoscale Res Lett*, vol. 8, no. 1, pp. 425–7, 2013.

[79]   R. Sundaresan, D. E. Burk, and J. G. Fossum, "Potential improvement of polysilicon solar cells by grain boundary and intragrain diffusion of aluminum," *Journal of Applied Physics*, vol. 55, no. 4, pp. 1162–1167, Feb. 1984.

[80]   M. Kittler, W. Seifert, M. Stemmer, and J. Palm, "Interaction of iron with a grain boundary in boron-doped multicrystalline silicon," *Journal of Applied Physics*, vol. 77, no. 8, pp. 3725–3728, Apr. 1995.

[81]   B. A. Pint and K. B. Alexander, "Grain Boundary Segregation of Cation Dopants," *Journal of the Electrochemical Society*, 1998.

[82]   N. Sahu, B. Parija, and S. Panigrahi, "Fundamental understanding and modeling of spin coating process: A review," *Indian J Phys*, vol. 83, no. 4, pp. 493–502, 2009.

[83]   M. Bruel, B. Aspar, and J. Aubertob-Herve, "Smart-Cut: a new silicon on insulator material technology based on hydrogen implantation and wafer bonding," *Jpn. J. Appl. Phys.*, vol. 36, pp. 1636–1641, 1997.

[84]   O. Lehtinen, E. Dumur, J. Kotakoski, A. V. Krasheninnikov, K. Nordlund, and J. Keinonen, "Production of defects in hexagonal boron nitride monolayer under ion irradiation," *Nuclear Inst. and Methods in Physics Research, B*, vol. 269, no. 11, pp. 1327–1331, Jun. 2011.

[85]   G. S. Was, "The Displacement of Atoms," in *Fundamentals of Radiation Materials Science*, vol. 18, no. 6, New York, NY: Springer New York, 2016, pp. 77–130.

[86]   A. V. Krasheninnikov and K. Nordlund, "Ion and electron irradiation-induced effects in nanostructured materials," *Journal of Applied Physics*, vol. 107, no. 7, pp. 071301–71, Apr. 2010.

[87]   Z. Bai, L. Zhang, and L. Liu, "Bombarding Graphene with Oxygen Ions: Combining Effects of Incident Angle and Ion Energy To Control Defect Generation," *J. Phys. Chem. C*, vol. 119, no. 47, pp. 26793–26802, Nov. 2015.

[88]   O. Lehtinen, J. Kotakoski, A. V. Krasheninnikov, A. Tolvanen, K. Nordlund, and J. Keinonen, "Effects of ion bombardment on a two-dimensional target: Atomistic simulations of graphene irradiation," *Phys. Rev. B*, vol. 81, no. 15, pp. 153401–4, Apr. 2010.

[89]   J. A. V. Pomoell, A. V. Krasheninnikov, K. Nordlund, and J. Keinonen, "Ion ranges and irradiation-induced defects in multiwalled carbon nanotubes," *Journal of Applied Physics*, vol. 96, no. 5, pp. 2864–2871, Sep. 2004.

[90]   N. F. Mott, "The scattering of fast electrons by atomic nuclei," presented at the Proceedings of the Royal Society of London Series A, 1929.

[91]   J. William A McKinley and H. Feshbach, "The Coulomb Scattering of Relativistic Electrons by Nuclei," *Phys. Rev.*, vol. 74, no. 12, pp. 1759–1763, Dec. 1948.

[92]   J. Hu, G. M. Vanacore, A. Cepellotti, N. Marzari, and A. H. Zewail, "Rippling ultrafast dynamics of suspended 2D monolayers, graphene," *Proc Natl Acad Sci USA*, vol. 113, no. 43, pp. E6555–E6561, Oct. 2016.

[93]   H.-P. Komsa and A. V. Krasheninnikov, "Native defects in bulk and monolayer MoS_2 from first principles," *Phys. Rev. B*, vol. 91, no. 12, pp. 125304–17, Mar. 2015.

[94]   A. Carvalho and A. H. C. Neto, "Donor and acceptor levels in semiconducting transition-metal dichalcogenides," *Phys. Rev. B*, vol. 89, no. 8, pp. 081406–5, Feb. 2014.

[95]   J. F. Ziegler, M. D. Ziegler, and J. P. Biersack, "SRIM – The Stopping and Range of Ions in Matter (2010)," *Nuclear Inst. and Methods in Physics Research, B*, vol. 268, no. 11, pp. 1818–1823, Jun. 2010.

[96]   Z. Y. Zhao, D. Hendrix, L. Y. Wu, and B. K. Cusson, "Ion Implantation Angle Variation to Device Performance and the Control in Production," *AIP Conference Proceedings*, vol. 680, no. 1, pp. 666–669, 2003.

[97]   F. L. Deepak, H. Cohen, S. Cohen, Y. Feldman, R. Popovitz-Biro, D. Azulay, O. Millo, and R. Tenne, "Fullerene-Like (IF) $Nb_xMo_{1-x}S_2$ Nanoparticles," *J. Am. Chem. Soc.*, vol. 129, no. 41, pp. 12549–12562, Oct. 2007.

[98]   M. A. Baker, R. Gilmore, C. Lenardi, and W. Gissler, "XPS Investigation of Preferential Sputtering of S from MoS_2 and Determination of MoS_x Stoichiometry from Mo And S Peak Positions," *Applied Surface Science*, vol. 150, no. 1, pp. 255–262, 1999.

[99]   J. R. Lince, D. J. Carré, and P. D. Fleischauer, "Effects of Argon Ion Bombardment on the Basal Plane Surface of MoS_2," *Langmuir*, vol. 2, 1986.

[100]   N. S. McIntyre, P. A. Spevack, G. Beamson, and D. Briggs, "Effects of Argon Ion Bombardment on Basal Plane and Polycrystalline MoS_2," *Surface Science*, vol. 237, no. 1, pp. L390–L397, 1990.

[101]   J. R. Lince, D. J. Carré, and P. D. Fleischauer, "Schottky-barrier formation on a covalent semiconductor without Fermi-level pinning: The metal-MoS_2(0001) interface," *Phys. Rev. B*, vol. 36, no. 3, pp. 1647–1656, Jul. 1987.

[102]   S. McDonnell, R. Addou, C. Buie, R. M. Wallace, and C. L. Hinkle, "Defect-Dominated Doping and Contact Resistance in MoS_2," *ACS Nano*, vol. 8, no. 3, pp. 2880–2888, Mar. 2014.

[103]   A. Inoue, T. Komori, and K.-I. Shudo, "Atomic-scale structures and electronic states of defects on Ar+-ion irradiated MoS_2," *Journal of Electron Spectroscopy and Related Phenomena*, vol. 189, pp. 11–18, Aug. 2013.

[104]   P. Bampoulis, R. van Bremen, Q. Yao, B. Poelsema, H. J. W. Zandvliet, and K. Sotthewes, "Defect Dominated Charge Transport and Fermi Level Pinning in MoS_2/Metal Contacts," *ACS Appl. Mater. Interfaces*, vol. 9, no. 22, pp. 19278–19286, May 2017.

[105]   J. B. Park, C. B. France, and B. A. Parkinson, "Scanning tunneling microscopy investigation of nanostructures produced by Ar +and He + bombardment of MoS_2 surfaces," *J. Vac. Sci. Technol. B*, vol. 23, no. 4, pp. 1532–12, 2005.

[106]   D. M. Sim, M. Kim, S. Yim, M.-J. Choi, J. Choi, S. Yoo, and Y. S. Jung, "Controlled Doping of Vacancy-Containing Few-Layer MoS_2 via Highly Stable Thiol-Based Molecular Chemisorption," *ACS Nano*, vol. 9, no. 12, pp. 12115–12123, Dec. 2015.

[107]   S. Das and J. Appenzeller, "Where Does the Current Flow in Two-Dimensional Layered Systems?," *Nano Lett.*, vol. 13, no. 7, pp. 3396–3402, Jul. 2013.

[108]   J. Wu, H. Li, Z. Yin, H. Li, J. Liu, X. Cao, Q. Zhang, and H. Zhang, "Layer Thinning and Etching of Mechanically Exfoliated MoS_2 Nanosheets by Thermal Annealing in Air," *Small*, vol. 321, pp. n/a–n/a, Aug. 2013.

[109]   R. K. Tiwari, J. Yang, M. Saeys, and C. Joachim, "Surface reconstruction of MoS_2 to Mo_2S_3," *Surface Science*, 2008.

[110]   M. Lee and M. C. Wu, "3D silicon transformation using hydrogen annealing," *Proc Solid-State Sens*, 2004.

[111]   H. Liu, A. T. Neal, Y. Du, and P. D. Ye, "Fundamentals in MoS_2 Transistors: Dielectric, Scaling and Metal Contacts," *ECS Transactions*, vol. 58, no. 7, pp. 203–208, Oct. 2013.

[112]   A. Tynkova, S. Sidorenko, S. Voloshko, A. R. Rennie, and M. A. Vasylyev, "Interdiffusion in Au(120nm)/Ni(70nm) thin films at the low-temperature annealing in the different atmospheres," *Vaccum*, vol. 87, no. C, pp. 69–74, Jan. 2013.

[113]   L. F. Voss, L. Stafford, J. S. Wright, S. J. Pearton, F. Ren, and I. I. Kravchenko, "W_2B and CrB_2 diffusion barriers for Ni/Au contacts to p-GaN," *Appl. Phys. Lett.*, vol. 91, no. 4, pp. 042105–4, Jul. 2007.

[114]   D. Jena and A. Konar, "Enhancement of Carrier Mobility in Semiconductor Nanostructures by Dielectric Engineering," *Phys. Rev. Lett.*, vol. 98, no. 13, pp. 658–4, Mar. 2007.

[115]   M. Mongillo, D. Chiappe, G. Arutchelvan, I. Asselberghs, M. Perucchini, M. Manfrini, D. Lin, C. Huyghebaert, and I. Radu, "Transport properties of chemically synthesized MoS_2 – Dielectric effects and defects scattering," *Appl. Phys. Lett.*, vol. 109, no. 23, pp. 233102–5, Dec. 2016.

[116]   D. S. Fox, Y. Zhou, P. Maguire, A. O'Neill, C. Ó'Coileáin, R. Gatensby, A. M. Glushenkov, T. Tao, G. S. Duesberg, I. V. Shvets, M. Abid, M. Abid, H.-C. Wu, Y. Chen, J. N. Coleman, J. F. Donegan, and H. Zhang, "Nanopatterning and Electrical Tuning of MoS_2 Layers with a Subnanometer Helium Ion Beam," *Nano Lett.*, vol. 15, no. 8, pp. 5307–5313, Aug. 2015.

[117]   Y. J. Zhang, J. T. Ye, Y. Yomogida, T. Takenobu, and Y. Iwasa, "Formation of a Stable p–n Junction in a Liquid-Gated MoS_2 Ambipolar Transistor," *Nano Lett.*, vol. 13, no. 7, pp. 3023–3028, Jul. 2013.

[118]   Y. Zhang, J. Ye, Y. Matsuhashi, and Y. Iwasa, "Ambipolar MoS_2 Thin Flake Transistors," *Nano Lett.*, vol. 12, no. 3, pp. 1136–1140, Mar. 2012.

[119]   S. A. Svatek, E. Antolin, D.-Y. Lin, R. Frisenda, C. Reuter, A. J. Molina-Mendoza, M. Munoz, N. Agrait, T.-S. Ko, D. P. de Lara, and A. Castellanos-Gomez, "Gate tunable photovoltaic effect in MoS_2 vertical p-n homostructures," *Journal of Materials Chemistry C: Materials for optical and electronic devices*, vol. 5, pp. 854–861, Jan. 2017.

[120]   A. Ray, R. Nori, P. Bhatt, S. Lodha, R. Pinto, V. R. Rao, F. Jomard, and M. Neumann-Spallart, "Optimization of a plasma immersion ion implantation process for shallow junctions in silicon," *Journal of Vacuum Science & Technology A: Vacuum, Surfaces, and Films*, vol. 32, no. 6, pp. 061302–10, Nov. 2014.

[121]   M. Chen, H. Nam, S. Wi, L. Ji, X. Ren, L. Bian, S. Lu, and X. Liang, "Stable few-layer MoS_2 rectifying diodes formed by plasma-assisted doping," *Appl. Phys. Lett.*, vol. 103, no. 14, pp. 142110–5, Sep. 2013.

[122]   S. Wi, H. Kim, M. Chen, H. Nam, L. J. Guo, E. Meyhofer, and X. Liang, "Enhancement of Photovoltaic Response in Multilayer MoS_2 Induced by Plasma Doping," *ACS Nano*, vol. 8, no. 5, pp. 5270–5281, May 2014.

[123]   R. Murray, K. Haynes, X. Zhao, S. Perry, C. Hatem, and K. Jones, "The Effect of Low Energy Ion Implantation on MoS_2," *ECS J. Solid State Sci. Technol.*, vol. 5, no. 11, pp. Q3050–Q3053, Aug. 2016.

[124]   K. Dolui, I. Rungger, C. Das Pemmaraju, and S. Sanvito, "Possible doping strategies for MoS_2 monolayers: An ab initiostudy," *Phys. Rev. B*, vol. 88, no. 7, pp. 075420–9, Aug. 2013.

[125]   J. Bai, X. Li, A. Wang, R. Prins, and Y. Wang, "Hydrodesulfurization of dibenzothiophene and its hydrogenated intermediates over bulk MoP," *Journal of Catalysis*, vol. 287, no. C, pp. 161–169, Mar. 2012.

[126]   P. Xiao, M. A. Sk, L. Thia, X. Ge, R. J. Lim, J.-Y. Wang, K. H. Lim, and X. Wang, "Molybdenum phosphide as an efficient electrocatalyst for the hydrogen evolution reaction," *Energy Environ. Sci.*, vol. 7, no. 8, pp. 2624–2629, May 2014.

[127]   M. Donarelli, F. Bisti, F. Perrozzi, and L. Ottaviano, "Tunable sulfur desorption in exfoliated MoS_2 by means of thermal annealing in ultra-high vacuum," *Chemical Physics Letters*, vol. 588, no. C, pp. 198–202, Nov. 2013.

[128]   S. Mathew, K. Gopinadhan, T. K. Chan, X. J. Yu, D. Zhan, L. Cao, A. Rusydi, M. B. H. Breese, S. Dhar, Z. X. Shen, T. Venkatesan, and J. T. L. Thong, "Magnetism in MoS_2 induced by proton irradiation," *Appl. Phys. Lett.*, vol. 101, no. 10, pp. 102103–5, Sep. 2012.

[129]   H.-P. Komsa, J. Kotakoski, S. Kurasch, O. Lehtinen, U. Kaiser, and A. V. Krasheninnikov, "Two-Dimensional Transition Metal Dichalcogenides under Electron Irradiation: Defect Production and Doping," *Phys. Rev. Lett.*, vol. 109, no. 3, pp. 035503–5, Jul. 2012.

[130]   G. H. Ryu, J. Lee, N. Y. Kim, Y. Lee, Y. Kim, M. J. Kim, C. Lee, and Z. Lee, "Line-defect mediated formation of hole and Mo clusters in monolayer molybdenum disulfide," *2D Materials*, vol. 3, no. 1, pp. 014002–8, Mar. 2016.

[131]   Z. G. Yu, Y.-W. Zhang, and B. I. Yakobson, "An Anomalous Formation Pathway for Dislocation-Sulfur Vacancy Complexes in Polycrystalline Monolayer MoS_2," *Nano Lett.*, vol. 15, no. 10, pp. 6855–6861, Oct. 2015.

[132]   R. Addou, L. Colombo, and R. M. Wallace, "Surface Defects on Natural MoS_2," *ACS Appl. Mater. Interfaces*, vol. 7, no. 22, pp. 11921–11929, Jun. 2015.

[133]   M. Ghorbani-Asl, S. Kretschmer, D. E. Spearot, and A. V. Krasheninnikov, "Two-dimensional MoS_2 under ion irradiation: from controlled defect production to electronic structure engineering," *2D Materials*, pp. 1–9, Jul. 2017.

[134]   S. McDonnell, R. Addou, C. Buie, R. M. Wallace, and C. L. Hinkle, "Defect-Dominated Doping and Contact Resistance in MoS_2," *ACS Nano*, vol. 8, no. 3, pp. 2880–2888, Mar. 2014.

[135]   H.-P. Komsa, S. Kurasch, O. Lehtinen, U. Kaiser, and A. V. Krasheninnikov, "From point to extended defects in two-dimensional MoS_2: Evolution of atomic structure under electron irradiation," *Phys. Rev. B*, vol. 88, no. 3, pp. 035301–8, Jul. 2013.

[136]   W. Zhou, X. Zou, S. Najmaei, Z. Liu, Y. Shi, J. Kong, J. Lou, P. M. Ajayan, B. I. Yakobson, and J.-C. Idrobo, "Intrinsic Structural Defects in Monolayer Molybdenum Disulfide," *Nano Lett.*, vol. 13, no. 6, pp. 2615–2622, Jun. 2013.

[137]   N. Sengoku and K. Ogawa, "Investigations of Electronic Structures of Defects Introduced by Ar Ion Bombardments on MoS_2 by Scanning Tunneling Microscopy," *Jpn. J. Appl. Phys.*, 1995.

[138]   J.-Y. Noh, H. Kim, and Y.-S. Kim, "Stability and electronic structures of native defects in single-layer MoS_2," *Phys. Rev. B*, vol. 89, no. 20, pp. 205417–12, May 2014.

BIOGRAPHICAL SKETCH

Ryan Murray was raised by a loving family in South Florida. He grew up ever curious and fascinated at the world around him, and was always encouraged by his parents to play with that world. At the age of 11 he began his life-long love of playing guitar. He was the captain of his High School wrestling team, two-time State Tournament Qualifier, and an Assistant Coach for the Olympic Heights Lions. He was in a band or two. He is a children's book writer, short story author, and hopeful novelist. He enjoys the feeling of flying from riding a bike, and enjoys the feeling of being grounded while doing yoga. In 2007 he graduated from the University of Florida with a Bachelor of Science in electrical and computer engineering. Following his undergraduate degree, Ryan taught music at a non-profit music school and worked as a Quality Engineer. He received a Master of Engineering in nanotechnology from the University of Pennsylvania in 2013. In August of 2017, he received his Doctor of Philosophy in materials science and engineering from the University of Florida.